

u^b

b
UNIVERSITÄT
BERN

PAUL SCHERRER INSTITUT
PSI

ACHIP at SwissFEL - Electron Beam Shaping with Dielectric Micro Structures

Inaugural Dissertation
of the Faculty of Science,
University of Bern

presented by

Benedikt Hermann
from Starnberg, Germany

Date of Defence: July 8, 2021

This work is licensed under a Creative Commons License:
Attribution 4.0 International.
This does not apply to quoted content from other authors.
To view a copy of this license visit
<http://creativecommons.org/licenses/by/4.0/>

Supervisors

Dr. Rasmus Ischebeck

Paul Scherrer Institut, 5232 Villigen PSI, Switzerland

Prof. Dr. Thomas Feuerer

Institute of Applied Physics, University of Bern, 3012 Bern, Switzerland

Examinors

Prof. Dr. Thomas Feuerer

Institute of Applied Physics, University of Bern, 3012 Bern, Switzerland

Prof. Dr. Yves Bellouard

École Polytechnique Fédérale de Lausanne, 1015 Lausanne, Switzerland

Accepted by the Faculty of Science, University of Bern.

The Dean, Prof. Dr. Zoltan Balogh

Bern, July 8, 2021

Declaration of consent

on the basis of Article 18 of the PromR Phil.-nat. 19

Name/First Name: Hermann, Benedikt

Registration Number: 12-937-009

Study program: Physics

Bachelor Master Dissertation

Title of the thesis: ACHIP at SwissFEL - Electron Beam Shaping with Dielectric Micro Structures

Supervisor: Prof. Dr. Thomas Feurer
Dr. Rasmus Ischebeck (PSI)

I declare herewith that this thesis is my own work and that I have not used any sources other than those stated. I have indicated the adoption of quotations as well as thoughts taken from other authors as such in the thesis. I am aware that the Senate pursuant to Article 36 paragraph 1 litera r of the University Act of September 5th, 1996 and Article 69 of the University Statute of June 7th, 2011 is authorized to revoke the doctoral degree awarded on the basis of this thesis.

For the purposes of evaluation and verification of compliance with the declaration of originality and the regulations governing plagiarism, I hereby grant the University of Bern the right to process my personal data and to perform the acts of use this requires, in particular, to reproduce the written thesis and to store it permanently in a database, and to use said database, or to make said database available, to enable comparison with theses submitted by others.

Zürich, June 7, 2021

Place/Date



Signature

Abstract

Particle accelerators are the workhorse not only for modern particle physics but also for many other scientific and medical applications. For example, at CERN, the success in exploring matter on the smallest scale is based on the large hadron collider, a 27-kilometer long circular accelerator. Impactful research in biochemistry and material science has been enabled by bright X-ray light sources such as free-electron lasers. They require accelerators on the kilometer-scale which are only available at national research facilities. Regarding medical applications, proton therapy is a successful method to fight tumors in the human body. However, the access to such complex and costly machines is limited to a fraction of humanity.

The size of the accelerator facilities in operation today is dominated by the achievable electric field gradients. During the recent century, the standard technology using metallic cavities driven by microwaves has been heavily optimized but is approaching a fundamental limit: The gradients cannot be increased beyond the vacuum breakdown limit. Plasma and dielectric accelerators are novel techniques that promise more compact and cost-efficient devices with extremely high field gradients.

This thesis focuses on diagnostics, technology and applications for dielectric electron accelerators. A new diagnostic for strongly focused electron beams has been developed: Nano-fabricated metallic wires were successfully used for phase space tomography with sub-micrometer resolution. This tool could be applied at other advanced accelerator research facilities operating with micrometer-scale beams. Furthermore, the applicability of dielectric accelerators for beam shaping at existing free-electron laser facilities has been investigated. A tunable dielectric wakefield structure has been designed and tested for passive beam shaping. This device could serve to prepare a desired longitudinal phase space for a specific free-electron laser mode. A theoretical study explores the use of a dielectric laser accelerator for pulse train generation at free-electron lasers.

Acknowledgments

This work was funded by the Gordon and Betty Moore Foundation as part of the ACHIP collaboration (Grant GBMF4744).

Throughout my PhD I have received a great deal of support, guidance and assistance from numerous individuals.

I would first like to thank my supervisors, Rasmus Ischebeck and Thomas Feurer, for their insightful feedback and guidance, which sharpened my thinking and brought my work to a higher level. During the shifts at SwissFEL, sometimes on weekends or during the night, I could always count on the support of Rasmus. Many thanks for your efforts!

I am grateful for discussions with members of the ACHIP collaboration during our wonderful collaboration meetings we had around the world. Especially, I am indebted to Thilo Egenolf and Uwe Niedermayer for their work on the wake field simulations. Thank you!

I would like to acknowledge Vitaliy Guzenko from the Laboratory for Micro and Nanotechnology at PSI for fabricating the spider-web shaped wire scanner.

I am indebted to Adrian Kirchner for his work on beam tomography and setup of the Michelson interferometer.

Many thanks to the SwissFEL Beam Dynamics group for supporting and discussing simulations and experiments throughout the different projects.

I am grateful for the assembly and calibration of the focusing quadrupoles by the magnet group at PSI.

I would like to thank the SwissFEL Operations group for help with machine related questions.

Many thanks also to the PSI vacuum group for venting the ACHIP chamber every time I wanted to install something new and for making sure the vacuum chamber stays tight and clean.

I would like to express my gratitude towards my family for supporting and encouraging me throughout my entire studies. Finally, I would like to thank my friends who helped to distract and rest my mind outside of my research.

Contents

Abstract	v
Acknowledgments	vii
Contents	ix
1 Introduction	1
1.1 Particle Accelerators	1
1.2 The Accelerator on a Chip International Program (ACHIP)	2
1.3 The ACHIP Chamber at SwissFEL	3
1.4 Beam shaping applications for FELs	4
2 Components at the ACHIP Chamber in SwissFEL	7
2.1 In-Vacuum Permanent Magnet Quadrupoles	8
2.2 Sample Positioning System	10
2.3 Electron Beam Diagnostics	10
2.3.1 Scintillating Screens	10
2.3.2 Nanofabricated Wire Scanners	12
2.4 Michelson Interferometer for THz Radiation	12
3 Transverse Beam Tomography with Wire Scanners	15
3.1 Introduction	16
3.2 Experimental Setup	18
3.2.1 Accelerator Setup	18
3.2.2 ACHIP Chamber	19
3.2.3 Nano-Fabricated Wire Scanner	19
3.2.4 Beam Loss Monitor	22
3.3 Transverse Phase Space Reconstruction Algorithm	22
3.3.1 Reconstruction of a Simulated Measurement	25
3.4 Results	25

3.5	Discussion	30
3.5.1	Resolution Limit	31
3.5.2	Comparison to other Profile Monitors	31
3.6	Conclusion	32
3.7	Appendix	33
3.7.1	Error Estimation	33
3.7.2	Termination Criterion for Reconstruction Algorithm	34
3.7.3	Reconstruction of non-Gaussian Beams	34
4	Dielectric Grating Wakefields	37
4.1	Introduction	38
4.2	Experimental Setup	39
4.2.1	Accelerator Setup	39
4.2.2	ACHIP Chamber	40
4.2.3	Wakefield Structure	40
4.3	Experimental Results	41
4.3.1	Effect of Grating Gap	42
4.3.2	Effect of Beam Tilts and Offsets	44
4.4	Simulation of the Experiment	46
4.4.1	Longitudinal Phase Space Reconstruction	46
4.4.2	CST Wakefield Simulations	49
4.5	Summary and Discussion	56
5	Optical Bunching in FELs Using Dielectric Laser Modulation	59
5.1	Introduction	60
5.1.1	Modulation of Electron Beams in a Laser-Driven Dielectric Double Grating	61
5.2	Simulation Results	63
5.2.1	Modulation and Compression	63
5.2.2	Comparison with Undulator Modulation	64
5.3	Discussion	69
5.4	Methods	71
5.4.1	Emittance Optimization for SwissFEL	71
5.4.2	Electron Optics for High Current Beams	71
5.4.3	Structure Optimization and Transverse Effects	72
5.4.4	Jitter and Stability Considerations	73

6	Optical Bunching Diagnostics	77
6.1	Introduction	79
6.2	Modulation and Bunching Diagnostics	80
6.3	Energy Spectrometer	80
6.4	Coherent Diffraction Radiation	81
6.5	Transverse Deflecting Cavity	83
6.6	Conclusion	86
7	Conclusions & Outlook	87
	Bibliography	89
	List of Publications	101

1.1 Particle Accelerators

Particle accelerators are driving a plethora of applications in many disciplines. The Large Hadron Collider at CERN is used to probe the smallest structures of matter with protons at energy levels of several TeV. Electron synchrotrons and free-electron lasers (FELs) around the world are using electrons at the GeV-level to generate bright photons ranging from the UV to the hard X-ray regime to explore the structure of proteins and crystals. Electron microscopes operating at energies from several keV to few MeV are widely used by biologists for inspection of cells and proteins. Medical applications include X-ray imaging techniques and tumor irradiation with protons. Most of the accelerators in operation today are based on the conventional technique using metallic cavities driven by microwaves. This technology was mainly developed during the World War II for the generation of high-power electromagnetic waves in the range above 1 GHz and improved for the development of high-energy accelerators, such as the two-mile electron linac at Stanford [RO94]. The maximum achievable field strengths with this technology are limited by vacuum breakdown inside the cavities at fields around 300 MV/m [Bra+03].

Novel particle acceleration techniques achieving gradients orders of magnitude larger than conventional microwave accelerators would make future accelerators more compact, more economic, and ultimately allow us to reach higher energies. Plasma-based accelerators are a promising candidate with demonstrated gradients exceeding 100 GV/m [Mod+95].

High frequency accelerators using THz or laser radiation to power a metallic or dielectric accelerating structure provide methods to accelerate and manipulate electron beams on timescales reaching down to the atto-second level [Bla+19; Sch+19], which would advance capabilities to explore ultra-fast processes, such as electronic motion in condensed matter.

1.2 The Accelerator on a Chip International Program (ACHIP)

The Accelerator on a Chip International Program (ACHIP) is funded by the Gordon and Betty Moore Foundation since 2015. It is an international research collaboration towards the implementation of a dielectric laser accelerator (DLA). A DLA is a compact accelerator that is powered by infrared lasers. A nano-fabricated photonic structure is used to transfer energy from the laser to charged particles travelling in a vacuum channel. Due to the high laser damage threshold of dielectrics, e.g., fused silica, DLAs open a path to particle acceleration with potential fields exceeding 1 GV/m outperforming conventional microwave accelerators by at least one order of magnitude. This new approach may lead to a down-scaling of accelerators for applications in science, biology and medicine. Furthermore, the inherently short (sub-fs) bunches of an optical accelerator could be used as probes in ultra-fast science experiments. The ACHIP collaboration is aiming to demonstrate the fundamental physics concepts required for an integrated accelerator-on-a-chip for real world applications. The two major goals of the proposed research program are:

1. Demonstrate acceleration with an integrated multi-stage DLA with GV/m peak gradients and energy gain ≥ 1 MeV for sub-relativistic and relativistic electrons.
2. Exploration of capabilities enabled by the transverse fields in DLA structures, including X-Ray and EUV production, focusing, and sub-fs-level diagnostics.

Progress towards a DLA injector for sub-relativistic electrons has been made at labs in Stanford and at Friedrich-Alexander-Universität Erlangen-Nürnberg using photonic structures made of silicon. Acceleration of 28 keV-electrons with a gradient of 133 MV/m using a double pillar structure and a distributed Bragg reflector has been demonstrated by colleagues at Erlangen [You+19]. At Stanford, a dual-pillar structure with two-sided laser illumination was used to successfully accelerate 99 keV-electrons with gradients up to 200 MV/m [Lee+18]. In both experiments the total energy gain was limited to a few keV by the length of the accelerating structure.

An accelerator structure designed from an inverse design approach including on-chip laser coupling was successfully tested with sub-relativistic electrons [Sap+20]. This demonstration of a waveguide-integrated DLA presents an key step for the scalability of this technology.

At UCLA, relativistic 8 MeV-electrons were accelerated in a fused silica double grating illuminated by a laser with a wavelength of 800 nm [Ces+18a; Per+13]. The highest

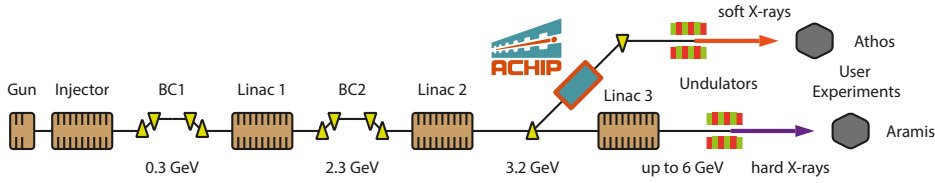


Figure 1.1: Schematic of the free-electron laser SwissFEL at PSI. The ACHIP chamber is located in the switch-yard to the Athos beamline at a beam energy of 3.2 GeV.

measured average accelerating gradient was around 850 MeV/m and was limited by the non-linear Kerr effect. The non-linear response of the dielectric at laser intensities approaching the damage threshold results in a phase velocity mismatch of the accelerating mode and the electrons, which reduces the effective accelerating gradient. This effect could be precompensated by adequately shaping the phase profile of the driving laser [Ces+18a].

1.3 The ACHIP Chamber at SwissFEL

SwissFEL, the free-electron laser (FEL) facility at the Paul Scherrer Institut started construction in 2013 with first user experiments performed in 2018 [Mil+17]. A low-emittance electron beam is generated with a photo-cathode, which is injected into a few hundred meter long linear accelerator based on normal conducting microwave cavities. A maximum charge of 200 pC per bunch can be accelerated up to 6 GeV at a rate of 100 Hz. Two undulator sections (Aramis and Athos) generate hard and soft X-ray pulses for a series of experimental end-stations.

Through the support of the ACHIP collaboration a two-meter long experimental vacuum chamber for DLA research was financed, designed, built, installed and commissioned at SwissFEL [Fer+18; Isc+20; Pra+17]. A schematic drawing, Figure 1.1, shows the layout of SwissFEL and the location of the ACHIP chamber.

The ACHIP chamber is situated in the switch-yard to the Athos beamline, 320 m downstream of the photo-cathode. An adjacent laser room and transfer line provide the infrastructure for potential laser-driven acceleration experiments in the future. The ACHIP chamber contains two permanent magnet triplets to focus and re-match the electron beam which has an energy of 3.2 GeV at this location. At the center of the chamber a six-dimensional positioning system (Smaract hexapod) with nanometer

precision is installed. The hexapod system is used to exchange up to five different samples, align or scan samples with respect to the beam. More information about the components installed in the ACHIP chamber is provided in Chapter 2.

One principle aim of the chamber is to investigate wakefields driven by ultra-relativistic, high-brightness electron beams in dielectric micro-structures to explore beam intensity limits for DLAs and the use of these wakefields to shape the electron beam for advanced FEL applications.

Besides that, the chamber is serving as a test bed to advance electron beam diagnostics including scintillating YAG screens, high-resolution wire scanners and optical transition radiation (OTR) monitors. Another topic under study: radiation generation using the coherent Smith-Purcell effect in dielectric structures. In collaboration with colleagues from FAU Erlangen a geometry to extract narrow-band THz radiation from the electron beam was optimized based on inverse design principles.

1.4 Beam shaping applications for FELs

Structuring the electron beam before it enters the undulators of an FEL enables advanced FEL modes. By creating or removing correlations in parts of the longitudinal phase space, ultra-short individual pulses, pulse trains or narrow-band radiation can be created.

The enhanced SASE scheme (eSASE) is a laser-driven modulation of the electron beam in a magnetic undulator followed by a magnetic chicane which converts the energy modulation into a temporal bunching. This scheme has been proposed by Zholents [Zho05] and is being implemented at SLAC [Cof+19]. It is planned to implement a similar modulation technique at SwissFEL within the scope of the Hidden Entangled Resonating Orders project (HERO) [HER21]. The eSASE technique allows very flexible and tunable shaping of the longitudinal phase space, through temporal shaping of the laser pulse and undulator parameters.

Synchronization of the modulating laser to the electron beam being generated hundreds of meters apart remains challenging. The arrival time jitter between the electron bunch and laser is typically on the order of 10 fs. This aspect in combination with a large economic footprint makes the eSASE scheme unsuitable for future compact FELs targeting the sub-fs X-ray regime.

A potential alternative to the conventional eSASE scheme could be provided by a DLA. A dielectric grating structure replaces the magnetic undulator to transfer energy from the laser to the electron beam. This scheme requires tight focusing of the electron beam

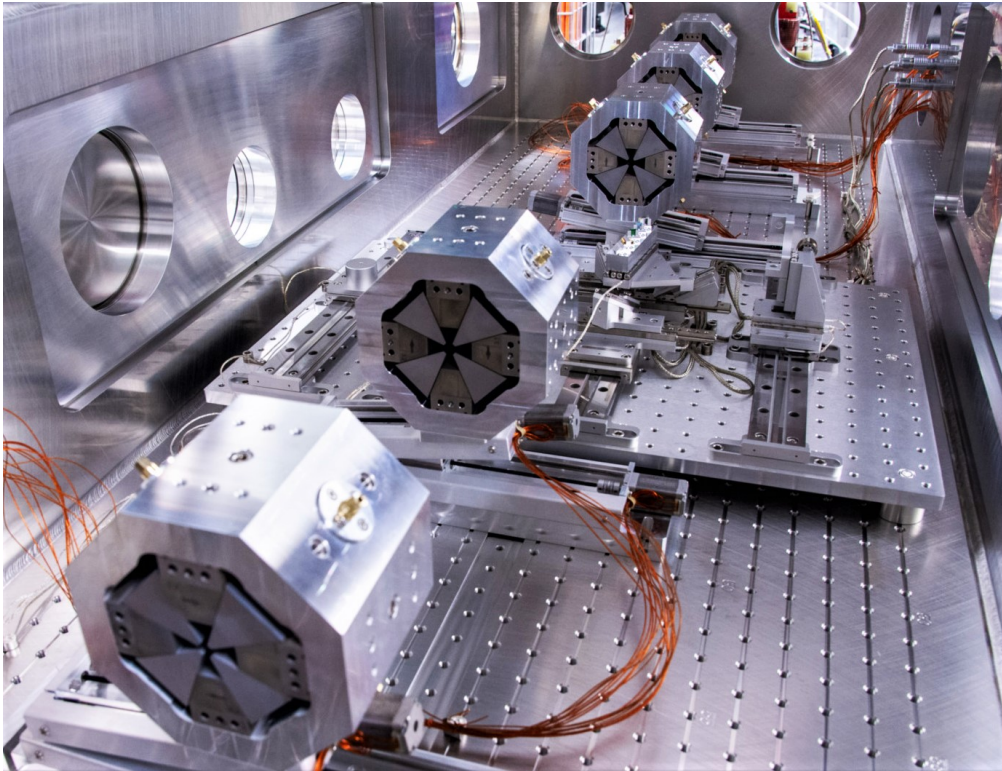


Figure 1.2: Inside view of the ACHIP chamber. The hardware components are described in Chapter 2.

but has an improved laser-to-modulation efficiency and could therefore provide a more economic and compact alternative to the conventional eSASE scheme. A simulation study on the applicability of DLAs for the modulation of electron beams at FELs is given in Chapter 5.

Methods which extract energy of the beam in the form of radiation and use these fields to shape the beam passively overcome temporal synchronization issues and result in a significant cost reduction since no external laser is needed. One of the proposed methods uses radiation emitted by the tail of the beam to modulate the core inside a resonant wiggler magnet [Mac+19]. In Chapter 4 we describe a passive beam shaping approach that uses wakefields excited by the electron beam inside a dielectric micro-structure. The structure under investigation is a double grating with a periodicity of $50\ \mu\text{m}$ fabricated by FEMTOprint [FEM]. The gap of the structure varies along the normally invariant direction from $10\ \mu\text{m}$ to $100\ \mu\text{m}$, enabling continuous tunability, an essential requirement for passive beam shaping techniques.

2

Components at the ACHIP Chamber in SwissFEL

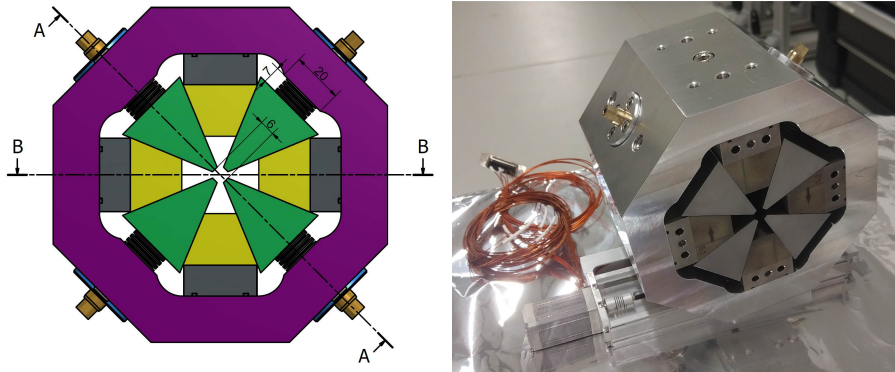


Figure 2.1: CAD drawing and photo of the permanent magnet quadrupole mounted on the positioning stage. Units in mm.

2.1 In-Vacuum Permanent Magnet Quadrupoles

Strong transverse focusing of the 3.2 GeV electron beam is required to achieve loss-less transmission through micrometer-sized apertures. The required transverse forces for ultra-relativistic electrons are created by permanent magnet quadrupoles. Placing the magnets inside the vacuum chamber enables a reduced aperture of 6 mm and therefore larger fields. Net focusing in both planes is achieved by a quadrupole triplet consisting of two weaker and one stronger quadrupole with altered polarity. To ensure a controlled transport in the down-stream beamline, a second, identical quadrupole triplet after the interaction point is used to rematch the beam. All quadrupoles are mounted on two-dimensional mounting systems that allow us to align the quadrupoles transversely and retract them from the beamline for normal SwissFEL operation. The design of the quadrupole focusing system is described in [Fer+18; Pra+17].

The choice of the magnetic material is done following the requirements of the gradients and minimum aperture as well as the radiation hardness. Permanent magnets are prone to demagnetisation, i.e., permanent reduction of their remanence (B_r), when interacting with high energy particles scattered while manipulating the beam. One of the known and main mechanism has a thermodynamic nature: the lost particles interact with the magnetic material and locally increase its temperature. The coercivity force keeps the magnetic domain stable against the external field but with increasing temperature coercivity decreases until it equals the force which finally flips the domain. $\text{Sm}_2\text{Co}_{17}$ is chosen for its relative high remanence ($B_r = 1.1 \text{ T}$) with respect to SmCo_5

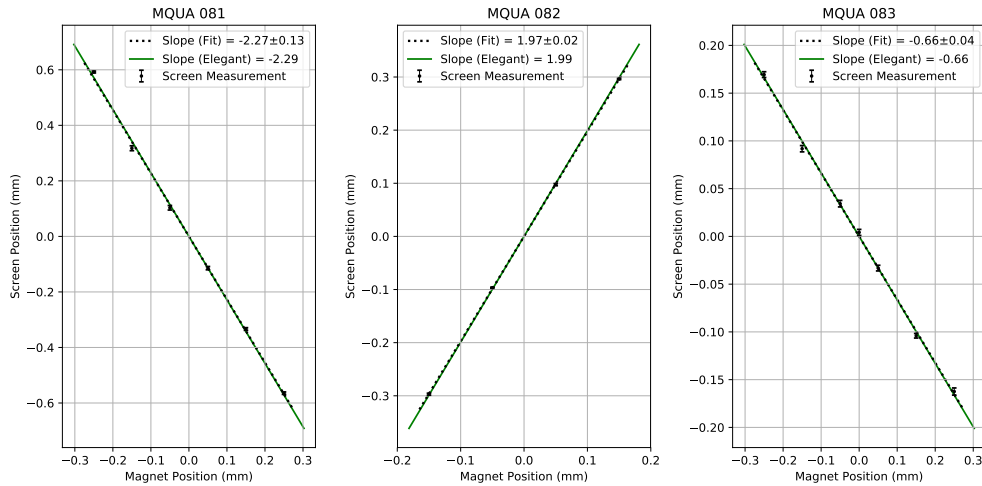


Figure 2.2: Measurement of the strength of three permanent magnet quadrupoles. The transverse kicks generated by transverse position offsets of the magnets match to the design simulation done with the particle tracking code Elegant [Bor00].

($B_r = 0.95$ T) and lower temperature dependence of the coercivity forces, about a factor of two lower than the stronger NdFeB ($B_r = 1.25$ T). Experiments have been carried out [Hei+18; Mar+06] which corroborate this choice. To enhance the field while keeping the magnets far from the beam, a hybrid structure is designed which modifies the Hallbach configuration [Hal80] substituting ferromagnetic poles in place of the radially magnetised blocks. To optimise the cost of their production, the low-gradient quadrupoles are equipped with simple Fe poles, while the high-gradient quadrupoles are equipped with the more performing and expensive CoFe poles.

The design value for the integrated gradient of the magnetic field along the beam axis is 38.76 T for the stronger quadrupoles and -25.9 T for the weaker quadrupoles. The strengths of the quadrupoles can be modified by tuning the gap with adjustment screws. The pre-beam calibration was done by the magnet group at PSI and deviations from the target strength were below 0.1 % for all quadrupoles.

Additionally, we verified the strength of the calibrated quadrupoles using a beam-based measurement. For this purpose, the three magnets upstream of the interaction point are individually moved onto the axis of the electron beam and then displaced by up to few hundred micrometer. The resulting transverse kick is measured with a scintillating

screen (YAG) in the center of the interaction chamber, which is imaged onto a CCD sensor placed outside of the vacuum chamber. We evaluate the beam position with a Gaussian fit to the projected beam profile. The measured quadrupole kicks agree well with beam dynamics simulations using the design values for the quadrupole strengths and lengths (Figure 2.2). The simulations are carried out with the tracking code Elegant [Bor00]. This test confirms that the strengths of the focusing quadrupoles match well to their respective design values within the precision of this measurement (around 1 %).

2.2 Sample Positioning System

A six-dimensional positioning system (hexapod) built by Smaract is used for sample alignment at the interaction point at the center of the ACHIP chamber. The system is based on synchronized piezoelectric translation stages which achieve an absolute precision of below 200 nm. Relative movements can be as small as 1 nm for translational or 1 μ rad for rotational motion. The hexapod carries an additional translation stage, which is used to exchange up to five different samples. The individual samples are attached to the sample stage without screws or glue, just by a kinematic mounting system. Each sample sits on three steel spheres which touch the sample holder on six compatible surfaces. This makes sample exchange extremely fast and repeatable, thus reducing the amount of time the vacuum chamber has to be opened during sample installation, which helps to keep pollution and condensation on the inside surfaces of the chamber low. Figure 2.3 shows a photograph of the kinematic mounting system designed for the ACHIP chamber.

2.3 Electron Beam Diagnostics

2.3.1 Scintillating Screens

Cerium doped YAG screens are a well established scintillating material to measure the transverse distribution of ultra-relativistic, high-brightness electron beams at FELs on a single shot basis [Isc+15]. To image the screen onto a camera, we installed a long-working-distance microscope outside of the chamber with adjustable magnification (up to 7 x). The numerical aperture at the highest magnification is 0.08 (full specifications of the microscope: https://www.global-optosigma.com/en_jp/application/ulwz.html). We mounted two YAG crystals on the hexapod sample stage with thicknesses of

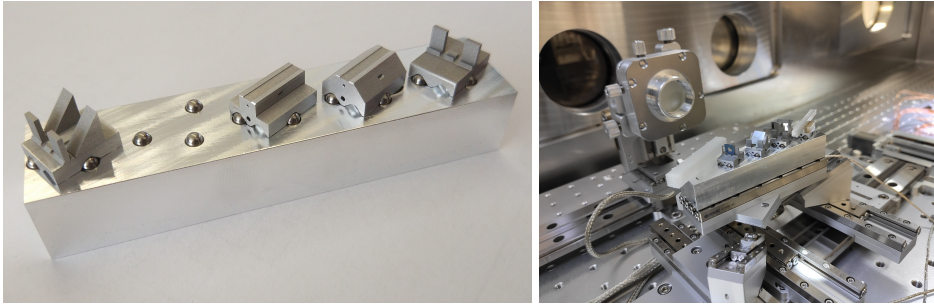


Figure 2.3: Kinematic mounting system designed for the sample stage in the ACHIP vacuum chamber (left) and installed hexapod with five samples (right).

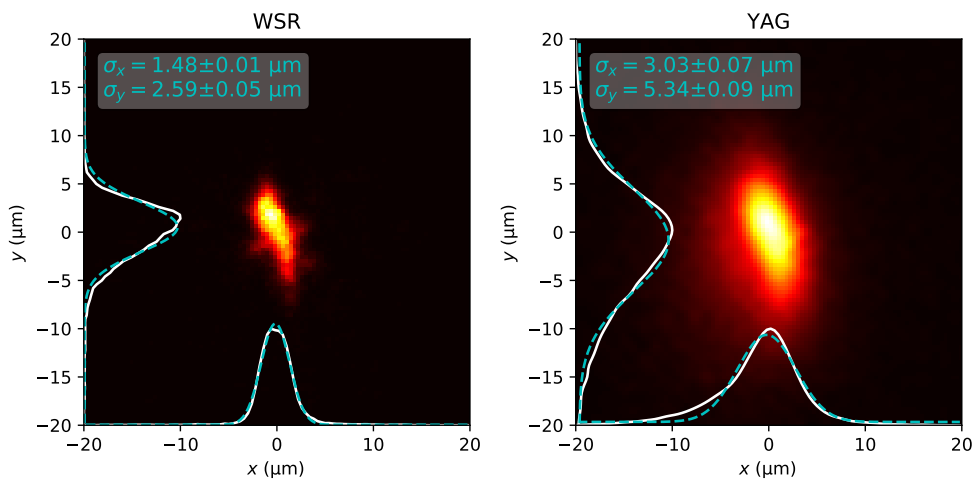


Figure 2.4: Comparison of measured 2D beam profile from multiple wire scans (left) and a scintillating YAG screen (right).

20 μm and 50 μm . We use these screens for initial beam optimization and quadrupole alignment. We did not observe a significant reduction of measured beam sizes, when using the thinner screen. In Figure 2.4, we compare the beam profile measured by the YAG screen and compare it to the profile obtained with a method based on multiple wire scans (for the same electron beam conditions). The smallest beam size (σ of a Gaussian fit) measured with the YAG screen and microscope is around 3 μm , which is at least a factor of three better than the standard SwissFEL screens [Isc+15], but still a factor of two larger than the corresponding measurement with a nano-fabricated wire scanner (see following paragraph). In the future we plan to conduct more studies on screen resolution and saturation effects in scintillating materials beyond Cerium doped YAG.

2.3.2 Nanofabricated Wire Scanners

Sub-micrometer beams have been successfully characterized along on dimension with single nano-fabricated gold wires, which are scanned across the beam [Bor+18; Orl+20]. Based on this technology, we designed and built a single nano-fabricated wire scanner device which consists of nine wires oriented at different angles. Using tomographic reconstruction techniques the 2D beam profile can be assessed with sub-micrometer resolution. The fabrication (electron beam lithography) was done by Vitaliy Guzenko at the Laboratory for Micro and Nanotechnology (LMN) at PSI. Two of the multi-dimensional wire scanner devices were sent to colleagues from the ACHIP collaboration at DESY for beam characterization at the linac of the Accelerator Research Experiment at SINBAD (ARES) [Mar+20], where relativistic DLA experiments are under preparation [May+18]. Detailed information on this high-resolution beam profile diagnostic using nano-fabricated wires can be found in chapter 3.

2.4 Michelson Interferometer for THz Radiation

The small and short electron beam available at the ACHIP chamber is well suited for testing of beam based radiation schemes, e.g., Smith-Purcell radiation from periodic structures [SP53]. Due to the short bunch lengths, down to few fs, and small beam sizes, in the order of 1 μm , coherent generation of radiation at infrared and THz wavelengths is conceivable. To characterize the spectrum of the emitted radiation we have installed a Michelson interferometer on one side of the ACHIP chamber. The movable mirror in one arm of the spectrometer allows us to measure the auto-correlation of the radiation

and to obtain the spectrum via Fourier transformation. The installed beam-splitter is made of high resistivity float zone silicon (HRFZ-Si), which provides a splitting ratio of 60/40 for wavelengths ranging from 50 μm to 1000 μm . The detector is a Schottky diode from ACST [ACS] (Type 3DL 12C LS2500 A2), which is sensitive from 300 μm to 4000 μm . Figure 2.5 shows a photograph of the Michelson interferometer setup for THz radiation. For studies at shorter wavelengths, the beam-splitter and detector have to be replaced.

We successfully used this spectrometer to characterize the radiation of a structure which was inversely designed to extract narrow-band THz radiation from the electron beam. The geometry was optimized in collaboration with Urs Häusler from FAU Erlangen and 3D-printed at PSI. The design together with the experimental characterization of the radiation is planned to be published in a separate manuscript.

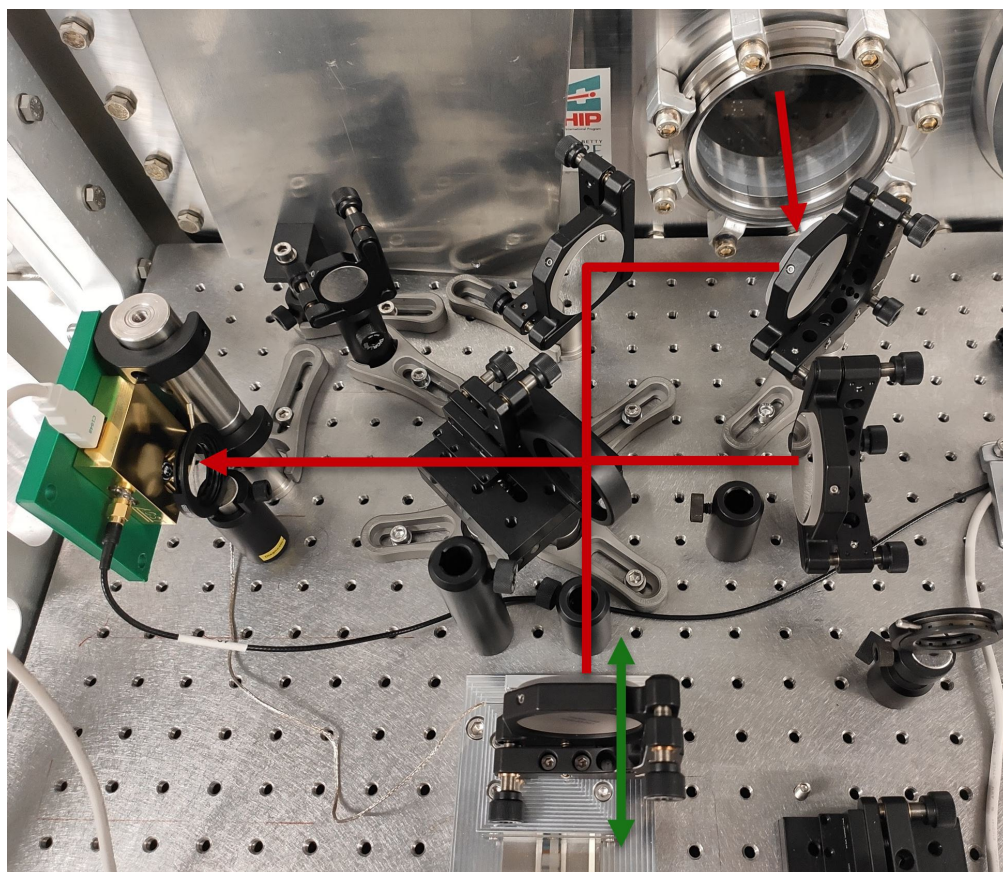


Figure 2.5: Michelson interferometer for THz radiation characterization next to the ACHIP chamber.

3

Transverse Beam Tomography with Wire Scanners

Electron beam transverse phase space tomography using nanofabricated wire scanners with submicrometer resolution

Authors: Benedikt Hermann^{1,3}, Vitaliy A. Guzenko¹, Orell R. Hürzeler¹, Adrian Kirchner², Gian Luca Orlandi¹, Eduard Prat¹ and Rasmus Ischebeck¹

¹Paul Scherrer Institut, 5232 Villigen PSI, Switzerland

²Friedrich-Alexander-Universität Erlangen-Nürnberg, 91054 Erlangen, Germany

³Institute of Applied Physics, University of Bern, 3012 Bern, Switzerland

Published: February 15, 2021. Physical Review Accelerators and Beams, Volume 24, Article number: 022802.

DOI: <https://doi.org/10.1103/PhysRevAccelBeams.24.022802>

Abstract

Characterization and control of the transverse phase space of high-brightness electron beams is required at free-electron lasers or electron diffraction experiments for emittance measurement and beam optimization as well as at advanced acceleration experiments. Dielectric laser accelerators or plasma accelerators with external injection indeed require beam sizes at the micron level and below. We present a method using nano-fabricated metallic wires oriented at different angles to obtain projections of the transverse phase space by scanning the wires through the beam and detecting the amount of scattered particles. Performing this measurement at several locations along the waist allows assessing the transverse distribution at different phase advances. By applying a novel tomographic algorithm the transverse phase space density can be reconstructed. Measurements at the ACHIP chamber at SwissFEL confirm that the transverse phase space of micrometer-sized electron beams can be reliably characterized using this method.

3.1 Introduction

High-gradient advanced accelerator concepts including plasma and dielectric structure based schemes are developed at various laboratories for future compact accelerators. The wavelength of the accelerating field in a plasma accelerator is given by the plasma wavelength which is typically on the order of tens of micrometers [ESL09]. A Dielectric

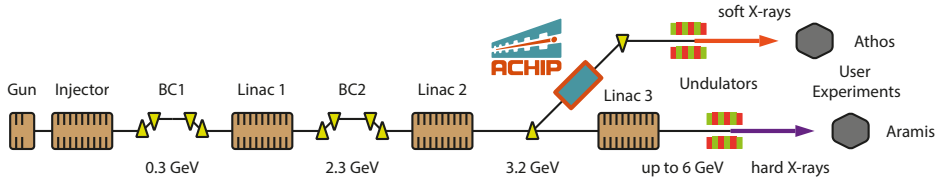


Figure 3.1: Schematic of the free-electron laser SwissFEL at PSI. The ACHIP chamber is located in the switch-yard to the Athos beamline at a beam energy of 3.2 GeV.

laser accelerator (DLA) is operating in the optical to near-infrared spectrum leading to structure apertures on the order of a single micrometer [Eng+14]. Hence, suitable test beams for external injection have to be generated and characterized down to the sub-micrometer level.

Future compact free-electron laser facilities operating at small normalized emittances on the order of 50 nm rad [Ros+20] require profile monitors with micrometer resolution. Electron diffraction requires an even smaller emittance to achieve the required coherence [Ji+19].

Conventional beam profile monitors for ultra-relativistic electron beams are scintillating screens, optical transition radiation (OTR) screens and wire scanners. Screen-based methods provide single-shot two-dimensional information, whereas conventional wire scanners provide multi-shot one-dimensional information.

The thickness of the scintillating screen, the imaging lens and the camera pixel size limit the resolution of this method to around $5\ \mu\text{m}$ to $10\ \mu\text{m}$ [Isc+15; Max+17]. OTR screens with sub-micrometer resolution have been demonstrated, but their application is limited to uncompressed electron bunches [Bol+15]. Typical wire scanners at free-electron laser facilities consist of cylindrical metallic (aluminum or tungsten) wires with diameters down to $5\ \mu\text{m}$ [Orl+16]. Projections of the transverse beam distribution can be measured by moving the stretched wire through the beam and correlating the wire position to the signal of a downstream beam loss monitor, which detects the scattered particle shower. Recent developments at PSI and FERMI led to single (one-dimensional) wire scanners fabricated with electron beam lithography reaching sub-micrometer resolution [Bor+18; Orl+20]. Based on this technology we designed a wire scanner consisting of nine wires arranged radially at different angles, as a tool for precise beam profile tomography at the ACHIP (Accelerator on a Chip International Program) interaction chamber, which is installed in the Athos branch of SwissFEL at PSI (see Fig. 3.1). This chamber is planned to support DLA research and

development [Fer+18; Pra+17]. A possible application of DLA technology for FELs is the generation of a micro-bunched pulse train using laser-based energy modulation followed by magnetic compression [Her+19].

The electrons at the ACHIP interaction point at SwissFEL possess a mean energy of 3.2 GeV and are strongly focused by an in-vacuum permanent magnet triplet [Pra+17]. A six-dimensional positioning system (hexapod) at the center of the chamber is used to exchange, align, and scan samples or a wire scanner for diagnostics.

In this manuscript, we demonstrate that the transverse phase space of a focused electron beam can be precisely characterized with a series of wire scans at different angles and locations along the waist. The transverse phase space ($x - x'$ and $y - y'$) is reconstructed with a novel particle-based tomographic algorithm. This technique goes beyond conventional one-dimensional wire scanners since it allows us to assess the four-dimensional transverse phase space. We apply this algorithm to a set of wire scanner measurements performed with nano-fabricated wires at the ACHIP chamber at SwissFEL and reconstruct the dynamics of the transverse phase space of the focused electron beam along the waist.

3.2 Experimental Setup

3.2.1 Accelerator Setup

The generation and characterization of a micro-meter sized electron beam in the ACHIP chamber at SwissFEL requires a low-emittance electron beam. The beam size along the accelerator is given by:

$$\sigma(z) = \sqrt{\beta(z)\varepsilon_n(z)/\gamma(z)}, \quad (3.1)$$

where β denotes the Twiss (or Courant-Snyder) parameter of the magnetic lattice, γ is the relativistic Lorentz factor of the electrons and ε_n is the normalized emittance of the beam. With an optimized lattice a minimal β -function of around 1 cm in the horizontal and 1.8 cm in the vertical plane is expected from simulations [Fer+18; Pra+17].

In order to reduce chromatic effects of the focusing quadrupoles [Mos+12], we minimize the projected energy spread by accelerating the beam in most parts of the machine close to on-crest acceleration. From simulations, we expect an optimized projected energy spread of 42 keV for a 3 GeV-beam with a charge of 1 pC [Pra+17], which corresponds to a relative energy spread of 1.4×10^{-5} . For this uncompressed and low-energy-spread beam we expect chromatic enlargement of the focused beam size

on the order of 0.1 %.

To lower the emittance of the beam, the bunch charge is reduced to approximately 1 pC from the nominal bunch charge at SwissFEL (10 pC to 200 pC). The laser aperture and pulse energy at the photo-cathode, as well as the current of the gun solenoid, are empirically tuned to minimize the emittance for the reduced charge. The emittance is measured at different locations along the accelerator with a conventional quadrupole scan [Pra14] and a scintillating YAG:Ce screen. After the second bunch compressor, which is the last location for emittance measurements before the ACHIP chamber, the normalized horizontal and vertical emittances are found to be 93 nm rad and 157 nm rad with estimated uncertainties below 10 %. The difference between the horizontal and vertical emittance could be the result of an asymmetric laser spot on the cathode. The electron energy at this emittance measurement location is 2.3 GeV. Subsequently, the beam is accelerated further to 3.2 GeV and directed to the Athos branch by two resonant deflecting magnets (kickers) and a series of dipole magnets [Abe+19]. Finally, the beam is transported to the beam stopper upstream of the Athos undulators.

3.2.2 ACHIP Chamber

The ACHIP chamber at SwissFEL is a multi-purpose test chamber, designed and built for DLA research. It is located in the switch-yard of SwissFEL, where the electron beam has an energy of around 3.2 GeV. The electron beam is focused by an in-vacuum quadrupole triplet and matched back by a second symmetric quadrupole triplet. All six magnets can be remotely retracted from the beam line for standard SwissFEL operation. The positioning system allows the alignment of the quadrupoles with respect to the electron beam. The magnetic center of the quadrupole is found by observing and reducing transverse kicks with a downstream screen or beam position monitor. At the center of the chamber a hexapod allows positioning different samples in the electron beam path. Figure 3.2 shows the interior of the ACHIP chamber including the permanent magnets and the hexapod. Further details about the design of the experimental chamber can be found in [Fer+18; Pra+17] and the first results of the beam characterization can be found in [Isc+20].

3.2.3 Nano-Fabricated Wire Scanner

Nano-fabricated wires are installed on the hexapod for the characterization of the focused beam profile. The wire scan device consists of nine free-standing 1 μm wide metallic (Au) stripes. The nine radial wires are supported by a spiderweb-shaped

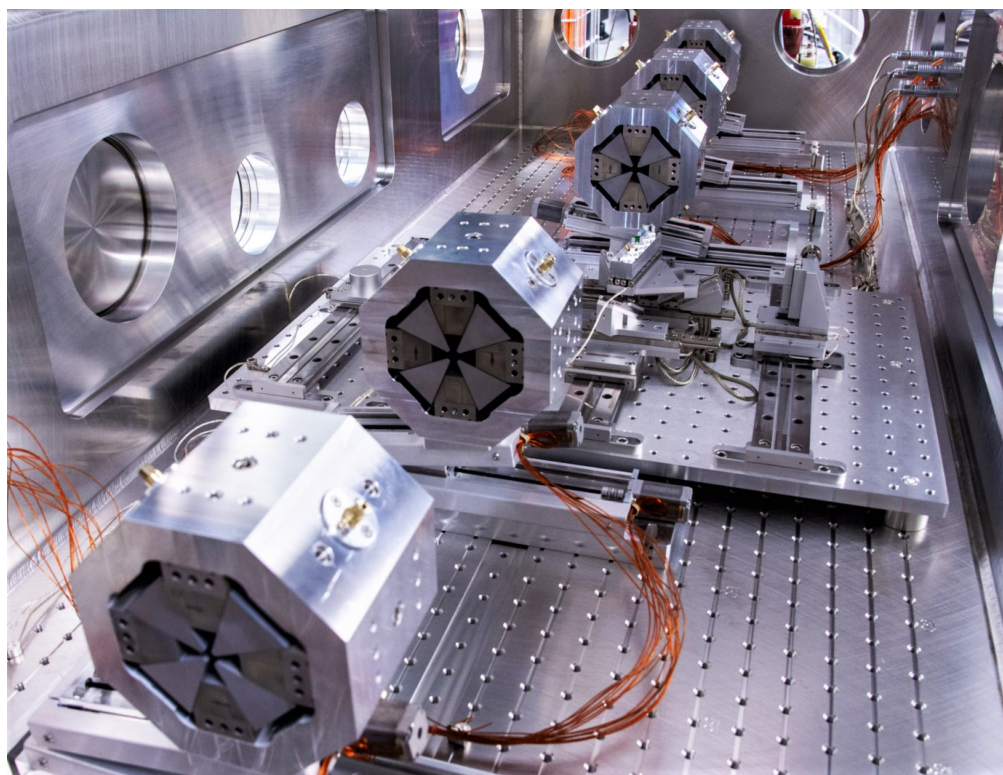


Figure 3.2: Inside view of the ACHIP chamber. Movable quadrupoles for focusing and re-matching are seen in the front and back. The hexapod for sample positioning is located at the center. Image adapted from [Isc+20] under [Creative Commons Attribution 3.0 licence](#).

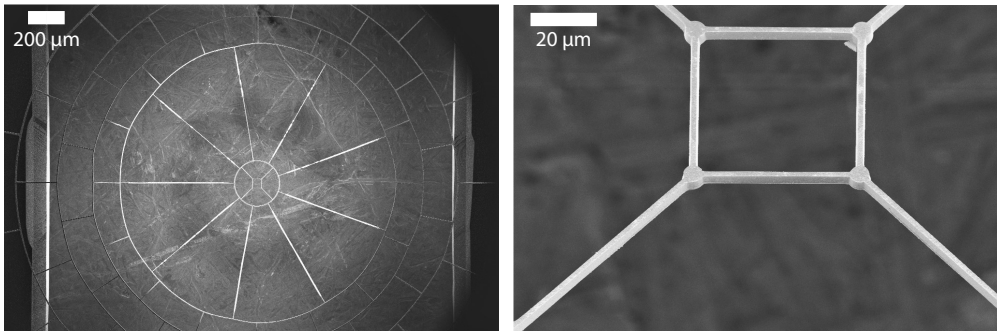


Figure 3.3: Scanning electron microscope images of the free-standing wire scanner device. Nine radial wires which are used for the wire scans are supported by a spiderweb-shaped structure attached to a silicon frame. At the center of the geometry a square simplifies the alignment of the wire scanner with respect to the electron beam. Scanning the square horizontally and vertically across the beam provides 4 distinct peaks (for beam sizes smaller than $50\ \mu\text{m}$). The center of the geometry can be referenced to the hexapod coordinate system from the location of these peaks.

structure attached to a silicon frame. A scanning electron microscope image of the wire scanner sample is shown in Fig. 3.3. We chose nine homogeneously spaced wires for our design, since this configuration allows us to access any wire angle within the tilt limits of the hexapod. The sample was fabricated at the Laboratory for Micro and Nanotechnology at PSI by means of electron beam lithography. The $1\ \mu\text{m}$ wide stripes of gold are electroplated on a $250\ \text{nm}$ thick Si_3N_4 membrane, which is removed afterwards with a KOH bath. The fabrication process and performance for this type of wire scanner are described in detail in [Orl+20]. The hexapod moves the wire scan device on a polygon path to scan each of the nine wires orthogonally through the electron beam. Hereby, projections along different angles (θ) of the transverse electron density can be measured. The two-dimensional transverse beam profile can be obtained using tomographic reconstruction techniques. The hexapod can position the wire scanner within a range of $20\ \text{cm}$ along the beam direction (z). By repeating the wire scan measurement at different locations around the waist, the transverse phase space and emittance of the beam can be inferred.

3.2.4 Beam Loss Monitor

Electrons scatter off the atomic nuclei of the metallic wire and a particle shower containing mainly X-rays, electrons and positrons is generated. The intensity of the secondary particle shower depends on the electron density integrated along the wire and is measured with a downstream beam loss monitor (BLM). The BLM consists of a scintillating fiber wrapped around the beam pipe. The fiber is connected to a photo-multiplier tube (PMT). The signal of the PMT is read-out beam synchronously in a shot-by-shot manner. To avoid saturation of the PMT, the gain voltage needs to be set appropriately. SwissFEL is equipped with a series of BLMs, which are normally used to detect unwanted beam losses and are connected to an interlock system. For the purpose of wire scan measurements, individual BLMs can be excluded from the machine protection system. Details about the BLMs at SwissFEL can be found in [Ozk+20]. For the wire scan measurement reported here, a BLM located 10 m downstream of the interaction with the wire was used.

3.3 Transverse Phase Space Reconstruction Algorithm

Inferring a density distribution from a series of projection measurements is a problem arising in many scientific and medical imaging applications. Standard tomographic reconstruction techniques, e.g., filtered back projection or algebraic reconstruction technique [GBH70] use an intensity on a grid to represent the density to be reconstructed. The complexity of these algorithms scales as $\mathcal{O}(n^d)$, where n is the number of pixels per dimension and d is the number of dimensions of the reconstructed density. Typically, for real space density reconstruction, d is 2 (slice reconstruction) or 3 (volume reconstruction). In the case of transverse phase space tomography d equals 4 (x, x', y, y'), leading to very long reconstruction times.

We developed a reconstruction algorithm based on a macro-particle distribution (instead of the intensity on grid), where each macro-particle, from now on called particle, represents a point in the four-dimensional phase space. The complexity of this algorithm is proportional to n_p (number of particles) and is independent on the dimension of the reconstruction domain. The particle density is then given by applying a Gaussian kernel to each coordinate of the particle ensemble:

$$G_{\kappa} = \frac{1}{\sqrt{2\pi\rho_{\kappa}}} \exp\left(-\frac{\kappa^2}{2\rho_{\kappa}^2}\right), \kappa \in \{x, x', y, y'\} \quad (3.2)$$

where we choose $\rho_{x',y'} = \rho_{x,y}/z_{\max}$, with z_{\max} the range of the measurement along z . Choosing the right kernel size is important for an appropriate reconstruction of the beam. It is dimensioned such that $\rho_{x,x',y,y'}$ represents the length scale below which we expect only random fluctuations in the particle distribution, which are not reproducible from shot to shot. Note that despite the Gaussian kernel, this reconstruction does not assume a Gaussian distribution of the beam, but is able to reconstruct arbitrary distributions that vary on a length scale given by $\rho_{x,x',y,y'}$.

The ensemble of particles is iteratively optimized so that their projections match with the set of measured projections. The algorithm starts from a homogeneous particle distribution. One iteration consists of the following operations.

- Transport $T(z)$
- Rotation $R(\theta)$
- Histogram of the transported and rotated coordinates
- Convolution with wire profile
- Interpolation to measured wire positions
- Comparison of reconstruction and measurement
- Redistribution of particles

In the case of ultra-relativistic electrons transverse space charge effects can be neglected since they scale as $\mathcal{O}(\gamma^{-2})$ and hence $T(z)$ becomes the ballistic transport matrix:

$$T(z) = \begin{pmatrix} 1 & z \\ 0 & 1 \end{pmatrix} \quad (3.3)$$

for (x, x') and (y, y') . The rotation matrix is then applied to (x, y) :

$$R(\theta) = \begin{pmatrix} \cos \theta & \sin \theta \\ -\sin \theta & \cos \theta \end{pmatrix}. \quad (3.4)$$

Afterwards, the histogram of the particles' transported and rotated x coordinates is calculated. Note that the bin width needs to be smaller than the width of the wire, to ensure an accurate convolution with the wire profile. This becomes important when the beam size or beam features are smaller than the wire width. Next, the convolution

of the histogram and the wire profile is interpolated linearly to the measured wire positions ξ . Now, the reconstruction can be directly compared to the measurement:

$$\Delta_{z,\theta}(\xi) = \frac{P_{z,\theta}^m(\xi) - P_{z,\theta}^r(\xi)}{\max_{\xi} P_{z,\theta}^r(\xi)}, \quad (3.5)$$

where $P_{z,\theta}^m$ and $P_{z,\theta}^r$ are the measured and reconstructed projections for the current iteration at position z and angle θ . The difference between both profiles quantifies over- and under-dense regions in the projection. Then, $\Delta_{z,\theta}(\xi)$ is interpolated back to the particle coordinates along the wire scan direction, yielding $\Delta_{z,\theta}^i$ for the i -th particle. Afterwards, we calculate the average over all measured z and θ :

$$\Delta^i = \frac{1}{n_{\theta}n_z} \sum_{\theta,z} \Delta_{z,\theta}^i. \quad (3.6)$$

The sign of Δ^i indicates if a particle is located in an over- or under-dense region represented by the current particle distribution. According to the magnitude of Δ^i the new particle ensemble is generated. A particle is copied or removed from the previous distribution with a probability based on $|\Delta^i|$. This process is implemented by drawing a pseudo-random number $\chi^i \in [0, 1[$ for each particle. In case $\chi^i < |\Delta^i|/s_{\max}$, particle i is copied or removed from the distribution (depending on the sign of Δ^i). Otherwise, the particle remains in the ensemble. Here, s_{\max} is the maximum of all measured BLM signals and is used to normalize Δ^i for the comparison with $\chi^i \in [0, 1[$. This process makes sure that particles in highly under-dense (over-dense) regions are created (removed) with an increased probability.

In the last step of each iteration, a small random value is added to each coordinate according to the Gaussian kernel defined in Eq. 3.2. This smoothens the distribution on the scale of ρ . For the reconstruction of the measurement presented in Sec. 3.4, $\rho_{x,y}$ was set to 80 nm.

The iterative algorithm is terminated by a criterion based on the relative change of the average of the difference $\Delta_{z,\theta}^i$ (further details in Appendix 3.7.2). The measurement range along z ideally covers the waist and the spacing between measurements is reduced close to the waist, since the phase advance is the largest here. Since the algorithm does not assume a specific shape (e.g., Gaussian) of the distribution, asymmetries, double-peaks, or halos of the distribution can be reconstructed (an example is shown in Appendix 3.7.3). Properties of the transverse phase space including, transverse emittance in both planes, astigmatism and Twiss parameters can be calculated from the

reconstructed distribution. To obtain the full 4D emittance, cross-plane information, such as correlations in $x - y'$ or $x' - y$ need to be assessed. For this purpose, the phase advance has to be scanned independently in both planes. This can be achieved with a multiple quadrupole scan as explained for instance in [PA14; Rai+93] but is not achieved by measuring beam projections along a waist, as the phase advance in both planes is correlated.

The presented phase space reconstruction algorithm could also be adapted to use two-dimensional profile measurements from a screen at different phase advances to characterize the four-dimensional transverse phase space.

The python-code related to the described tomographic reconstruction technique is made available on github [Her21].

3.3.1 Reconstruction of a Simulated Measurement

To verify the reconstruction algorithm, we generate a test distribution and calculate a set of wire scan projections (nine projections along different angles at seven locations along the waist). The algorithm then reconstructs the distribution based on these simulated projections. For this test, we choose a Gaussian beam distribution with Twiss parameters $\beta_x^* = 2.0$ cm, $\beta_y^* = 3.0$ cm and a transverse emittance of 200 nm rad in both planes. An astigmatism of -1 cm (longitudinal displacement of the horizontal waist) is artificially introduced. Moreover, noise is added to the simulated wire scan profiles to obtain a signal-to-noise ratio similar to the experimental data show in Sec. 3.4. The Gaussian kernel size for the reconstruction $\rho_{x,y}$ (see Eq. 3.2) is 80 nm, which is around one order of magnitude smaller than the beam size in this test. Figure 3.4 compares the original and reconstructed transverse phase space at $z = 0$ cm. Good agreement ($< 10\%$ error) is achieved for the emittances and astigmatism, which is manifested as a tilt in the $x - x'$ plane. For this numerical experiment, the algorithm terminates according to the criterion described in Appendix 3.7.2 after around 100 iterations. The run-time on a single-core of a standard personal computer is around two minutes. Parallelising the computation on several cores would reduce the computation time by few orders of magnitude.

3.4 Results

We have measured projections of the transverse electron beam profile at the ACHIP chamber at SwissFEL with the accelerator setup, wire scanner and BLM detector

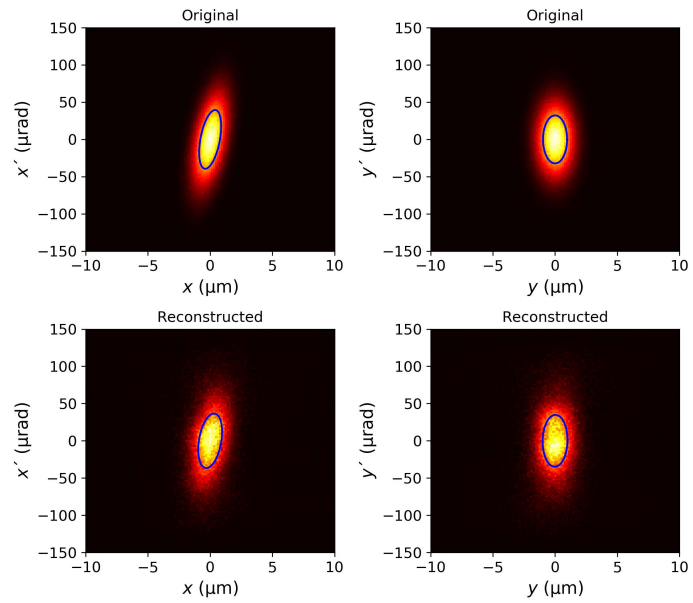


Figure 3.4: Reconstruction from simulated measurement. The original distribution in the transverse phase space is shown in the upper row. An astigmatism of -1 cm is added to the horizontal plane (tilt in $x - x'$). The algorithm reconstructs the transverse phase space based on a set of simulated wire scan projections. The result of the reconstruction is shown in the lower row. The 1σ -ellipse of a 2D Gaussian fit is drawn in blue for each histogram.

	ε_n (nm rad)	β^* (cm)	σ^* (μm)
x	186(15)	3.7(2)	1.04(6)
y	278(18)	3.7(2)	1.26(5)

Table 3.1: Normalized emittance ε_n , Twiss β -function at the waist β^* , and corresponding beam size σ^* of the reconstructed transverse phase space distribution.

described in Sec. 3.2. All nine wire orientations are used at six different locations along the waist of the electron beam. This results in a total of 54 projections of the electron beam's transverse phase space. Lowering the number of projections limits the possibility to observe inhomogeneities of the charge distribution. The distance between measurement locations is increased along z , since the expected waist location was around $z = 0$ cm. All 54 individual profiles are shown in Fig. 3.5. In each sub-plot, the orange dashed curve represents the projection of the reconstructed phase space for the respective angle θ and longitudinal position z . The reconstruction represents the average distribution over many shots and agrees with most of the measured data points. Discrepancies arise due to shot-to-shot position jitter, charge fluctuations, or density variations of the electron beam. The effect of these error sources is discussed further in Appendix 3.7.1. The evolution of the reconstructed transverse phase space along the waist is depicted in Fig. 3.6. The expected rotation of the transverse phase space around the waist is clearly observed. The position of the waist is found to be at around $z = 6.2$ cm downstream of the center of the chamber. Figure 3.7 shows the beam size evolution around the waist. We quantify the normalized emittance and β -function of the distribution by fitting a 2D Gauss function to the distribution in the (x, x') and (y, y') phase space. The $1\text{-}\sigma$ ellipse of the fit is drawn in blue in all sub-plots of Fig. 3.6. We use the following definition for the normalized emittance:

$$\varepsilon_n = \gamma A_{1\sigma} / \pi, \quad (3.7)$$

where $A_{1\sigma}$ is the area of the $1\text{-}\sigma$ ellipse in transverse phase space. The values for the reconstructed emittance, minimal β -function (β^*) and beam size at the waist are summarized in Table 3.1. The measurement range (8 cm) along the waist with $\beta^* = 3.7$ cm covers a phase advance of around 90° .

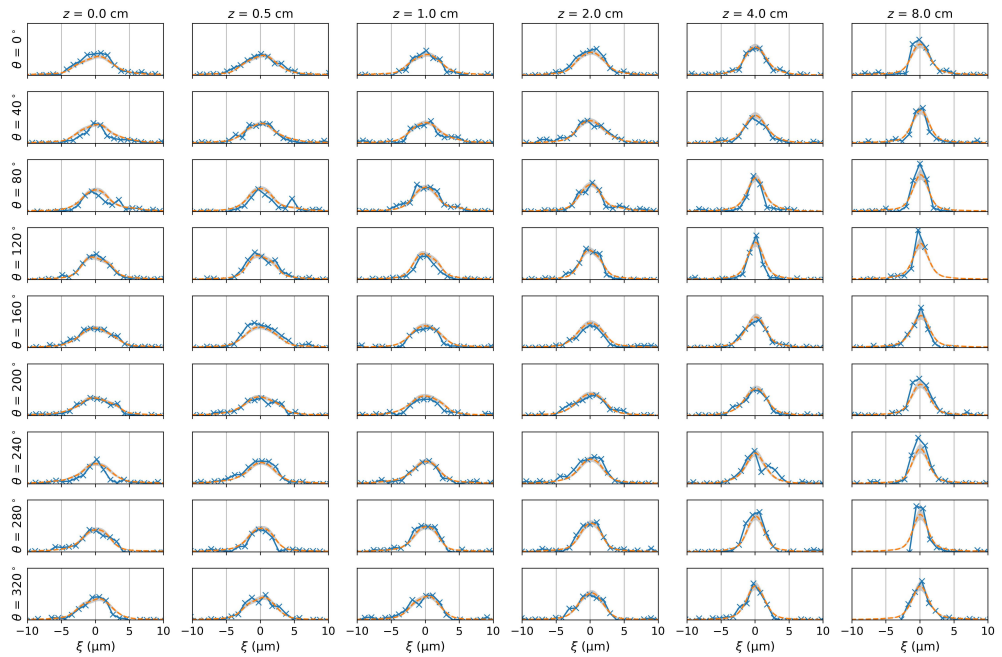


Figure 3.5: Measured (blue crosses) and reconstructed (orange dashed) profiles of the electron beam distribution. The vertical axes are identical for all sub-plots and show the BLM signal or reconstruction in arbitrary units. Sub-plots in the same column correspond to the same z location of the wire scanner and sub-plots in the same row correspond to the same projection angle θ . The grey area depicts the uncertainty of the reconstruction. For the last column ($z = 8$ cm) the scan range did not cover the entire beam profile for all scans due to a misalignment of the electron propagation direction and the z -axis of the hexapod, which results in a transverse offset of the wire scanner device with respect to the electron beam. This effect is the largest for the last scan ($z = 8$ cm) since the wire scanner was aligned to the beam axis at $z = 0$ cm.

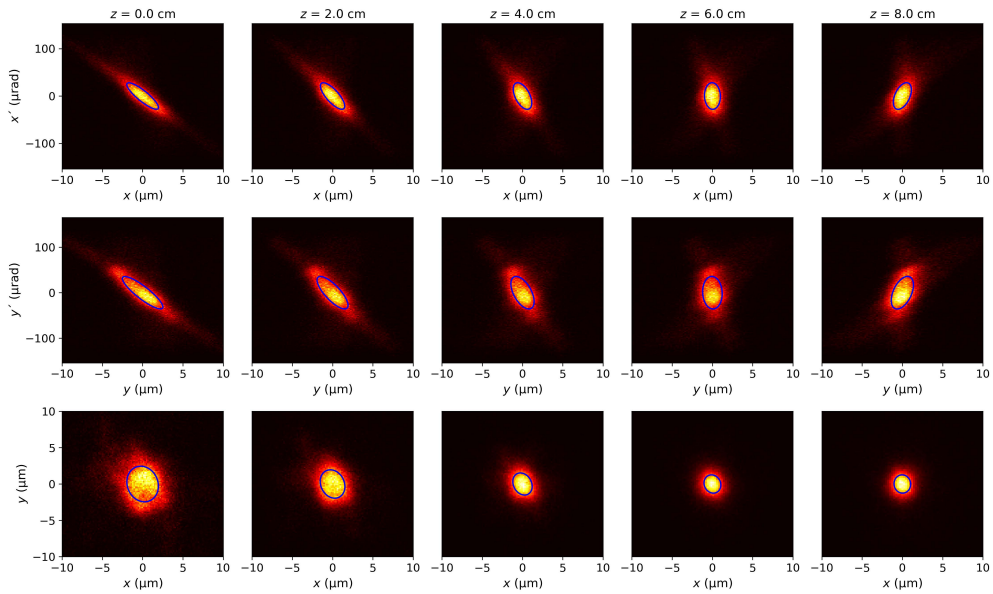


Figure 3.6: 2D histograms of the phase space reconstructed from wire scan measurements. Sub-plots in the same column correspond to the same z location. The first row shows the $x - x'$ and the second row shows the $y - y'$ phase space. The last row depicts the corresponding beam profile ($x - y$). The 1σ -ellipse of a 2D Gaussian fit is drawn in blue for each histogram.

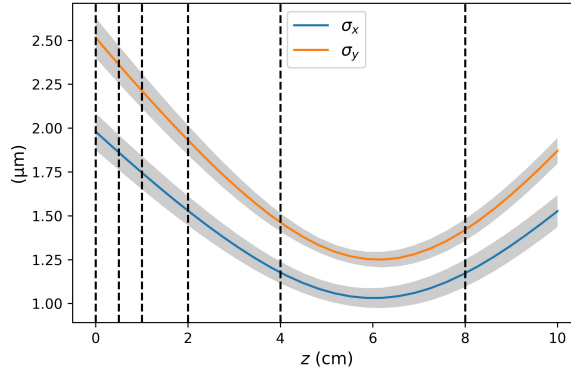


Figure 3.7: Evolution of the reconstructed beam size around the waist. The dashed vertical lines indicate wire scan measurement locations along z . At each of the six locations wire scans are carried out along nine different angles. Since we expected the waist to be around $z = 0$ cm, the distance between measurements is reduced here.

3.5 Discussion

The reconstructed phase space represents the average distribution of many shots, since shot-to-shot fluctuations in the density cannot be characterized with multi-shot measurements like wire scans. Errors induced by total bunch charge fluctuations and position jitter of the electron beam could be corrected for by evaluating beam-synchronous BPM data. Since the BPMs in the Athos branch were still uncalibrated, their precision was insufficient to correct orbit jitter in our measurement. This issue is considered further in Appendix 3.7.1.

The expected waist is located at the center of the chamber ($z = 0$ cm), whereas the reconstructed waist is found 6.2 cm downstream. In addition, the β -function at the waist (β^*) was measured to be around 3.6 cm in both planes, which is in disagreement with the design optics ($\beta_x^* = 1$ cm, $\beta_y^* = 1.8$ cm). This indicates that the beam is mismatched at the chamber entrance and improving the matching of the electron beam to the focusing lattice could provide even smaller (sub-micrometer) beams in the ACHIP chamber.

The reconstructed normalized emittances are up to a factor of two larger than the normalized emittances measured after the second bunch compressor. This emittance increase can be attributed to various reasons. Within a distance of 103 m the electron

beam is accelerated from 2.3 GeV (conventional emittance measurement) to around 3.2 GeV and is directed to the Athos branch with a fast kicker and a series of bending magnets. Chromatic effects in the lattice, transverse offsets in the accelerating cavities or leaking dispersion from dispersive sections in the switch-yard can lead to a degradation of the emittance along the accelerator. These effects were not precisely characterized and corrected before the measurement, since the priority was to validate a new method for transverse phase space characterization of a strongly focused ultra-relativistic electron beam.

Another possible explanation for the discrepancy of the emittances: the conventional emittance measurement uses the horizontal and vertical beam profiles measured for different phase advances (quadrupole currents) with a scintillating screen (single-shot). A Gaussian fit to the beam profiles at each phase advance is used to estimate the emittance [Pra14]. In contrast, the tomographic wire scan technique presented here reconstructs the transverse phase space averaged over many shots. Afterwards, a Gaussian fit estimates the area of the distribution in the transverse phase space. Both large shot-to-shot jitter and non-Gaussian beams can give rise to differences between the results of the two techniques.

The wire scan acquisition time could be reduced by using fewer projection angles. This could be done, if less detailed information on the beam distribution is acceptable, e.g., if only projected beam sizes are of interest, two projection angles are sufficient. The optimal number of angles depends on the internal beam structure and the beam quantities of interest.

3.5.1 Resolution Limit

The ultimate resolution limit of the presented tomographic characterization of the transverse beam profile depends on the roughness of the wire profile. With the current fabrication process, this is on the order of 100 nm estimated from electron microscope images of the free-standing gold wires. This is one to two orders of magnitude below the resolution of standard profile monitors for ultra-relativistic electron beams (YAG:Ce screens) [Isc+15; Max+17].

3.5.2 Comparison to other Profile Monitors

The scintillating screens (YAG:Ce) at SwissFEL achieve an optical resolution of 8 μm , and the smallest measured beam sizes are 15 μm [Isc+15]. At the Pegasus Laboratory at UCLA beam sizes down to 5 μm were measured with a 20 μm thick YAG:Ce screen

in combination with an in-vacuum microscope objective [Max+17]. Optical transition radiation (OTR) based profile monitors are only limited by the optics and camera resolution [TS99]. At the Accelerator Test Facility 2 at KEK this technique was used to measure a beam size of 750 nm [Bol+15]. However, OTR profile monitors are not suitable for compressed electron bunches (e.g., at FELs) due to the emission of coherent OTR [Akr+08].

At the SLAC Final Focus Test Beam experiment a laser-Compton monitor was used to characterize a 70 nm wide beam along one dimension [Bal+95]. The cost and complexity of this system, especially for multi-angle measurements, are its main drawbacks.

Concerning radiation hardness of the nano-fabricated wire scanner, tests with a single wire and a bunch charge of 200 pC at a beam energy of 300 MeV at SwissFEL did not show any sign of degradation after repeated measurements [Orl+20].

3.6 Conclusion

In summary, we have presented and validated a novel technique for the reconstruction of the transverse phase space of a strongly focused, ultra-relativistic electron beam. The method is based on a series of wire scans at different angles and positions along the waist. An iterative tomographic algorithm has been developed to reconstruct the transverse phase space. The technique is validated with experimental data obtained in the ACHIP chamber at SwissFEL. The method could be applied to other facilities and experiments, where focused high-brightness electron beams need to be characterized, for instance at plasma acceleration or DLA experiments for matching of an externally injected electron beam, emittance measurements at future compact low-emittance FELs [Ros+20], or for the characterization of the final-focus system at a high-energy collider test facility. For the latter application, the damage threshold of the free-standing nano-fabricated gold wires needs to be identified and radiation protection for the intense shower of scattered particles needs to be considered. Nevertheless, the focusing optics could be characterized with the presented method using a reduced bunch charge.

Acknowledgments

We would like to express our gratitude to the SwissFEL operations crew, the PSI expert groups, and the entire ACHIP collaboration for their support with these experiments.

We would like to thank Thomas Schietinger for careful proofreading of the manuscript. This research is supported by the Gordon and Betty Moore Foundation through Grant GBMF4744 (ACHIP) to Stanford University.

3.7 Appendix

3.7.1 Error Estimation

Position Errors

The uncertainty of the position of the wire scanner with respect to the electron beam is affected by the readout precision of the hexapod (< 1 nm), vibrational motion of the hexapod (< 10 nm) and position jitter of the electron beam, which at SwissFEL is typically a few-percent of the beam size. The orbit of the electron beam is measured with BPMs along the accelerator. Unfortunately, the BPMs along the Athos branch of SwissFEL have not been calibrated (the measurement took place during the commissioning phase of Athos). Nevertheless, we tried correcting the orbit shot-by-shot based on five BPMs and the magnetic lattice around the interaction point. However, it does not reduce the measured beam emittance, as their position reading is not precise enough to correct orbit jitter at the wire scanner location correctly. Therefore, we do not include corrections to the wire positions based on BPMs. The reconstructed beam phase space represents the average distribution for many shots including orbit fluctuations. After the calibration of the BPMs in Athos we plan to characterize the effect of orbit jitter to wire scan measurements in detail.

Amplitude Errors

Jitter to the BLM signal is introduced by read-out noise of the PMT ($< 1\%$), charge fluctuations of the machine and halo-particles scattering at other elements of the accelerator. The charge measured by the BPMs fluctuated by 1.3% (rms) during the measurement. The signal-to-noise ratio (SNR) of the measurements varies from 25 to 45 depending on the respective projected beam size. We define the SNR as: $s_{\max}/\sigma_{\text{noise}}$, where s_{\max} is the maximum of the signal and σ_{noise} refers to the standard deviation of the background.

Uncertainty of the Reconstruction

Due to the error sources mentioned above the measured projections are not fully compatible with each other, i.e., the reconstructed distribution cannot match to all measured data points. The error of the reconstructed phase space density and the derived quantities is estimated by a procedure similar to the main reconstruction algorithm. The reconstructed distribution is now taken as input. Instead of averaging over all projections, the iteration is performed for each projection individually. Hence, a set of $n_z \times n_\theta$ distributions is generated, in which each distribution matches best to one measured projection. All derived quantities, such as the emittance or β -function, are computed for each distribution and the error is taken as the standard deviation of this set.

3.7.2 Termination Criterion for Reconstruction Algorithm

The algorithm to reconstruct the phase space from wire scan measurements iteratively approximates the distribution that fits best to all measurements (see Sec. 3.3). The iteration is stopped when a criterion based on the relative change from the current to the previous iteration is reached. We define p_k as the average probability for a particle to be added or removed to the ensemble in iteration k .

$$p_k = \frac{1}{n_p n_\theta n_z} \sum_{i,\theta,z} |\Delta_{z,\theta}^i| \quad (3.8)$$

The iteration terminates when the relative change of p_k reaches a tolerance limit τ :

$$\frac{|p_k - p_{k-1}|}{|p_k|} < \tau \quad (3.9)$$

For the case of the presented data set $\tau = 0.005$ is found to provide stable convergence and a consistent solution. Around 110 iterations are required to reach the termination criterion.

3.7.3 Reconstruction of non-Gaussian Beams

Our particle based tomographic reconstruction algorithm does not assume any specific shape for the density profile. Therefore, asymmetric density variations, such as tails of a localized core can be reconstructed. To demonstrate this capability of our tomographic

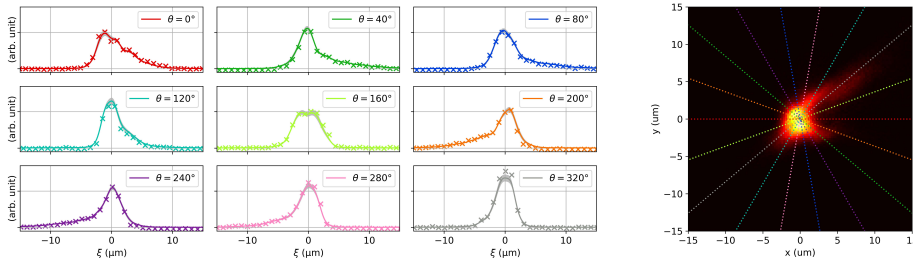


Figure 3.8: Tomographic reconstruction of a beam with non-Gaussian tails. The nine measured projections are indicated by crosses in the small nine sub-plots. The reconstruction result is shown in the larger sub-plot on the right (x,y profile). The projections of the reconstruction are shown as solid lines in the corresponding sub-plots. The colors correspond to the different projection angles as indicated by dashed lines in the 2D profile plot on the right. The tomographic reconstruction is able to represent the core and tails of the beam.

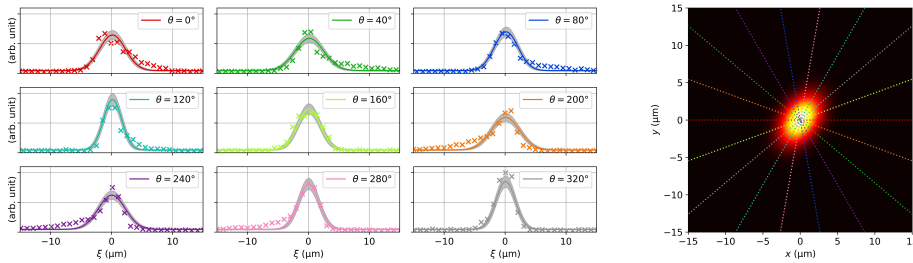


Figure 3.9: The result of a single Two-dimensional Gaussian fit to approximate nine measured projections. The measurement and the beam profile are shown analogously to the tomographic result shown in Fig. 3.8. In contrast to the tomographic reconstruction, the Gaussian fit is not able to represent the tails correctly.

technique, we show here a measurement of a non-Gaussian beam shape and compare the result to a 2D Gaussian fit. This measurement was performed with different machine settings than the measurement presented in Sec. 3.4. The electron bunch carried a charge of around 10 pC. The transverse beam profile was characterized with nine wire scans at different angles at one z position. Therefore we can only reconstruct the two-dimensional (x,y) beam profile. The measurement and the tomographic reconstruction are shown in Fig. 3.8. For comparison, we add the result of a single two-dimensional Gaussian fit to all nine measured projections (Fig. 3.9). The core and tails observed in the measurement are well represented by the tomographic reconstruction, whereas the Gaussian fit overestimates the core region by trying to approximate the tails.

4

Dielectric Grating Wakefields

4.1 Introduction

The acceleration gradient of conventional radio-frequency accelerators is limited by vacuum breakdown in the metallic cavities to around 300 MeV [Bra+03]. High-gradient advanced accelerator concepts with demonstrated fields orders of magnitude larger are being developed at various laboratories for future, more compact accelerators. These concepts include plasma [ESL09] and dielectric structure [Eng+14] based schemes. The Accelerator on a Chip International Program (ACHIP) is a research collaboration funded by the Gordon and Betty Moore Foundation with the aim to develop a dielectric laser accelerator (DLA) towards scientific and industrial applications. A DLA is a photonic microstructure driven by infrared laser fields. Charged particles are accelerated inside a vacuum channel with apertures in the order of a single micrometer. The beam intensity for sub-relativistic DLAs is at the moment limited by the small acceptance of the structure and the emittance of available electron sources. Higher densities can be achieved in experiments using relativistic electron beams [Ces+18a]. Ultimately, self-fields of the beam limit the transmittable electron density before beam break-up [PB68] occurs.

In this chapter, we present the experimental characterization of wakefields inside a dielectric double grating made of fused silica with a periodicity of 50 μm and gaps covering the range from 10 μm to 100 μm . The grating gap increases slowly along the normally invariant direction. Wakefield simulations of this tunable double grating were initially performed with a Gaussian pulse excitation and indicate control of the wakefield amplitude within one order of magnitude [Ege20]. The experiments were carried out with the ACHIP experimental chamber [Fer+18; Pra+17] at SwissFEL, the free-electron laser (FEL) at PSI [Mil+17]. A low-emittance electron beam with a charge of 10 pC and an energy of 3.2 GeV is strongly focused into the double grating. The modulation by the wakefield is observed in the energy spectrum of the electron beam. We demonstrate the smooth tunability of the wakefield source making it a compact and cost efficient alternative for conventional beam shaping technologies for the longitudinal phase space (LPS) for special FEL applications. For instance, residual chirp reduction or short pulse generation by linearizing parts of the LPS and compressing it with a magnetic chicane before sending the beam into the undulators.

Wakefield experiments using dielectric lined tubes with a diameter of 100 μm have been performed at SLAC with a bunch charge of 3 nC and a beam energy of 28.5 GeV [TM08]. A maximum accelerating field of 16 GV/m has been observed before damage was in-

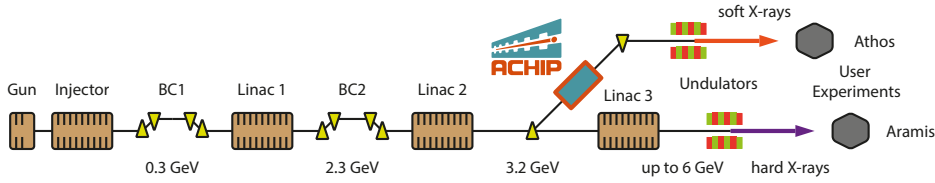


Figure 4.1: The free-electron laser SwissFEL at PSI. The ACHIP chamber is located in the switch-yard to the Athos beamline at a beam energy of 3.2 GeV. Sketch adapted from [Her+21].

duced to the material. Hence, we do not expect to reach the damage threshold in our experiment with a bunch charge of 10 pC.

4.2 Experimental Setup

4.2.1 Accelerator Setup

The bunch charge is lowered to 10 pC by reducing the laser aperture and pulse energy of the cathode laser. The nominal charge per bunch at SwissFEL is 200 pC. The reduced charge allows us to intersect the beam fully with the 40 mm long dielectric structure without reaching the limits of the radiation protection system of the SwissFEL facility. During the alignment of the double grating, it is unavoidable that the beam intersects the structure. The beam emittance was optimized by lowering the gun solenoid current to account for the reduced space charge forces at the reduced charge of 10 pC. The emittance is measured with a quadrupole scan and a scintillating screen after the laser heater at a beam energy of 150 MeV [Pra14]. The normalized emittance was minimized to around 110 nmrad in the horizontal and vertical plane.

For the dielectric grating wakefield studies, a current profile with a strong peak in the head which excites the wakefield followed by a longer tail would be beneficial, since it allows us to excite strong wakefields while covering a longer range of the wakefield response. Such current configurations are achieved with non-linear compression by changing the amplitude of the X-band cavity in the injector, which is normally used to remove second order contributions to the chirp. Lowering the X-band amplitude by 25 % from its nominal value results in an increased chirp in the head of the bunch forming a current spike after compression of the LPS with a magnetic chicane (second bunch compressor of SwissFEL). More information on the non-linear LPS setup and characterization can be found in Sec. 4.4.1.

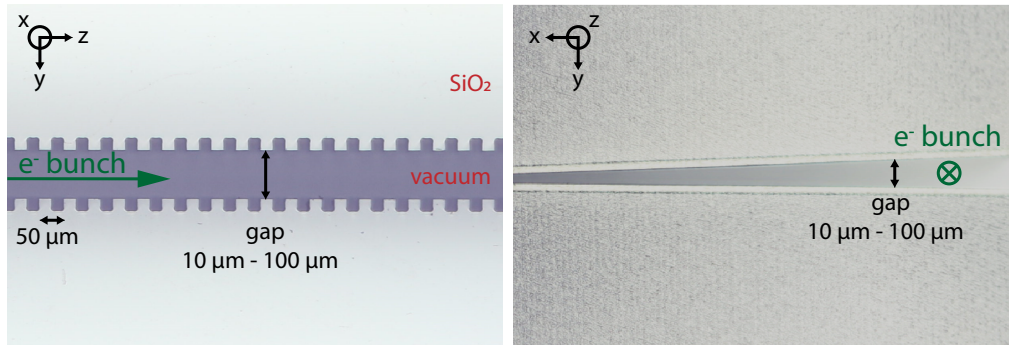


Figure 4.2: Optical microscope image of the fused silica double grating manufactured by FEMTOprint [FEM]. The period of the structure is $50\ \mu\text{m}$ and the gap is linearly changing from $10\ \mu\text{m}$ to $100\ \mu\text{m}$ along the normally invariant direction (x).

4.2.2 ACHIP Chamber

The ACHIP interaction chamber is installed in the Athos branch of SwissFEL at PSI (see Fig. 4.1). The main purpose of the chamber is to support DLA research and development [Fer+18; Pra+17]. A possible application of DLA technology for FELs is the generation of a micro-bunched pulse train using laser-based energy modulation followed by magnetic compression [Her+19].

The electrons at the ACHIP interaction point at SwissFEL possess a mean energy of $3.2\ \text{GeV}$ and are strongly focused by an in-vacuum permanent magnet triplet [Pra+17]. A six-dimensional positioning system (hexapod) at the center of the chamber is used to exchange, align, and scan samples or diagnostics.

A wire scanning tool consisting of nine nano-fabricated wires allows to measure beam sizes with sub-micrometer resolution. A tomographic reconstruction algorithm was developed to reconstruct the transverse phase space from wire scans at different angles and longitudinal positions around the waist [Her+21].

Using the wire scan tomography at the interaction point, we measured a beam size (root-mean-square (rms) of a Gaussian fit) of $2.1\ \mu\text{m}$ (vertical) and $4.1\ \mu\text{m}$ (horizontal) for the beam used for the wakefield measurements.

4.2.3 Wakefield Structure

The dielectric wakefield structure under study is a regular double grating made of fused silica with a periodicity of $50\ \mu\text{m}$ and a grating depth of $25\ \mu\text{m}$. It is a scaled version

of typical geometries that have been used for relativistic DLAs driven by infrared lasers [Ces+18a; Per+13]. For the structure used in the experiments presented here, the gap of the grating changes linearly from $10\ \mu\text{m}$ to $100\ \mu\text{m}$ over a total height of $2\ \text{mm}$ (along the open direction of the gap). This allows us to smoothly tune the wakefield interaction strength by adjusting the position of the grating with respect to the electron beam, which is essential for beam shaping applications for FELs. We do not expect the slowly changing gap to affect the local wakefield interaction significantly, since the gap changes marginally within typical dimensions of the electron beam (few μm). The structures used in this study have been fabricated by FEMTOprint [FEM], an EPFL spin-off commercializing free-form manufacturing of glass with a laser etching process with achievable surface roughness of around $100\ \text{nm}$. Two microscope images from the top and front perspective of the tunable double grating structure are shown in Fig. 4.2. The entire structure consists of 800 periods resulting in a total length of $40\ \text{mm}$. The geometric acceptance angle of the structure at the smallest gap is just $0.25\ \text{mrad}$. The structure was aligned to the electron beam axis experimentally by first minimizing the losses (scattered particles) detected by down stream beam loss monitor. Second, the gap size observed during a position scan was maximized iteratively by adjusting the tilt of the hexapod. We found optimal transmission at an angular offset of $1.2\ \text{mrad}$ between the z -axis of the grating mounted on the hexpod and the electron beam axis. This is within the expected tolerances of the sample mounting system described in Sec. 2.2.

4.3 Experimental Results

The energy spectrometer for the electron beam is a scintillating screen (YAG:Ce) in a dispersive section of the switch-yard downstream of the ACHIP chamber. The horizontal axis is dispersive and is thus proportional to the energy of the electrons. Modulations of the LPS lead to deformations of the spectrum (horizontal projection on screen). Transverse kicks in the horizontal direction (dispersive on screen) cannot be distinguished from longitudinal kicks. Therefore, we decided to mount the grating with its open direction being horizontal. Even though the gap changes along this direction, we expect this asymmetry to not cause significant horizontal kicks since the change of the gap is negligible within the length of the measured beam size ($4.1\ \mu\text{m}$). However, transverse kicks in the vertical direction can be expected from off-centered beams. These kicks result in a vertical displacement along the beam. For illustration, Fig. 4.3 depicts typical spectrometer images with and without the wakefield structure

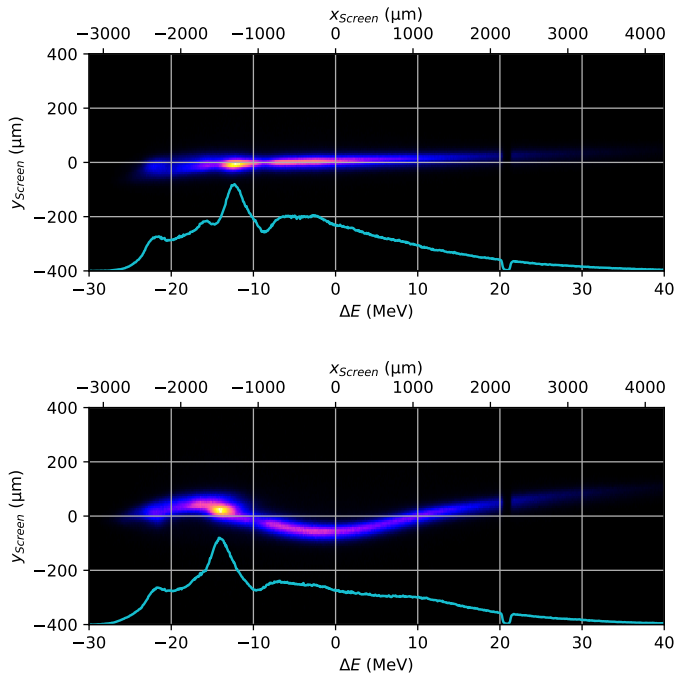


Figure 4.3: Typical spectrometer images. Top: without structure. Bottom: with structure off-centered (misalignment along y). The misalignment creates transverse wakefields seen as vertical modulations, whereas longitudinal wakefields modify the spectrum shown in cyan.

inserted. In the following, we summarize observations of longitudinal and transverse kicks and their dependence on the grating gap, beam offset and tilt.

4.3.1 Effect of Grating Gap

The gap of the double grating can be tuned smoothly by adjusting the horizontal position with the hexapod. Fig. 4.4 shows the spectrum of the beam without structure and for different gap dimensions ranging from $12.5 \mu\text{m}$ to $74.6 \mu\text{m}$. The spectrum without structure possesses clear modulations, which arise from longitudinal space charge (LSC) and coherent synchrotron radiation (CSR) effects of the high space-charge density in the bunch compressor and switch-yard of SwissFEL. We observe the main peak of the spectrum shifting to lower energies as the gap is decreased. At

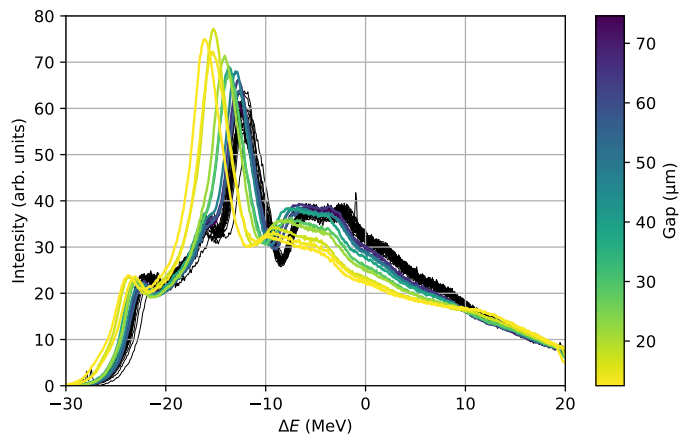


Figure 4.4: Measured spectra for different gaps ranging from 12.5 μm to 74.6 μm .

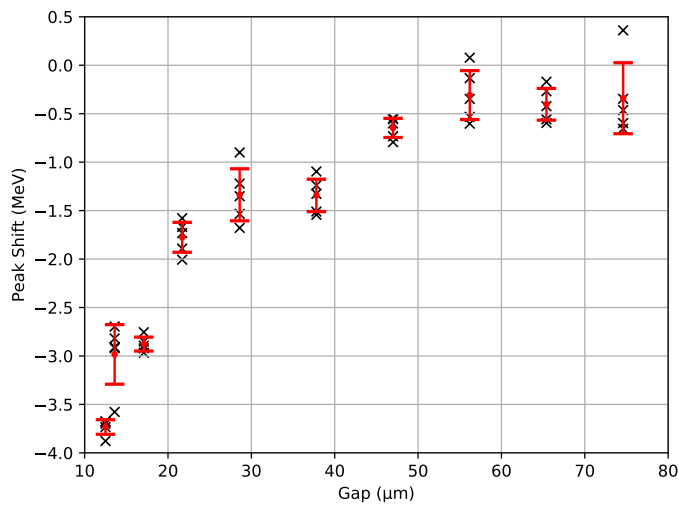


Figure 4.5: Measured shift of the primary peak of the spectrum as a function of gap size.

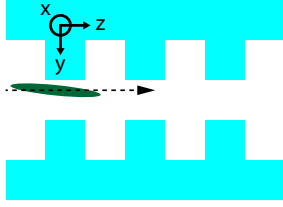


Figure 4.6: Illustration of a tilted beam passing off-centered through the double grating.

the high-energy tail we see a slight increase of density, also continuously increasing with decreasing gap. The shift of the main peak as a function of grating gap is shown in Fig. 4.5. A shift of around -3.7 MeV is observed for the smallest gaps ($12.5 \mu\text{m}$). This corresponds to average decelerating fields of 92.5 MV/m over the length of the structure (40 mm).

4.3.2 Effect of Beam Tilts and Offsets

We investigated the wakefield sensitivity on the transverse position close to the grating surface and studied how beam tilts affect the interaction. First order beam tilts considered here are correlations in the $t - y$ plane of the phase space at the interaction point. Fig. 4.6 illustrates a tilted beam passing off-centered through the double grating. In the beginning of the experimental shift, we observed that the transverse streaking effect of the structure was not symmetric for both directions of grating offsets and attributed this behaviour to a tilted beam breaking the symmetry. To affirm that this asymmetry is indeed caused by the beam tilt, we repeated the gap scan for a series of skew-quadrupole currents (I_Q). The skew-quadrupoles in the dispersive section of the bunch compressors are used to control the first order tilt of the beam at FELs [PLR15]. Fig. 4.7 depicts the transverse kick as a function of beam energy, i.e., the center of mass for vertical slices of the beam on the spectrometer screen for a scan across the gap. Comparing the transverse streaking for different skew-quadrupole currents reveals the dependence of the wakefield interaction on the beam tilt. For the case of $I_Q = -0.116$ A, the asymmetry of the wakefield streaking is minimal for the measured range of quadrupole settings. However, the natural tilt on the spectrometer (without wakefield streaking) is increased for this setting. This is attributed to the beam transport from the interaction point to the spectrometer screen, i.e., a tilt in $t - y'$ at the structure location (not affecting the symmetry of

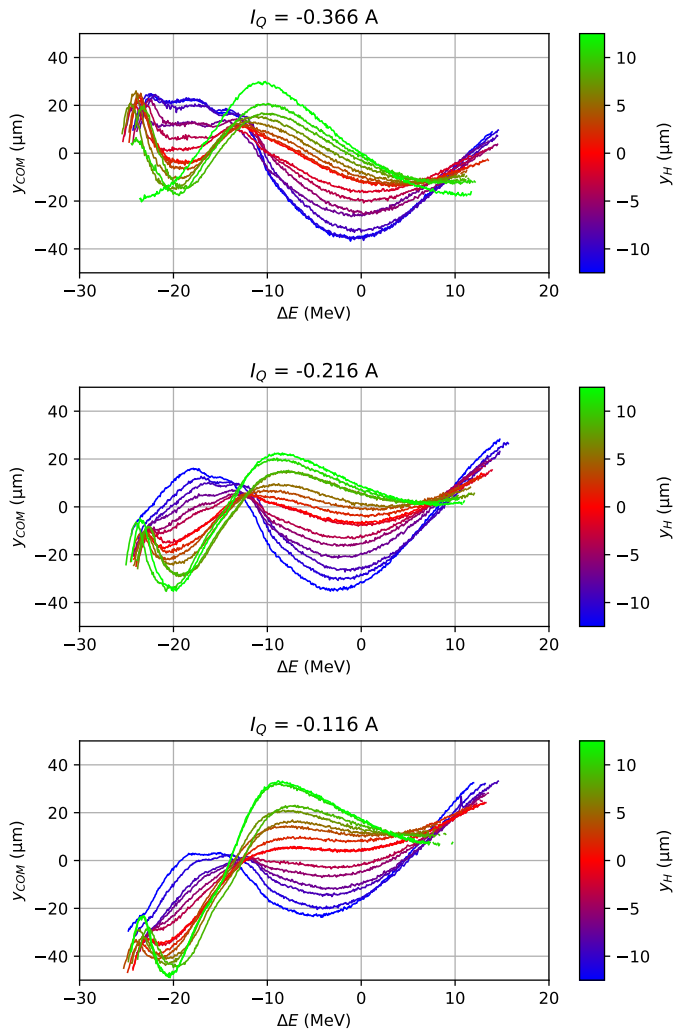


Figure 4.7: Transverse kick as a function of beam energy, i.e., the center of mass for vertical slices of the beam on the spectrometer screen for a scan across the gap. The three plots correspond to different skew-quadrupole currents (I_Q).

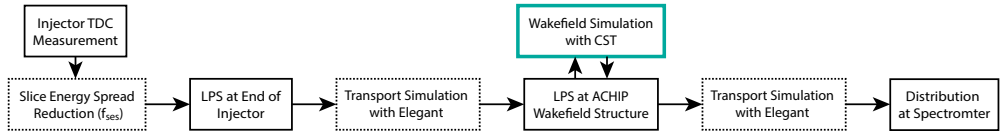


Figure 4.8: Flowchart of the simulation of the experiment.

the interaction) translates into a tilt in $t - y$ at the spectrometer location. This tilt manifests as a $E - y$ correlation on the spectrometer screen since the LPS of the beam couples t and E (see Sec. 4.4.1 for more details on the LPS). A 2D scan including both skew-quadrupole currents would enable us to cancel the tilt in both planes ($t - y$ and $t - y'$) simultaneously along the beamline.

4.4 Simulation of the Experiment

The LPS of the electron beam needs to be known at the location of the dielectric structure for the simulation of the experiment. The current profile is required as input to the wakefield simulation. The entire LPS is used to apply the time dependent modulation to the distribution. The simulation consists of particle tracking using Elegant [Bor00] and wakefield simulations using CST [CST19]. The CST wakefield calculations were performed in collaboration with Uwe Niedermayer and Thilo Egenolf* from TU Darmstadt (*now at GSI Darmstadt).

The entire workflow starting from the LPS measurement at the injector, tracking to the ACHIP chamber, CST wakefield calculation, and tracking to the spectrometer screen is illustrated in Fig. 4.8. Details of the LPS reconstruction and results of the wakefield simulation with CST are given in the following sections.

4.4.1 Longitudinal Phase Space Reconstruction

The standard tool for direct measurements of the LPS at FELs is a transverse deflecting cavity (TDC) in combination with a dipole spectrometer. SwissFEL has two TDCs, one after the first bunch compressor at the end of the injector and a second TDC at the end of Linac 3 before the Aramis undulators. A third transverse deflector with adjustable polarization in the Athos electron beamline is planned to be installed in 2021 [Cra+20]. For the experiments presented here, we extracted the LPS from the TDC measurement at the end of the injector (see Fig. 4.9) and simulated the beam transport along the

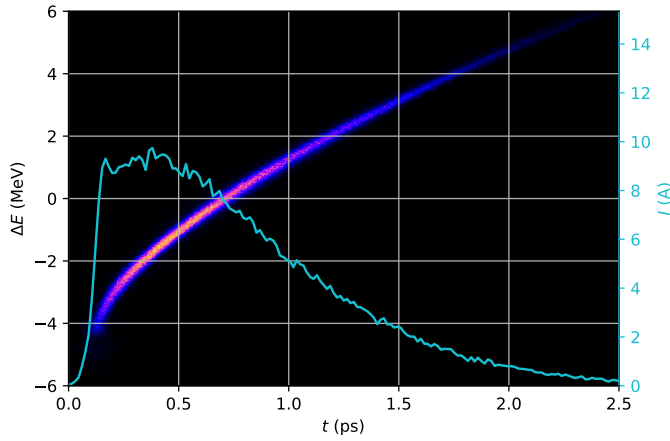


Figure 4.9: LPS observed with the TDC at the SwissFEL injector spectrometer (beam energy: 300 MeV). The X-band (linearizer) amplitude has been decreased by 25 % from its nominal value to keep the non-linearity in the head (left).

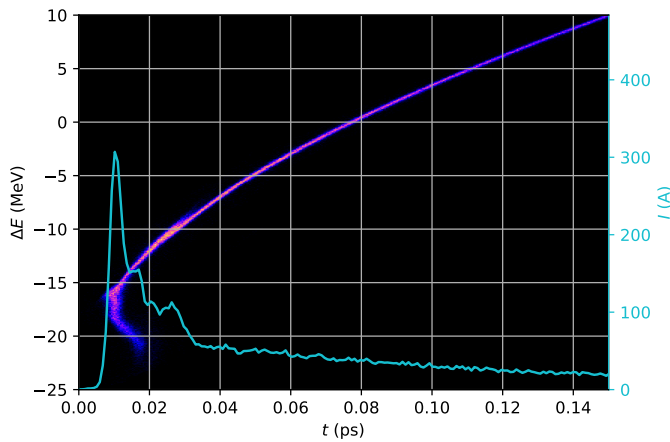


Figure 4.10: LPS after transport up to the ACHIP chamber (beam energy: 3.2 GeV). The simulation is performed with Elegant [Bor00] including LSC and CSR effects based on the injector LPS measurement (Fig. 4.9) with reduced slice energy spread ($f_{ses} = 0.175$, see Eq. 4.1).

machine up to the ACHIP chamber and spectrometer screen with Elegant [Bor00]. Elegant has the capability to calculate LSC and CSR effects [Bor01; Hua+04; SSY97]. These numerical methods are not full 6D space charge simulations but approximations needed for the simulation of beamlines hundreds of meters long. These numerical models have been bench marked with measurements at FELs, e.g., LCLS at SLAC [Ban+09]. The initial slice energy spread of the beam strongly affects the strength of LSC and CSR effects. The slice beam size as measured with the injector TDC and the spectrometer screen corresponds to a slice energy spread of 150 keV. A detailed study of the slice energy spread at SwissFEL reported a slice energy spread of 7.1 keV for a bunch charge of 10 pC [Pra+20]. This study was done with the uncompressed electron beam, whereas the beam was compressed by around a factor of ten for the measurements presented here. Including these differences in the compression setup, we conclude that the measurement of the slice energy spread is resolution-limited. We reduced the slice energy spread of the initial distribution according to the following relation:

$$\sigma = f_{ses} \sqrt{\sigma_{meas}^2 - \sigma_{res}^2}, \quad (4.1)$$

where σ_{meas} is the measured slice energy spread as seen on the spectrometer screen, σ_{res} is the resolution of the spectrometer imaging system, and f_{ses} accounts for multiple effects limiting the resolution of the measurement. These effects include the natural beam size on the screen which can be enlarged due to a mismatch of the beam, and the increase of the slice energy spread due to the finite beam size inside the TDC. In principle, the contributions of these effects could be distinguished by repeating the LPS measurement at different beam energies since they depend with different orders on the beam energy. This technique is demonstrated in [Pra+20]. Due to beam time limitations it was not possible to repeat this study for the machine parameters used for the wakefield experiment presented here. Therefore, the initial slice energy spread was empirically reduced with the factor f_{ses} (Eq. 4.1) by comparing the simulated spectrum to the measurement. With the slice compression of the LPS, inhomogeneities cannot be recovered correctly. How this might affect the reconstructed current profile is discussed in Sec. 4.5.

Fig. 4.11 shows the measured spectrum and the simulated distribution at the spectrometer screen for different values of f_{ses} . As expected, the modulation due to CSR and LSC effects increases with decreasing f_{ses} . Not all features, especially at the low energy end of the spectrum, could be recovered as seen in the measurement. The height of the main peak of the spectrum agrees with the measurement for f_{ses} around 0.175.

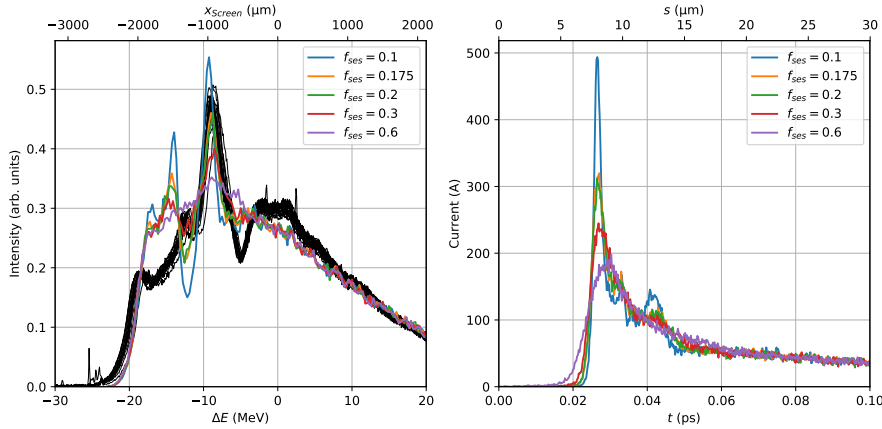


Figure 4.11: Simulated spectrum and current at the ACHIP location for different initial slice energy spreads (f_{ses}). The height of the main peak for $f_{ses} = 0.175$ agrees best with the measurement (black, 30 shots).

In addition, the accelerating phase (ϕ) of Linac 1 needed to be adjusted for the tracking simulation. Machine drifts over time might lead to a relative change of the phase with respect to the calibrated absolute phase values. Fig. 4.12 compares the simulated spectrum to the measurement for relative phase offsets ($\Delta\phi$). The phase of the reference settings for the simulations corresponding to $\Delta\phi = 0^\circ$ is 71.53° whereas the applied phase for the measurement was 70.53° . The position of the main peak within the spectrum matches best with the measurement for $\Delta\phi$ around -1.7° . This corresponds to a relative phase offset of -0.7° during the measurement, which is an expectable offset since the machine was not phased before the shift. The reconstructed current profile for $f_{ses} = 0.175$ and $\Delta\phi = -1.7^\circ$ reaches a peak current of about 300 A, with a full-width-half-maximum (FWHM) of around 6 fs.

4.4.2 CST Wakefield Simulations

The interaction with the dielectric structure is modeled in CST Particle Studio [CST19], a widely used finite integration technique for Maxwell's equations. In a first approximation, the beam is treated as a line charge in the center of the gap. The simulated time dependent longitudinal wake kick is interpolated at the longitudinal particle coordinates of the reconstructed LPS. The modulated LPS is then tracked to the spec-

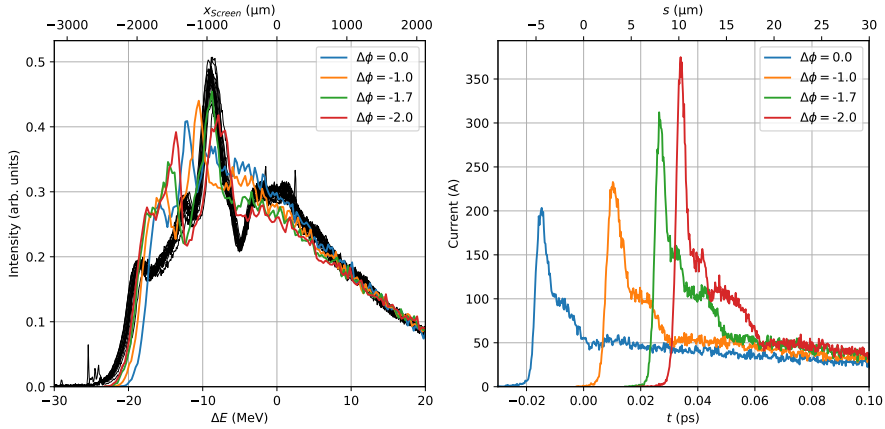


Figure 4.12: Simulated spectrum and current at the ACHIP location for different Linac 1 phase offsets ($\Delta\phi$). The location of the main peak for $\Delta\phi = -1.7^\circ$ agrees best with the measurement (black, 30 shots). The slice energy spread parameter f_{ses} was set to 0.2 for this scan.

trometer screen with Elegant. The simulated shift of the peak of the spectrum for different gap sizes is depicted in Fig. 4.14 and is around a factor of three larger than observed in the experiment. For the initial CST wakefield simulation, the number of periods was set to 15, which was found to be sufficient in a previous study on intensity effects in DLAs [ENB20]. The mesh-size of this simulation was $0.25\ \mu\text{m}$ (uniform and isotropic), which corresponds to eight sampling points within the FWHM of the reconstructed current profile. This is insufficient to represent the current accurately in the simulation. In the subsequent sections we investigate and distinguish numerical and physical effects that could contribute to the discrepancy between experiment and simulation, e.g., the effect of the mesh size, number of simulated periods, initial slice energy spread or finite beam size. These simulations are carried out only for the small grating gap of $14.5\ \mu\text{m}$, since the wakefield effect is strongest and the simulation domain is significantly reduced as compared to larger gaps.

Mesh Size

The mesh discretizes the geometry of the structure and needs to be small enough to resolve the dielectric structure and the electron bunch accurately. The current spike has a FWHM of around 6 fs, or $1.8\ \mu\text{m}$, which is much shorter than the periodicity of

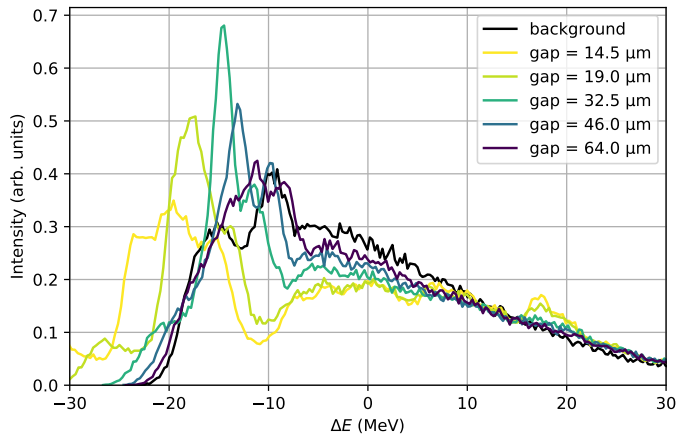


Figure 4.13: Simulated spectra for different gap sizes. The background (black) represents the simulated spectrum without wakefields from the dielectric grating.

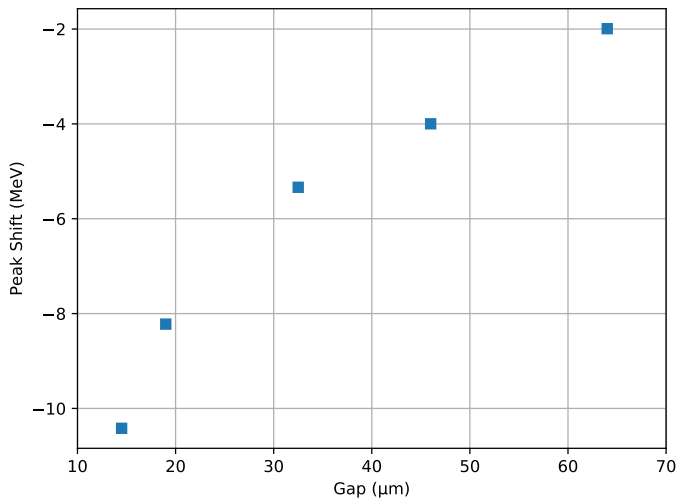


Figure 4.14: Simulated shift of the primary peak of the spectrum as a function of gap size. Three times larger shifts than in the experimental result shown in Fig. 4.5.

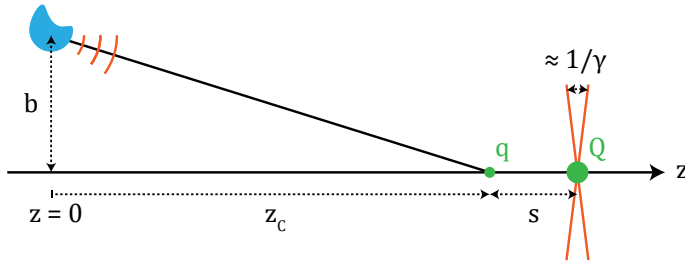


Figure 4.15: Sketch of the wakefield catch-up. The catch-up distance z_c is the distance required for the field from a driving charge Q scattered at an object at a distance b to reach a trailing witness charge q separated by s . Charges are moving relativistically to the right. This sketch is made based on [Wil89].

the structure ($50 \mu\text{m}$) and therefore more relevant for the required mesh size. In order to evaluate the numerical error, we studied the variation of the computed wakefield for different mesh sizes (Fig. 4.16). We observe, that the wakefield amplitude is not affected by more than 10 % when changing the mesh size from $0.5 \mu\text{m}$ to $0.1 \mu\text{m}$, but the rise time of the wakefield is clearly larger for the largest mesh size, i.e., the current spike is not well resolved. A mesh size of $0.125 \mu\text{m}$, seems to be sufficient to call the wake potential converged. We conclude, that the observed mismatch of the peak shift between the experiment and simulation cannot be explained by insufficient mesh resolution.

Number of Simulated Periods

To accurately estimate the wakefield per period of a long structure, the simulated number of periods (n_p) needs to be large enough, such that edge effects at the entrance and exit are negligible. As indicated by a previous study on intensity effects in DLAs [Ege20], 10 to 15 periods should suffice. Another requirement for the simulation is given by the so-called catch-up distance (z_c), a geometrical estimation of how far the field needs to be propagated to interact with a test particle at a distance s from the source charge. It is approximately:

$$z_c \approx \frac{b^2 - s^2}{2s}, \tag{4.2}$$

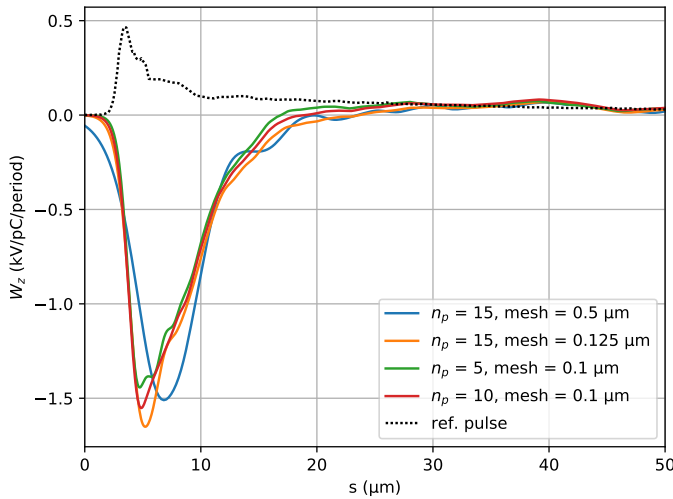


Figure 4.16: Simulated longitudinal wakefield for different mesh sizes and number of periods (n_p).

where b is the distance of the scattering object to the beam axis [Wil89]. This concept is illustrated in Fig. 4.15. For a length equal to the FWHM of the current spike ($1.8 \mu\text{m}$) and $b = 7.25 \mu\text{m}$, the catch-up distance is $z_c \approx 13.7 \mu\text{m}$ being much shorter than the total simulation length. We confirmed that the wakefield amplitude does not change more than 10% when varying the number of simulated periods from 5-15, see Fig. 4.16. We conclude that it is not necessary to simulate a larger number of periods at the current level of mismatch between experiment and simulation.

Finite Beam Size

The initial model neglected the transverse extent of the beam. The wakefield was calculated for a line current and the resulting time dependent wake was applied homogeneously across the transverse coordinates. The rms beam sizes measured in the beginning of the experimental shift were $2.1 \mu\text{m}$ (vertical) and $4.1 \mu\text{m}$ (horizontal). In order to evaluate the effect of the finite transverse beam extent we studied the variation of the wakefield for transverse offsets of the witness beam. The results are summarized in Fig. 4.17. We observe that horizontal offsets (Δx) lead to a reduction, whereas vertical offsets (Δy) lead to a slight increase of the wakefield amplitude. In

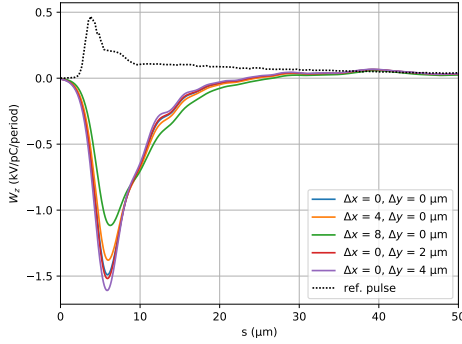


Figure 4.17: Simulated longitudinal wakefield for horizontal and vertical offsets of the witness beam.

addition, the beam was larger in the horizontal plane making the dependence on Δx more important.

To assess the effect of the finite beam size on the spectrum, we convolved the wakefield as a function of Δx with a Gaussian profile corresponding to the beam extent in the horizontal plane. Afterwards, the time- and now also position dependent wake is added to the LPS which is then tracked to the spectrometer using Elegant. The resulting spectrum for three different beam sizes is shown in Fig. 4.18. We observe that a larger beam leads to a reduced peak shift, since the average wakefield amplitude is smaller. However, even for a beam size of $12.6 \mu\text{m}$, three times larger than measured, the peak of the spectrum is still shifted by about 8 MeV. A transverse beam size of several μm is relevant and the offset dependent longitudinal wakefield should be taken into account, but the effect is too small for the measured beam size of $4.1 \mu\text{m}$ to be solely responsible for the mismatch to the experimental result.

Slice Energy Spread

The slice energy spread of the initial distribution used for the Elegant tracking to the ACHIP chamber is crucial for the simulation of LSC and CSR effects and the resulting LPS, see Sec. 4.4.1. Since the LSC and CSR modules of Elegant are only approximations, there could be a systematic error in the particle distribution used for the wakefield simulation with CST. To assess, whether the slice energy spread reduction factor (f_{ses}) could explain the discrepancy between experiment and simulation, we simulated the wakefield interaction for a larger slice energy spread. Instead of $f_{ses} = 0.2$ as used

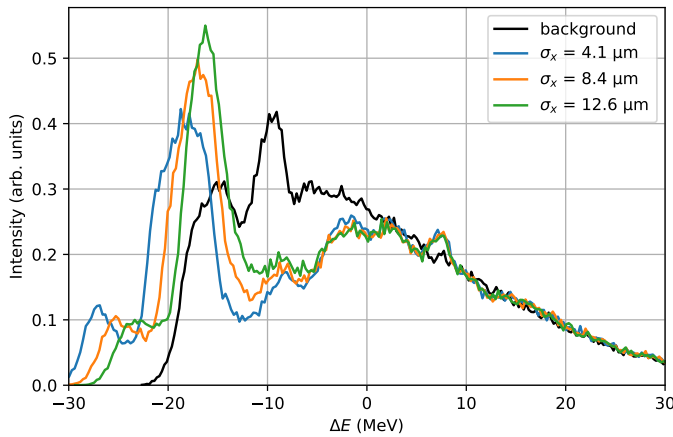


Figure 4.18: Simulated spectra for different beam sizes. The transverse extent of the beam leads to a weaker average wakefield and therefore reduced peak shift.

previously, we compare here the case for a three times larger initial slice energy spread: $f_{ses} = 0.6$. The resulting spectrum with and without wakefield is shown in Fig. 4.19. The spectrum without the wakefield has now a lower peak, matching worse to the measured spectrum, compare Fig. 4.5. Moreover, the simulated shift of the peak is still about three times larger than what was observed experimentally.

Relative Permittivity

The relative permittivity (ϵ_r) for fused silica is around 2.1 for wavelengths in the range from $0.5 \mu\text{m}$ to $7 \mu\text{m}$ [KPJ07a], which contains a large portion of the spectrum of the current profile of the electron bunch (FWHM = $1.8 \mu\text{m}$). We studied the effect of a variation of the relative permittivity on the wakefield with simulations. Only a little dependence is found: The wakefield amplitude changes by 50 % when ϵ_r is reduced heavily to 1.22, see Fig. 4.20. A possible explanation for this weak dependence is that the total wake effect is dominated by the Smith-Purcell wake caused by scattering fields at the grating surface. The Cerenkov wake due to fields propagating inside the dielectric is smaller. The Smith-Purcell wake is dominated by the geometry of the surface and not as much by the refractive index. A similar observation was made in [Ege20]. Here, the dielectric grating wakefield was compared to the analytical solution of a perfectly conducting grating [Ban+09], where only the Smith-Purcell

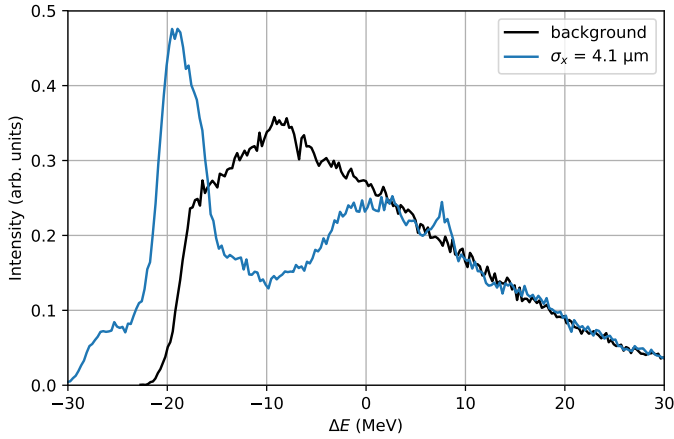


Figure 4.19: Simulated spectra for larger initial slice energy spread ($f_{ses} = 0.6$).

wake is present as no fields penetrate into the material. Since we cannot expect large deviations of the relative permittivity found in literature, for instance in [KPJ07a], the dependence on the relative permittivity cannot explain the discrepancy between simulation and experiment.

4.5 Summary and Discussion

We have achieved the transmission of a non-linearly compressed bunch with a charge of 10 pC through a 40 mm long dielectric double grating without significant losses. Inspection with an optical microscope after the measurement did not show signs of degradation or damage to the fused silica structure due to heating or direct irradiation during alignment. The aperture of the double grating was scanned from 12.5 μm to 75 μm and we observed the gap-dependent effect of the wakefield modulation with an electron spectrometer. For the smallest aperture a shift of the main peak of the spectrum of around 3.7 MeV was measured, which corresponds to an average gradient of 92.5 MV/m. The demonstrated tunability is an important feature for beam shaping applications at FELs.

The transverse wakes created when the grating is off-centered, could be used to select slices of the beam that drive the lasing process in the undulators, which leads to a reduced time of the FEL pulse. This is similar to the scheme described in [PLR15],

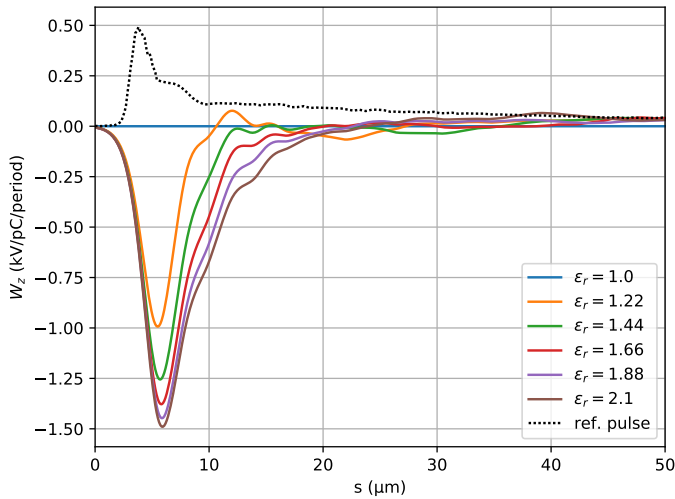


Figure 4.20: Simulation of longitudinal wakefield for different relative permittivities ϵ_r and a constant grating gap of $14.5 \mu\text{m}$. For fused silica we expect $\epsilon_r \approx 2.1$ in the relevant wavelength range. ($\epsilon_r = 1$ corresponds to vacuum, simulation was executed)

which uses linearly tilted beams in the undulators to shorten the FEL pulse.

Transverse tilts of the electron beam at the wakefield structure lead to asymmetric streaking when the grating is off-centered. This effect could be used as a diagnostic for precise beam tilt control at FELs.

The simulation of the experiment requires the reconstruction of the LPS at the interaction point. Since a TDC was not available in Athos at the time of the measurements, we used the LPS measured in the injector and performed a particle tracking with Elegant up to the ACHIP chamber and the spectrometer screen. The resulting distribution did not recover all features of the measured spectrum. The main peak of the spectrum could be recovered by reducing the initial slice energy spread of the distribution, which can be justified by the resolution of the LPS measurement and comparing the slice energy spread to another, more sophisticated method based on energy dependent scaling of the slice beam size in the spectrometer.

The simulation of the wakefield interaction using CST showed a discrepancy of almost a factor of three, when comparing the shift of the peak in the spectrum. We investigated a number of effects that could explain the discrepancy: Numerical parameters, such as the mesh and number of simulated periods, the finite beam size at the interaction

point, the initial slice energy spread and material parameters. However, agreement with the experiment could not be achieved with combinations of reasonable parameter variations.

A direct measurement of the LPS after the ACHIP chamber would greatly simplify the simulation efforts, since the LPS reconstruction would be more accurate and the wakefield modulation could be observed time-dependently. A new X-band TDC with fs-resolution will be installed in Athos in the near future [Cra+20], which would benefit these wakefield experiments enormously.

Additional studies to clarify the discrepancy between experiment and simulation could include the effect of the surface roughness on the wakefield interaction. For the structures made by FEMTOprint used in this experiment we expect a surface roughness in the order of 100 nm [FEM]. The effect of a distorted surface for a perfectly conducting beam pipe has been studied theoretically and an additional synchronous wakefield due to randomly distributed scattering objects was found [RWT01; Stu98]. However, this does not cover the effect of rough surfaces on the Smith-Purcell wakefield in dielectric double gratings.

The wavelength-dependent absorption of fused silica shows a strong peak at around 10 μm [KPJ07a]. This strong absorption would affect waves with longer wavelength than relevant for the driving current spike. Therefore, this absorption is not expected to alter the wakefield interaction much in this region of the LPS. In addition, the absorption affects the Cerenkov contribution to the wakefield only. The Smith-Purcell surface induced wakefield would not be affected by absorption inside the material. The effect of absorption in combination with surface roughness on the wakefield in a dielectric double grating could be investigated in a future study.

5

Optical Bunching in FELs Using Dielectric Laser Modulation

Laser-Driven Modulation of Electron Beams in a Dielectric Micro-Structure for X-Ray Free-Electron Lasers

Authors: Benedikt Hermann^{1,2}, Simona Bettoni¹, Thilo Egenolf³, Uwe Niedermayer³, Eduard Prat¹ and Rasmus Ischebeck¹

¹Paul Scherrer Institut, 5232 Villigen PSI, Switzerland

²Institute of Applied Physics, University of Bern, 3012 Bern, Switzerland

³Institute for Accelerator Science and Electromagnetic Fields (TEMF), TU Darmstadt, 64289 Darmstadt, Germany

Published: December 24, 2019. Scientific Reports, Volume 9, Article number: 19773.

DOI: <https://doi.org/10.1038/s41598-019-56201-8>

Abstract

We describe an application of laser-driven modulation in a dielectric micro-structure for the electron beam in a free-electron laser (FEL). The energy modulation is transferred into longitudinal bunching via compression in a magnetic chicane before entering the undulator section of the FEL. The bunched electron beam comprises a series of enhanced current spikes separated by the wavelength of the modulating laser. For beam parameters of SwissFEL at a total bunch charge of 30 pC, the individual spikes are expected to be as short as 140 as (FWHM) with peak currents exceeding 4 kA. The proposed modulation scheme requires the electron beam to be focused into the micrometer scale aperture of the dielectric structure, which imposes strict emittance and charge limitations, but, due to the small interaction region, the scheme is expected to require ten times less laser power as compared to laser modulation in a wiggler magnet, which is the conventional approach to create a pulse train in FELs.

5.1 Introduction

Free-electron lasers (FELs) make use of a highly compressed relativistic electron beam to generate electromagnetic radiation in a magnetic undulator. They are the brightest sources of radiation from the VUV [Ack+07; All+15] to the X-ray regime [Alt+06; Emm+10; Ish+12; Kan+17; Mil+17]. The emission of radiation in a so-called self-amplification of spontaneous emission (SASE) FEL grows exponentially from noise and critically depends on the local properties of the electron beam. A technique proposed to generate an individual or a train of sub-femtosecond X-ray pulses with

well-defined separation is the energy modulation of the electron bunch with a laser in the magnetic field of a resonant undulator. This "enhanced SASE" (ESASE) method has been proposed by Zholents [Zho05], and is being implemented at LCLS [Cof+19] and planned at other facilities such as SwissFEL [Abe+19].

In this paper, we present and compare an alternative method to the conventional undulator modulation scheme. We show, that by modulating the electron bunch in a laser-driven dielectric micro-structure, similar modulation strength can be achieved with significantly lower laser power. The beamline required for the proposed scheme is sketched in Figure 5.1. Key elements are the strong focusing and matching quadrupole triplets, the chicane for bunching and the FEL undulator section with interleaved chicanes acting as phase shifters. The intrinsic synchronization of the FEL pulses to an external laser, which is achieved in both schemes, naturally gives rise to pump-probe experiments. The CHIC scheme in the soft X-ray beamline in SwissFEL (Athos) makes use of magnetic chicanes between the undulator segments to delay the electron beam with respect to the X-Rays [Abe+19; Pra+16]. Athos is planned to deliver FEL radiation for wavelengths ranging from 0.65 nm to 5 nm from 2020 and user operation starting in 2021 [Abe+19]. Adjusting these chicanes to form overlap between each X-ray pulse with the subsequent slice of the electron bunch, the longitudinal coherence is transferred along the bunch, and the X-ray pulses become phase-locked [TM08]. The chamber for the interaction with the laser and dielectric structure is installed in the switchyard to Athos and is currently being commissioned. It is also planned to demonstrate GV/m gradients in these dielectric laser acceleration (DLA) structures with a length of 1 mm at a laser wavelength of 2 μm [Fer+18; Pra+17].

5.1.1 Modulation of Electron Beams in a Laser-Driven Dielectric Double Grating

Illuminating a dielectric double grating with a laser creates evanescent waves which travel inside the gap of the structure with a phase velocity defined by the periodicity of the structure and the wavelength of the illuminating laser. For a laser incident normal onto a straight grating a net interaction with a charged particle traveling along the gap is achieved if the resonance condition is fulfilled: $\lambda_S = \lambda_L \beta n$ [Eng+14]. Here, λ_S denotes the periodicity of the dielectric structure, λ_L is the wavelength of the laser, β is the normalized electron velocity and n is the order of the spatial harmonic of the evanescent wave. To sustain the interaction over distances greater than the laser pulse length, a pulse-front tilt setup for the laser has to be employed [Ces+18b; Koz+18; Wei+17]. Due to the optical phase dependence of the interaction, net-acceleration of

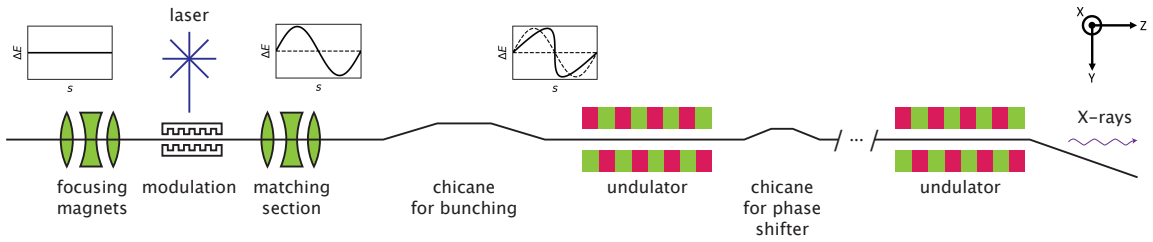


Figure 5.1: Schematic overview of the proposed scheme. Strong focusing is required to match the beam into the micrometer scale aperture of the dielectric grating. The longitudinal phase-space is modulated by the optical near fields in the dielectric structure excited by a laser. The energy modulation is converted into longitudinal bunching by a magnetic chicane. Three inset plots illustrate the longitudinal phase-space evolution. The resulting pulse train emits a series of homogeneously spaced x-ray pulses which can be mode-locked by small chicanes between undulator modules acting as phase shifters.

electrons can be achieved only for bunches significantly shorter than the wavelength of the driving laser. The momentum distribution of an electron beam longer than the laser wavelength will be modulated sinusoidally. The amplitude of the longitudinal interaction with the evanescent waves inside the channel of a straight grating is proportional to $\cosh(2\pi y/(\lambda_L \beta \gamma))$ and the transverse component of the interaction is proportional to $\sinh(2\pi y/(\lambda_L \beta \gamma))$ [NEB17]. As a result, the modulation amplitude becomes homogeneous over the entire gap and the transverse component vanishes for ultra-relativistic particles ($\gamma \gg 1$). Therefore, a straight grating illuminated by a laser polarized along the direction of the electrons creates an almost purely longitudinal momentum modulation. A resonant transverse momentum component can be added by tilting the grating [Nie+19]. In principle, the transverse momentum modulation can be used to bunch the beam by an appropriate compression setup using R_{52} (transfer matrix element relating transverse momentum changes to temporal deviations). However, compression of the transversely modulated beam leads to a slice emittance increase within the spikes. Since the SASE process strongly depends on the transverse slice emittance [Pra+14], we focus on longitudinal modulation only to avoid emittance growth after compression.

5.2 Simulation Results

5.2.1 Modulation and Compression

The particle distribution for this study is optimized with ASTRA [Flo00] to obtain a low emittance and a low energy spread for a bunch charge of 30 pC and an energy of 3 GeV to achieve a final peak current which is sufficient to drive the SASE FEL process. This working point is covered by the parameter range of the SwissFEL accelerator at the location of the ACHIP interaction chamber in the switchyard of the Athos beamline. At this location, the optimized distribution has a peak current of 300 A and a length of around 100 fs. The tracking of the modulated electron beam through the switchyard is done with ELEGANT [Bor00] including longitudinal space charge and coherent synchrotron radiation effects. The electromagnetic field distribution created in a laser excited structure is modeled with CST Studio [CST19]. We observe that the longitudinal and transverse component of the interaction follow the analytical solution derived in [NEB17]. The remaining transverse modulation amplitude is 500 times smaller than the transverse momentum spread for the case of the 3 GeV electron beam in Athos at SwissFEL. Detailed information about the field simulations with CST are given in section Methods - . We conclude, that the interaction of an ultra-relativistic electron bunch ($\gamma \approx 6000$) inside the channel of a double grating structure with the fields of a normally incident laser can be modeled as a homogeneous sinusoidal momentum modulation. The transverse kicks and the transverse dependence of the longitudinal kick vanish for a straight grating and ultra-relativistic electrons [NEB17]. The symmetry of the field can be even further enhance by illuminating the structure from both sides or by using a distributed Bragg mirror (DBR) behind the structure [NBE17; You+19]. The DBR consists of dielectric layers with well-defined thicknesses to reflect the laser and mimic double-sided illumination. The modulated electron beam is bunched in a subsequent magnetic chicane. Naturally, the achievable peak current after optimal compression depends on the slice energy spread and increases with the modulation strength, up to a certain limit. To illustrate the concept we use a modulation amplitude of 0.5 MeV, which leads to an optimal R_{56} around 2 mm. This modulation amplitude corresponds to an average acceleration gradient of 0.5 GV/m in a 1 mm long structure. Such gradients have recently been demonstrated in a DLA experiment for relativistic electrons at the Pegasus facility at UCLA in 0.5 mm to 1 mm long structures [Ces+18a]. The interaction length was limited to 21.5 μm due to the temporal overlap with the laser pulse since no pulse-front tilt for the laser was used in this experiment. The simulation results for the

DLA modulation, transport through the Athos switchyard of SwissFEL and optimal bunching are summarized in Figure 5.2. In the first row (sub-figures a-d) projections of the phase-space just after the DLA interaction are shown, whereas the second row (sub-figures e-h) depicts the bunched particle distribution after the magnetic chicane. After compression a strong increase of the slice energy spread ($\sigma_\gamma/\gamma = 1 \times 10^{-4}$) within the current spikes is observed, where γ is the relativistic mass factor. For SASE FELs the energy spread has to be much smaller than the FEL Pierce parameter ρ , see for instance [HK07]. In case of the Athos beamline at SwissFEL, ρ is in the order of 1×10^{-3} , this condition is fulfilled. Since the transverse modulation is negligible, we assume the slice emittance ($\epsilon_{n,x}$) to be conserved. Peak currents of up to 5 kA are achievable in this configuration, which corresponds to a current enhancement by a factor of 16. Similarly as for the conventional scheme, the spike heights inherit the Gaussian envelope from the original macro-bunch shape. The length of the individual spikes is expected to be around 140 as (FWHM). We observe 14 individual spikes with peak currents exceeding 2.5 kA spaced by 6.7 fs corresponding to the laser wavelength of 2 μm .

5.2.2 Comparison with Undulator Modulation

The conventional ESASE scheme uses an undulator magnet to resonantly transfer energy from a co-propagating optical laser to the electron beam to achieve a net-modulation of the electron beam [Zho05]. Here, we compare our proposed DLA modulation scheme to the conventional approach in terms of electron beam and laser requirements.

Emittance and Charge Limitations

Typical apertures of wiggler magnets are in the order of 10 mm. Typical electron beam sizes at the end of FEL accelerators are far below 1 mm. Thus, no special focusing elements for the electron beam are needed and the charge which can be transported through the modulating structure is not limited by the geometry of the wiggler. In comparison, the DLA modulation scheme requires the GeV electron beam to be focused into the micrometer scale channel of the dielectric structure. This can be achieved with strong quadrupole focusing in combination with low transverse emittance. The beam size is determined by the emittance and the Twiss parameter $\bar{\beta}$ at the interaction point by $\sigma = (\epsilon_n \bar{\beta} / \gamma)^{1/2}$. Since emittance scales with the charge for photo-injectors used at FELs, the charge which can be modulated in this scheme is limited. To estimate

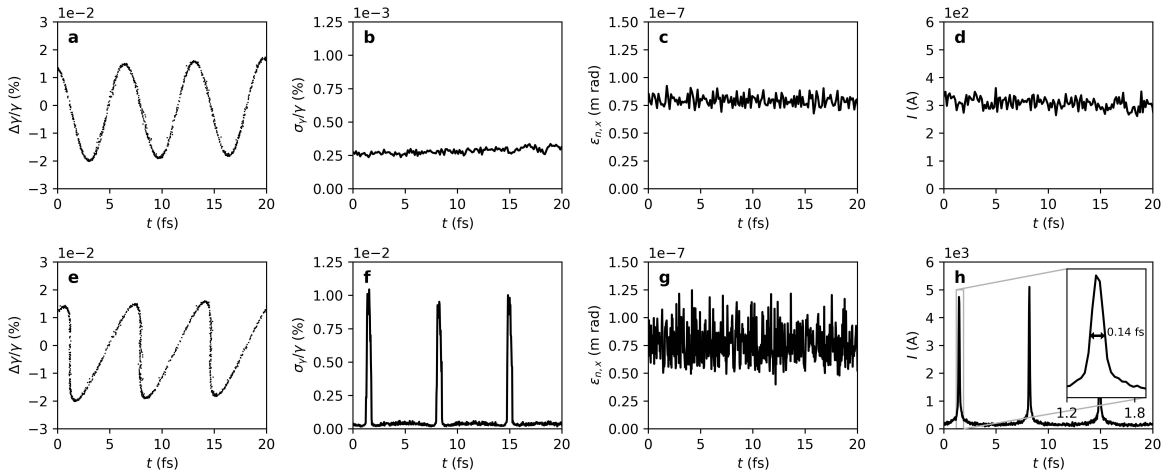


Figure 5.2: Simulated phase-space of the 3 GeV electron beam of SwissFEL at two locations: after the DLA interaction (first row, **a-d**) and after the propagation through the switchyard to the Athos beamline and optimal compression (second row, **e-h**). A strong increase in slice energy spread is observed, compare sub-figure **b** and **f**, whereas the slice emittance remains unchanged (sub-figure **c** and **g**). The noise in **g** appears larger than in **c**, as the bin width is reduced to resolve the short spikes. After optimal compression peak currents of up to 5 kA are predicted by this simulation (**h**).

the charge limit, we assume a grating aperture of $1.2 \mu\text{m}$, a beam energy of 3 GeV, and a $\bar{\beta}$ -function of 5 mm at the interaction point. These parameters can be achieved with the existing permanent magnet quadrupoles in the ACHIP chamber in the Athos branch at SwissFEL [Fer+18]. The in-vacuum quadrupole magnets are 10 cm long and provide a geometric strength (K -value) of 26 m^{-2} and 39 m^{-2} at a beam energy of 3 GeV [Pra+17]. For the parameters described above, the beam size and charge are plotted against emittance in Figure 5.3. The emittance of the electron beam in SwissFEL has been optimized for different charges according to the procedure explained in Methods. For a maximum beam size of $\sigma = 0.3 \mu\text{m}$, corresponding to a 4σ -aperture of $1.2 \mu\text{m}$, a normalized emittance smaller than 100 nm rad is required, which limits the charge to approximately 50 pC .

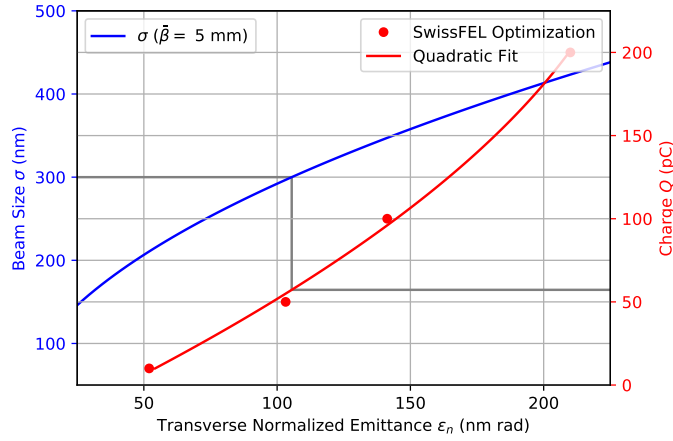


Figure 5.3: The transverse beam size (σ) for a fixed $\bar{\beta}$ -function (5 mm) and the maximum charge are plotted as a function of emittance. The emittance has been optimized for the SwissFEL injector at 4 different working points. We observe that a maximum charge of 50 pC can be focused to a beam size of 0.3 μm using the existing magnets in the ACHIP chamber installed in the Athos switchyard of SwissFEL.

Modulation Effectiveness

The total modulation amplitude $\Delta\gamma$ obtained from a laser with a peak power P_{pk} and a spot size $\sigma_{L,x}, \sigma_{L,z}$ (distance from the center at which the intensity drops to $e^{-1/2}$ of the maximum), in a dielectric grating of length L_S , is calculated by

$$\Delta\gamma = e_1 \frac{e}{m_e c^2} \left(\frac{P_{pk}}{c \epsilon_0 \pi \sigma_{L,x} \sigma_{L,z}} \right)^{\frac{1}{2}} \int_{-L_S/2}^{L_S/2} \exp\left(-\frac{z^2}{4\sigma_{L,z}^2}\right) dz. \quad (5.1)$$

Here, e_1 denotes the structure factor being the ratio of the effective acceleration gradient to the required incident electric field strength, which corresponds to the Fourier coefficient of the first spatial harmonic of the laser field inside the structure [NEB17]. This formula is derived by integration of the electric field along the structure, and from the relation between the electric field vector \vec{E} and the intensity I of an electromagnetic wave, $I = c\epsilon_0 \vec{E}^2/2$, where the vacuum permittivity is denoted by ϵ_0 . Considering that the modulation amplitude is proportional to the square root of the

laser power, it is useful to define the unit-less modulation effectiveness η as

$$\eta = \frac{c\epsilon_0}{e^2} \frac{(m_e c^2 \Delta\gamma)^2}{P_{pk}}. \quad (5.2)$$

This quantity describes the effectiveness of the modulating process and can be applied to any laser driven modulation scheme. It is a measure for the laser power which is required to achieve a certain modulation amplitude. The effectiveness depends on the laser focal spot size as described by equation 5.1 and 5.2. Due to the Gaussian integral involving the shape of the laser in z , the dependence is not monotonous and an optimum value can be found. To illustrate this, we plot the effectiveness against $\sigma_{L,z}$, see Figure 5.4. For a 1 mm long structure, the maximum effectiveness is achieved for $\sigma_{L,z} \approx 250 \mu\text{m}$. In practice, it can be favorable to use a larger laser spot size to reduce the peak electric field strength in the dielectric material and accept the reduced effectiveness. For the comparison, we assume a laser focal spot size of $\sigma_{L,x} = 4 \mu\text{m}$ by $\sigma_{L,z} = 500 \mu\text{m}$. The effectiveness is approximately 20 % lower as compared to the optimal case, see Figure 5.4. The Rayleigh length in x for a Gaussian laser beam is $z_{r,x} = 4\pi\sigma_{L,x}^2/\lambda_L$, which is around $100 \mu\text{m}$ in this case. The structure factor e_1 for a relativistic DLA made of fused silica is typically in the order of 1, which is what we use for the calculation, but can be higher (2-3) for a smaller gap size [Woo+16]. Higher e_1 however goes along with more resonant structures, prohibiting short pulse operation. Based on these parameters and the formula above we calculate an effectiveness of the DLA modulation technique of around 140. The ESASE scheme proposed for LCLS at Stanford uses a modulation at a wavelength of $2.2 \mu\text{m}$ with a modulation amplitude of 7 MeV. The required laser peak power is estimated to be 10.7 GW [Zho+04]. The corresponding effectiveness, as previously defined, for this setup is around 12. In comparison, the proposed DLA modulation scheme is around ten times more effective, in terms of required laser power for a fixed modulation amplitude. The requirements for the electron beam and the laser pulse for both schemes are summarized in table 5.1.

Tunability

Another important aspect for both schemes is the tunability of the modulation period. In both scenarios a change of the laser wavelength λ_L is required. In an experiment, this can be realized by a tunable optical parametric amplifier (OPA) in combination with reflective optics for the laser transport to avoid chromatic effects, for example in

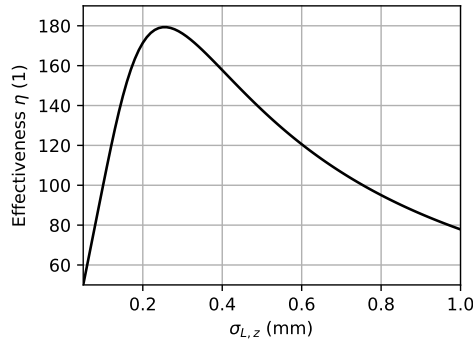


Figure 5.4: Dependency of the DLA modulation effectiveness on the laser focal spot size $\sigma_{L,z}$ for a 1 mm long structure.

lenses. Regarding the undulator modulation scheme, the wiggler parameter K_W needs to be modified such that $\lambda_L = \lambda_W(1 + K_W^2/2)/2\gamma^2$, where λ_W is the wiggler period [Zho05]. This is typically achieved by adjusting the gap between the magnetic arrays of the wiggler. In order to change the modulation period in the DLA scheme, the periodicity of the structure needs to be modified according to the resonance condition $\lambda_S = \lambda_L\beta n$. We propose to realize this with a chirped (diverging) grating, where the periodicity slowly changes along the open direction, see Figure 5.5. The resulting tilt of the grating will not degrade the transverse emittance since the transverse momentum modulation acquired in the first half of the structure is canceled in the second half as the tilt angle is inverted. In comparison to a series of different structures, the chirped grating approach would provide fast and continuous scanning capabilities by positioning the grating along its open direction (x). In principle, fused silica can be used for wavelengths ranging from 0.4 μm to 4 μm . In this window, the refractive index at room temperature varies between 1.4 and 1.6 and the absorption index is close to zero. To enhance the modulation effectiveness other grating parameters, such as the grating teeth width, could be optimized for the desired wavelength interval. For larger wavelengths, the absorption rises strongly and peaks at around 10 μm [KPJ07b]. The length of the individual current spikes can be tuned in both schemes by adjusting the modulation amplitude and the compression factor R_{56} of the magnetic chicane. For the DLA modulation scheme the modulation amplitude is limited by the damage threshold of the dielectric structure. Irreversible damage of fused silica DLAs has been observed for incident electric fields of around 9 GV/m [Ces+18a], which would limit

Parameter	Symbol	DLA	ESASE	Unit
Required transverse electron beam size	$\sigma_{e,y}$	0.3	-	μm
Structure Period (grating / wiggler magnet)	λ_S	2×10^{-6}	0.3	m
Number of periods	N_S	500	8	1
Structure length	L_S	1×10^{-3}	2.4	m
Laser wavelength	λ_L	2	2.2	μm
Laser spot size, x	$\sigma_{L,x}$	4	250	μm
Laser spot size, z	$\sigma_{L,z}$	500	250	μm
Modulation effectiveness	η	140	12	1

Table 5.1: Comparison of the requirements for the electron beam and the laser for DLA modulation and conventional undulator modulation for ESASE. The parameters for the ESASE scheme are taken from the proposal for LCLS [Zho+04].

the modulation amplitude to around 9 MeV for a 1 mm long structure. This boundary is more than one order of magnitude higher than the modulation amplitude we use for the bunching simulation presented above.

5.3 Discussion

We investigated a scheme which uses the fields in a dielectric micro-structure excited by a laser to modulate the ultra-relativistic electron beam of an FEL with the purpose of creating a pulse train for the ESASE scheme. Beam dynamics simulations using parameters of the SwissFEL accelerator predict the generation of 140 as (FWHM) electron spikes with peak currents up to 5 kA from a bunch with a total charge of 30 pC and an initial current of 0.3 kA. These beam parameters are suitable to drive the SASE process and create pulsed FEL radiation. Investigation of the properties of the radiation created in the Athos undulators at SwissFEL, through time-dependent FEL simulations, can be subject of a future study. Especially, the undulator tapering to increase the pulse energy while keeping the FEL pulses short and phase shifters between the undulator sections to create phase-locked pulses need to be optimized in detail.

The micrometer scale aperture of the dielectric structure implies strict limitations for beam focusing and transverse emittance. For the case of the Athos beamline at SwissFEL, the estimated charge limit is around 50 pC. Losses created by the tails of

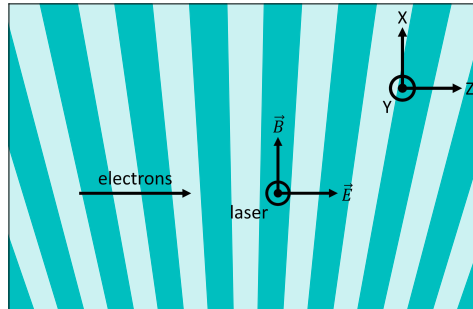


Figure 5.5: Conceptual drawing of the diverging grating structure. The periodicity can be scanned by moving the grating along x with respect to the electron beam. The dimensions and especially the slope of the changing periodicity need to be chosen, such that the periodicity changes not significantly within the beam size. As a consequence, the length of the chirped grating along the open direction (x) follows from the required tunability range. For a homogeneous interaction within the transverse beam shape we limit the periodicity change within $10\ \mu\text{m}$ to $0.01\lambda_S \equiv 20\ \text{nm}$. The resulting slope of the periodicity change along x equals 2×10^{-3} . For a tunability range of $1.5\ \mu\text{m}$ to $2.5\ \mu\text{m}$ a structure length along the open direction (x) is given by wavelength range / slope = $0.5\ \text{mm}$.

the beam limit the achievable repetition rate. The conventional undulator modulation scheme has no such limitations and is favourable in a high charge, emittance and repetition rate machine. Based on our estimation, dielectric laser modulation for ultra-relativistic electron beams is around a factor of ten more effective than undulator modulation, meaning that only a tenth of laser power is required to achieve the same modulation amplitude of the longitudinal phase-space. Since the laser system is one of the main cost drivers of the ESASE scheme, the proposed DLA modulation scheme presents a significant economic advantage. This aspect is particularly important for future, more compact and less expensive X-ray FEL facilities which will operate at lower charge and emittance than existing facilities. Both schemes allow continuous scanning of the modulation period, by changing the wavelength of the laser and properties of the modulating structure: in the undulator modulation scheme the wiggler parameter needs to be changed; in the DLA modulation scheme the periodicity of the grating needs to be adapted. We propose to use a diverging grating for continuous scanning capabilities.

5.4 Methods

5.4.1 Emittance Optimization for SwissFEL

SwissFEL can run at different bunch charges to accommodate the requests of the users. For each case, the emittance and the optics mismatch along the slices of the beam have been optimized at the injector to maximize the uniformity of the properties along the bunch, and therefore the lasing intensity. The main parameters included in the optimization are the first focusing at the exit of the radio-frequency gun, along the first accelerating structure, and the transverse size of the laser at the cathode. These parameters are determined starting from the layout corresponding to the 200 pC design case of SwissFEL and finely tuned using a simplex optimizer [BPR15]. In the simulations the assumed intrinsic emittance is 550 nm/mm, accordingly to what was measured at the SwissFEL injector test facility [Div+15; Pra+15]. Downstream of the injector the beam is compressed in two stages. We optimized the compression parameters to have an optimum balance between the intrinsic energy spread, the peak current and the residual chirp. We simulated 2×10^5 macro-particles for the tracking with ELEGANT [Bor00] of the 30 pC-distribution which is used in this study.

5.4.2 Electron Optics for High Current Beams

Operating the proposed DLA modulation scheme with a high current initial electron beam will induce strong wakefields inside the dielectric structure that may lead to heating and destruction of the device. The electron optics can be adapted to achieve a strongly asymmetric focus to reduce the current density inside the structure to reduce short-range wakefields. This can be achieved with a strong quadrupole doublet. We used the focusing strengths of the existing permanent magnets inside the ACHIP chamber at SwissFEL and optimized their position with ELEGANT [Bor00]. Due to the ultra-relativistic energy (3 GeV) transverse space charge effects at the focus can be neglected and the particle tracking code ELEGANT can be applied. The laminarity parameter, as defined for instance in [FMP14], must not exceed unity in order to neglect space charge forces. For the parameters of this study the laminarity parameter at the interaction point is indeed around 1×10^{-3} . The Twiss parameters ($\bar{\beta}_x$ and $\bar{\beta}_y$) along the beamline and the transverse beam profile at the interaction point for a normalized slice emittance at the core the beam of 80 nm rad are shown in Figure 5.6. The particle distribution for this simulation was optimized with ASTRA [Flo00] at a charge of 30 pC for the SwissFEL injector. The compression settings were optimized using ELEGANT.

With the optimized permanent magnet configuration a ratio $\bar{\beta}_x/\bar{\beta}_y$ of around 1600 can be achieved ($\bar{\beta}_x = 10$ m, $\bar{\beta}_y = 5$ mm). The aspect ratio of the electron beam is given by $(\bar{\beta}_x/\bar{\beta}_y)^{1/2} \approx 40$. A larger transverse electron beam size at the interaction point requires an even larger laser spot to maintain a homogeneous interaction. As a result, the laser power requirement would increase.

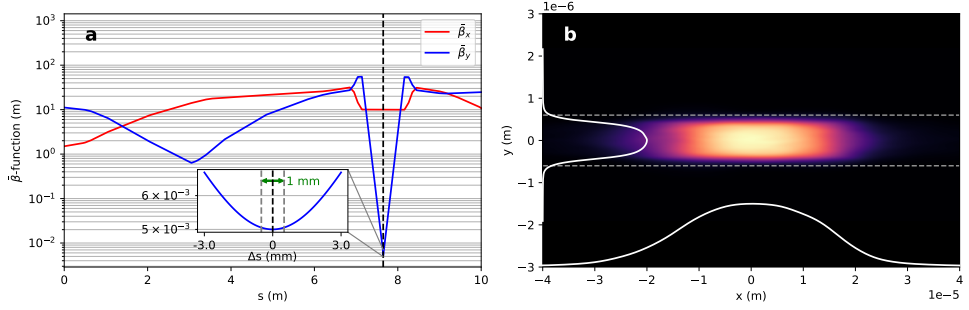


Figure 5.6: (a) Electron optics for asymmetric focusing with 2 strong permanent magnet quadrupoles. The Twiss parameters $\bar{\beta}_x$ and $\bar{\beta}_y$ are plotted around the interaction region. A ratio $\bar{\beta}_x/\bar{\beta}_y$ of around 1600 is achieved with a permanent magnet quadrupole doublet. The inset shows the evolution of $\bar{\beta}_y$ in the vicinity of the interaction point (black dashed line). We observe that the beam size does not change significantly within a propagation distance of 1 mm (green arrow). (b) Simulated electron beam profile at the interaction point. The two dashed lines indicate the gap of the dielectric double grating ($1.2 \mu\text{m}$).

5.4.3 Structure Optimization and Transverse Effects

The geometry of the dielectric double grating is optimized to achieve a structure factor of about 1. We used CST Microwave Studio [CST19] to calculate the electromagnetic fields of a single grating period in the frequency domain. The incident laser field is modeled as a plane wave coupled into the dielectric structure. The Fourier coefficient of the first spatial harmonic is given by [NEB17]

$$\underline{e}_1(y) = \frac{1}{\lambda_S E_0} \int_{-\lambda_S/2}^{\lambda_S/2} \underline{E}_z(y, z) \exp\left(i \frac{2\pi}{\lambda_S} z\right) dz \quad (5.3)$$

with the longitudinal electric field $\underline{E}_z(y, z)$ inside the channel and the amplitude E_0 of the incident laser field. The absolute value of the complex Fourier coefficient

as the structure factor describes the ratio of the acceleration gradient to the incident laser field. To achieve the desired structure factor in the center of the channel, we optimized the teeth and also the base thickness for a given aperture. The resulting parameters are shown in Figure 5.7. Since the transverse dependence of the Fourier coefficient is analytically given as $\underline{e}_1(y) = \underline{e}_1(y=0) \cosh(2\pi y/(\lambda_L \beta \gamma))$ [NEB17], the modulation amplitude is almost independent of the transverse position in the gap. This is confirmed by numerically evaluating the structure factor along the gap, see Figure 5.7. The transverse fields can be analytically obtained using the Panofsky-Wenzel theorem. For a straight grating, the transverse kick becomes $\underline{f}_1(y) = \lambda_L/(2\pi) \partial \underline{e}_1/\partial y = \underline{e}_1(y=0) \sinh(2\pi y/(\lambda_L \beta \gamma))/\gamma$ [NEB17] and therefore vanishes for ultra-relativistic electrons. Numerically the transverse kick can be calculated by integrating the transverse electric and magnetic fields inside the channel as

$$\underline{f}_1(y) = \frac{1}{\lambda_S E_0} \int_{-\lambda_S/2}^{\lambda_S/2} \left(\underline{E}_y(y, z) + \beta c \underline{B}_x(y, z) \right) \exp\left(i \frac{2\pi}{\lambda_S} z\right) dz. \quad (5.4)$$

The evaluation of this integral along the gap using the fields simulated by CST Microwave Studio confirmed the analytical description, i.e. that the transverse effect vanishes, see Figure 5.7. Note that the numerical noise arises especially from the interpolation of the magnetic field, which is not allocated at the same mesh entity as the electric field and thus needs to be interpolated. This is the reason why the numerical transverse kicks, which are close to zero, do not fulfill the Panofsky-Wenzel theorem. To estimate the effect of the remaining transverse component we compare \underline{f}_1 to the transverse momentum spread of the electron beam at the interaction point. Over the entire gap the transverse amplitude is more than a factor of 1000 smaller than the longitudinal modulation component. For the case of the longitudinal modulation amplitude used in this study (0.5 MeV) the transverse modulation is expected to be smaller than 0.5 keV. The rms transverse momentum spread at the interaction point is calculated to be around 260 keV, which is a factor of 500 larger than the transverse modulation effect. The large transverse momentum spread is a result of the strong focusing. Hence, the degradation of the slice emittance by transverse forces in the structure can be neglected for an ultra-relativistic electron beam.

5.4.4 Jitter and Stability Considerations

Good stability of beam position and size is required for the DLA modulation scheme, due to its micro-meter sized aperture. The electromagnetic field simulation for the

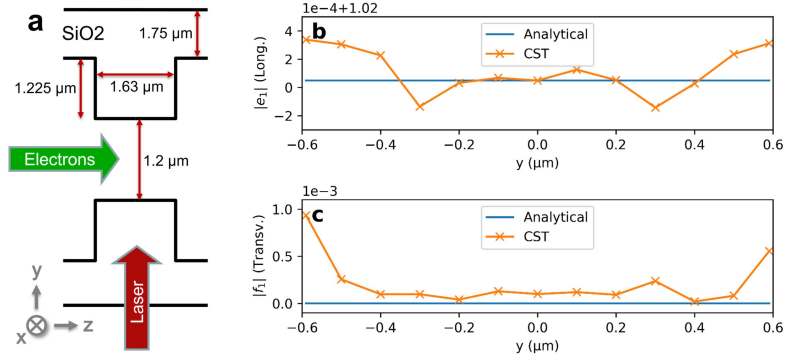


Figure 5.7: (a) Parameters of the optimized double grating. (b) Longitudinal structure factor e_1 plotted along the $1.2\ \mu\text{m}$ wide gap of the structure. The numerical noise of the constant structure factor of 1.02 is in the order of 1×10^{-4} . (c) Transverse structure factor f_1 . Transverse forces (including numerical noise) across the gap are 3 orders of magnitude smaller than longitudinal forces.

proposed structure shows good homogeneity of the modulation strength ($< 0.05\%$) and negligible transverse forces across the channel gap. Therefore, beam position and size jitter will not affect the modulation strength but only the number of particles hitting the boundary of the dielectric grating. In the following, we estimate the fraction of particles being transmitted through the structure geometry defined above. An upper limit for the position jitter of the electron beam in the accelerator of SwissFEL is 10% of the beam size. The beam size measured along the machine typically shows jitter in the order of 3% . In the proposed strong focusing setup, energy jitter adds significantly to the beam size due to chromatic effects of the permanent magnet quadrupoles. Simulations using ELEGANT [Bor00] show an increase of the spot size by 1% for a typical energy error of 0.1% . For the calculation of the transmitted fraction we consider a maximum position offset of $\Delta y = 30\ \text{nm}$ and a beam size scaled by the factor $\kappa_y = 1.05$. The beam profile distribution is shown in Figure 5.8 for three different combinations: (a) $\Delta y = 0\ \text{nm}$, $\kappa_y = 1.00$, (b) $\Delta y = 30\ \text{nm}$, $\kappa_y = 1.00$, (c) $\Delta y = 30\ \text{nm}$, $\kappa_y = 1.05$. In the worst case scenario (c) a fraction of 2.3% of the electrons will scatter in the dielectric material of the structure. Towards high repetition rates above $100\ \text{Hz}$, radiation protection of the machine may become an issue. In this case, it might be required to increase the structure gap and sacrifice efficiency. The small loss of scattered particles in the tail of the electron beam do not reduce the stability of

the FEL output power since the core of the beam is dominantly driving the SASE FEL process.

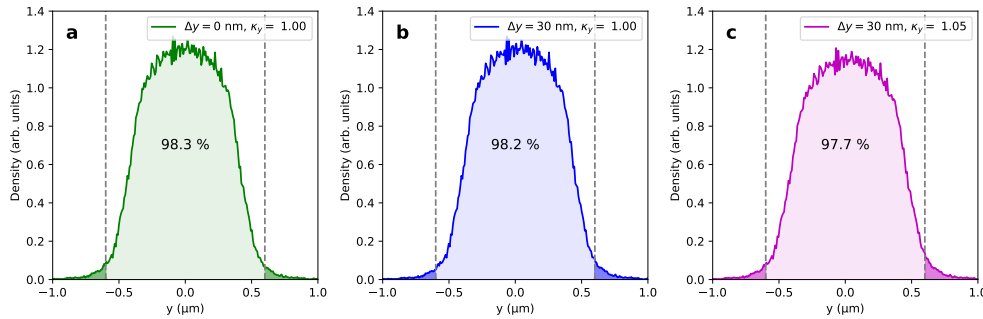


Figure 5.8: Transverse beam profiles for different combinations of position offset (Δy) and beam size factor (κ_y): (a) ideal case $\Delta y = 0$ nm, $\kappa_y = 1.00$, (b) $\Delta y = 30$ nm, $\kappa_y = 1.00$, (c) worst case $\Delta y = 30$ nm, $\kappa_y = 1.05$. The aperture of the dielectric grating structure is shown in gray, dashed.

Author Contributions Statement

B.H., U.N., E.P. and R.I. designed the concept. S.B. simulated the generation of suitable electron bunches in the SwissFEL accelerator. E.P. and B.H. implemented the beam dynamics simulation for the transport of the beam along Athos. T.E. modeled the electromagnetic fields in the structure and optimized the structure geometry. U.N. and B.H. developed the notion of modulation effectiveness. All authors contributed to the manuscript.

Competing Interests

The authors declare no competing interests.

Data Availability

The simulation data that support the findings of this study are available from the corresponding author upon reasonable request.

6

Optical Bunching Diagnostics

Diagnostics for Electron Pulse Trains at SwissFEL Obtained by Energy Modulation in a Laser-Driven Dielectric Structure

Authors: Benedikt Hermann^{1,2}, Simona Bettoni¹, Thilo Egenolf³, Thomas Feuerer², Franziska Frei¹, Uwe Niedermayer³, Eduard Prat¹ and Rasmus Ischebeck¹

¹Paul Scherrer Institut, 5232 Villigen PSI, Switzerland

²Institute of Applied Physics, University of Bern, 3012 Bern, Switzerland

³Institute for Accelerator Science and Electromagnetic Fields (TEMF), TU Darmstadt, 64289 Darmstadt, Germany

Published: September 18, 2020. Journal of Physics: Conference Series, Volume 1596, 4th European Advanced Accelerator Concepts Workshop 15-20 September 2019, Isola d'Elba, Italy, Article number: 012046.

DOI: <https://doi.org/10.1088/1742-6596/1596/1/012046>

Abstract

Electron pulse trains with sub-femtosecond spike length offer novel possibilities to ultra-fast pump-probe experiments in free-electron lasers. The pulse train can be generated by an energy modulation which is converted to temporal bunching in a magnetic chicane. The source of the energy modulation is typically a resonant interaction with a co-propagating laser in a wiggler magnet. Alternatively, the modulation can be obtained by a dielectric laser accelerator (DLA). The implementation of the DLA modulation scheme at SwissFEL would be enabled by using the experimental chamber installed in the framework of the Accelerator-on-a-Chip International Program (ACHIP) and a magnetic chicane placed afterwards. In this contribution, we will focus on electron beam diagnostics for the DLA-modulated and compressed electron bunch train. Our simulation results predict that measuring the energy spread of the modulated beam and coherent diffraction radiation emitted from a foil with a hole provides a precise tool to characterize and optimize the laser-electron modulation. An absolute measurement of the longitudinal phase-space with a temporal rms-resolution of 350 as is possible with the planned X-band transverse deflecting cavity in Athos.

6.1 Introduction

Free-electron lasers (FELs) make use of a highly compressed relativistic electron beam to generate electromagnetic radiation in a magnetic undulator. They are the brightest sources of radiation from the VUV [Ack+07; All+15] to the X-ray regime [Alt+06; Emm+10; Ish+12; Kan+17; Mil+17]. A technique proposed to generate an individual or a train of sub-femtosecond X-ray pulses with well-defined separation is the energy modulation of the electron bunch with a laser in the magnetic field of a resonant undulator (wiggler). The energy modulation is converted into a longitudinal density modulation with a magnetic chicane. This enhanced SASE (ESASE) method was proposed by Zholents [Zho05], and has been implemented at LCLS and is planned at other facilities such as SwissFEL. As an alternative approach, we investigated and compared the modulation of the electron beam in a dielectric laser accelerator (DLA) to the conventional undulator modulation scheme. In a DLA, electrons interact with the near-field excited by an external laser in the vicinity of a dielectric micro-structure. The phase velocity of the evanescent wave depends on the periodicity of the structure and the wavelength of the laser. Resonant acceleration of electrons requires the phase velocity to match to the particles velocity (phase-synchronicity) [Eng+14]. Particles resonantly gain or lose energy depending on their phase. If the initial electron beam is longer than the wavelength of the driving laser, the longitudinal phase space will be modulated. In a beam dynamics simulation study, we estimate that a similar modulation strength can be achieved by around 10 times less laser power using the DLA scheme due to the reduced interaction volume. Further details on the DLA modulation concept for the generation of pulse trains in FELs can be found in [Her+19]. The beamline required for the proposed scheme is sketched in Figure 6.1. The intrinsic synchronization of the FEL pulses to an external laser makes these schemes very suitable for ultra-fast pump-probe experiments. The CHIC scheme in the soft X-ray beamline in SwissFEL (Athos) makes use of magnetic chicanes between the undulator segments to delay the electron beam with respect to the X-rays [Abe+19]. This setup would allow the generation of a phase locked pulse train [TM08]. The vacuum chamber for the DLA interaction, which is equipped with a hexapod for sample positioning and six strong in-vacuum permanent magnet quadrupoles to match the electron beam into the dielectric structure is installed in the switchyard to Athos and is currently being commissioned. It is also planned to demonstrate GV/m gradients in DLA structures with a length of 1 mm at a laser wavelength of 2 μm [Fer+18; Pra+17].

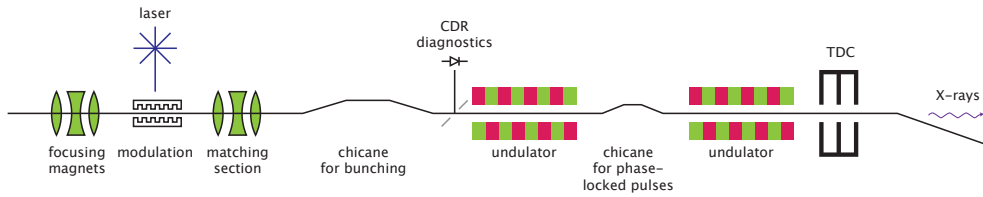


Figure 6.1: Sketch of the DLA modulation scheme. After modulation of the longitudinal phase-space, the ultra-relativistic electron beam is bunched in a magnetic chicane. The resulting pulse train creates uniformly spaced spikes of X-ray radiation in the undulator section. A coherent diffraction radiation (CDR) monitor after the bunching chicane can be used as a passive temporal diagnostic for the electron bunch. A direct measurement of the longitudinal phase-space is possible with a transverse deflecting cavity (TDC) at the end of the beamline. The illustration is adapted from [Her+19]

6.2 Modulation and Bunching Diagnostics

We investigate methods to diagnose the energy modulation and temporal properties of the bunched electron beam after passing through the dielectric structure and magnetic chicane for compression. We outline a setup procedure to optimize spatial and temporal overlap between electrons and laser, as well as a method to precisely tune the modulation amplitude and compression factor to achieve the maximum peak current and shortest length of the individual spikes. Our calculations predict that an absolute measurement of the longitudinal phase-space with an rms-resolution of 350 as can be achieved with the planned X-band TDC at the end of the Athos beamline. The particle distribution used for this study is optimized with ASTRA [Flo00] and ELEGANT [Bor00] for the case of SwissFEL. The beam energy in the Athos beamline is 3 GeV. The normalized emittance (80 nm rad) at the core of the beam has been minimized for a charge of 30 pC.

6.3 Energy Spectrometer

A measurement of the increase in projected energy spread of the electron beam due to the laser interaction is needed to initially optimize spatial and temporal overlap between the laser pulse and the electrons in the dielectric structure. Since the total initial electron bunch length is longer than the wavelength of the laser (2 μm) the projected energy spread increases with the modulation amplitude. For the case of

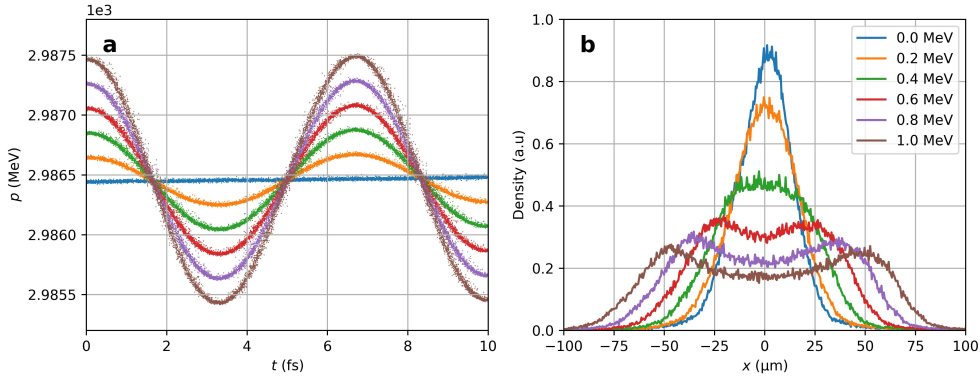


Figure 6.2: (a) 10-fs window of the modulated (uncompressed) longitudinal phase-space. (b) ELEGANT simulation of the horizontal electron distribution for different modulation strengths as seen on the dispersive screen in the Athos switchyard at SwissFEL. The characteristic double-horn structure which develops with increasing modulation strengths is observed.

SwissFEL a suitable profile monitor is available in a dispersive section of the Athos switchyard. We perform tracking simulations with ELEGANT[Bor00] for different modulation strengths and investigate the particle distribution at the location of the dispersive screen. The energy-modulated phase-space and the horizontal (x) projection are shown in Figure 6.2. The growth of the energy spread for increasing modulation strengths is clearly observable on the dispersive screen. A characteristic result of the projection of a sinusoidal modulation is the double-horn structure which develops for amplitudes exceeding the projected energy spread. The measurement of the energy spread can be used to infer the modulation amplitude, but no information about temporal properties of the electron beam is obtained.

6.4 Coherent Diffraction Radiation

A simple and non-invasive characterisation of the temporal bunch shape of the electron beam is the diagnosis of coherent diffraction radiation (CDR) emitted when the beam passes through a hole in a metallic foil. This concept is elaborated in [Cas+01; Cas96; Chi06; Ger+11]. The spectral intensity of the CDR of N particles is related to the longitudinal bunch shape (longitudinal form factor), as described for instance

in [Cas+05; Fre+13; LHS94; LS94], by

$$\frac{d^2P}{d\omega d\Omega} = \frac{d^2P_0}{d\omega d\Omega} (N + N(N - 1)|F(\omega)|^2), \quad (6.1)$$

where $d^2P_0/d\omega d\Omega$ is the single electron spectrum of the considered radiation process and F is the longitudinal form factor. This concept is also valid for other radiation processes which preserve the bunch shape, such as coherent transition or coherent synchrotron radiation. The longitudinal form factor is given by the Fourier transform of the longitudinal charge distribution, neglecting the contribution of the transverse profile. The finite transverse extent of the beam will reduce the emitted intensity as investigated in [Gri+08]. This reduction can be minimized by focusing the electron beam into the radiator. In addition, we will concentrate the analysis on the CDR spectrum at wavelengths 15 to 40 times larger than the length of the individual spikes. For longer wavelength, compared to the bunch length, the effect of the transverse beam size is further suppressed. To estimate the radiation dependence on the modulation amplitude (for fixed compression, $R_{56} = 2$ mm), we calculate the current profile for a series of modulation amplitudes and simulate the emitted spectrum according to the derivation in [Cas+05].

Figure 6.3 contains the details of this scan. The longitudinal phase-space distribution is shown in sub-figure 6.3a for three characteristic cases (0.3 MeV: under-compressed, 0.5 MeV: fully compressed and 0.7 MeV: over-compressed). The corresponding current is given in the sub-figure below (6.3c). The simulated CDR spectrum emitted from a metallic foil with a hole (diameter: 1 mm) is plotted in sub-figure 6.3b. We neglect here radiation generated at other edges present in the beamline, for instance at diagnostic chambers. The mechanical design for a real machine should consider guiding and shielding of the electromagnetic radiation emitted at all edges and interfaces. The integrated spectrum ($2 \mu\text{m} \pm 1\%$) for the entire amplitude scan is shown in sub-figure 6.3d. In addition, we perform the same simulation scan for the case of a fixed modulation amplitude (0.5 MeV) and a variable compression factor R_{56} . The peak current and integrated CDR signal for both scans (amplitude and compression factor) are summarized in Figure 6.4. We observe that the intensity around the modulation wavelength ($2 \mu\text{m}$) is not monotonically correlated to the peak current of the bunch train. In the case of over-compression, the CDR signal keeps increasing, although the peak current is decreasing. This is a result of the increased $2 \mu\text{m}$ periodicity content in the Fourier transform of the current, while the peak current is already reduced.

To obtain more information about the length of the individual spikes, higher-order

peaks of the CDR spectrum need to be taken into account as well. Figure 6.4 shows the CDR intensity at the central modulation wavelength (1st harmonic: $2\ \mu\text{m}$), at the 2nd and 3rd harmonic for both parameter scans. The spectrum at shorter wavelengths is indeed more sensitive to the length of the individual current spikes. This can be seen in the drop of the signal for over-compression for the higher harmonics. A key feature of the CDR simulation is the intersection of the normalized signals at the point of optimal compression. This reflects the fact that the current distribution is affected the most at the point where the linear part of the sinusoidal modulation is vertical in phase-space (close to optimal compression). Measuring the CDR spectrum during a scan of the modulation amplitude and the compression factor (R_{56}) and analysing their normalized intensities around fixed frequencies provides a simple optimization tool for the compression state of the bunch train.

Experimentally, this measurement can be realized by inserting a holed foil after the bunch compressor and transporting the radiation to a spectrometer or a series of wavelength-dependent beam splitters and photo-diodes, sensitive in the relevant spectral range (visible to near-infrared). A careful characterization of the detection setup is required and should include a measurement of the wavelength-dependent sensitivity as well as a test of the signal linearity with respect to the incident intensity. Therewith, single-shot acquisition permits to compare intensity ratios as depicted in Figure 6.4. To further increase the precision, beam-synchronous data acquisition would allow to take into account dependences on other beam parameters (e.g. charge and orbit fluctuations).

6.5 Transverse Deflecting Cavity

A direct measurement of the beam current can be achieved by correlating the longitudinal and transverse coordinates of the electron beam with the fields of a transverse deflecting cavity (TDC). The longitudinal phase space can be retrieved by combining the TDC with a dispersive screen. A TDC with variable polarisation operating at X-band frequency is planned to be installed in the Athos beamline of SwissFEL [Cra+18]. Since the TDC will be in the post-undulator section, the measurement of the energy loss and energy-spread increase of the electron beam can be used to reconstruct the temporal profile of the photon pulses [Beh+14]. Sub-fs temporal resolution is expected by the post-undulator X-band TDC at Athos [Cra+18]. For a normalized emittance of $80\ \text{nm rad}$ and a maximum RF voltage of $60\ \text{MV}$, our calculations predict an rms-resolution of $350\ \text{as}$. During the TDC streaking, the slice energy spread is expected to

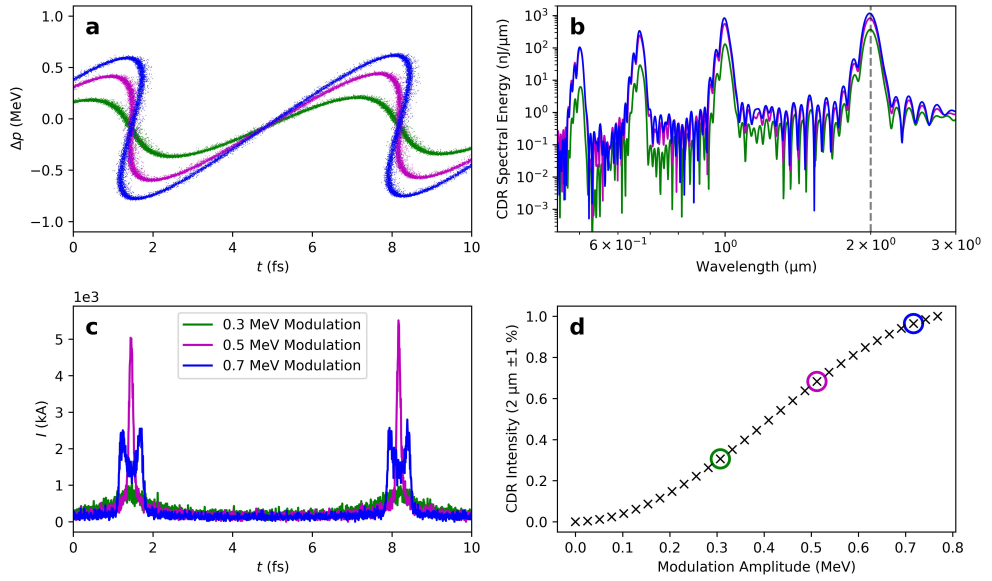


Figure 6.3: Phase-space (a) and beam current (c) of the modulated and compressed electron beam. The CDR emission spectrum comprises peaks at $2 \mu\text{m}$ (modulation wavelength) and at higher harmonics (b). The dependence of the integrated intensity on the modulation amplitude for a fixed compression factor within a range of $\pm 1\%$ around $2 \mu\text{m}$ is shown in sub-figure (d).

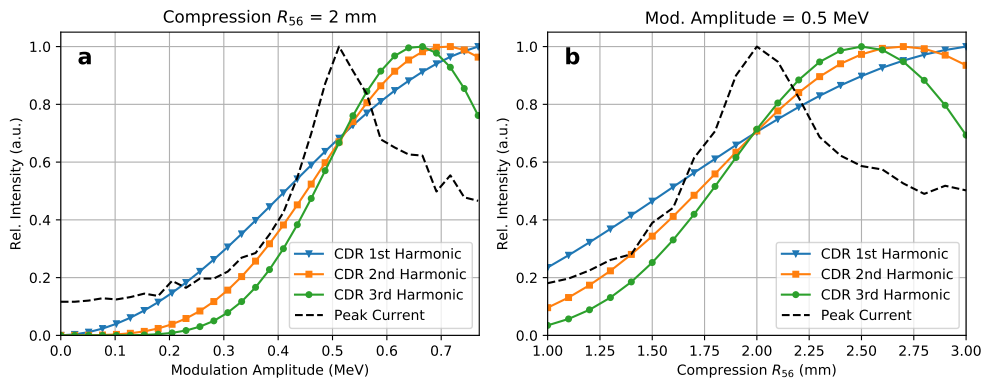


Figure 6.4: Normalized CDR signal at $2\ \mu\text{m}$ and higher harmonics for two parameter scans: Left: modulation amplitude, Right: compression factor R_{56} . The CDR spectrum is integrated within a $\pm 1\%$ interval. The peak current of the bunch train (after compression) is shown in black, dashed. The parameters for optimal compression coincide with the intersection of the CDR curves. At this point the slope of the CDR signals at all harmonics is maximal. Scanning the compression and modulation parameters while acquiring the intensity of the CDR spectrum provides a simple tool to maximize the current within the compressed bunch train.

increase by about 0.4 MeV. This imposes a limit to the measurement of small energy modulations after the TDC.

6.6 Conclusion

We present simulations of diagnostic tools to characterize and optimize the modulation and compression for a bunch train obtained from dielectric laser modulation at SwissFEL. The energy modulation (without temporal information) can be observed and maximized in a dispersive screen in the Athos switchyard. The compressed bunch train can be characterized via CDR generated for instance at a hole in a metallic foil located after the magnetic chicane. Our simulations show that the peak current of the bunch train can be precisely optimized by measuring the CDR intensity at the modulation wavelength and a few higher harmonics while scanning the compression and modulation parameters. These diagnostic tools are investigated for electron bunch properties optimized for the DLA modulation scheme in the ACHIP chamber, but are applicable as well to similar electron pulse trains obtained by conventional undulator modulation for the ESASE scheme. These spectral diagnostics can be complemented by a TDC installed after the undulator, which can provide absolute temporal information of the electron and photons with an expected resolution of about 350 as.

Within this study, I investigated new technologies for future accelerators in collaboration with colleagues from ACHIP and PSI. Concepts were tested with the ACHIP chamber at SwissFEL. This experimental vacuum chamber has been installed in the switchyard to the Athos branch and is now fully operational. In-vacuum permanent magnet quadrupoles for beam focusing and a precision hexapod for sample exchange and alignment are commissioned. The strengths of the quadrupoles have been verified with a beam-based measurement and confirmed the design parameters within an uncertainty of 1 %.

We developed a tool for two-dimensional beam profile measurements with sub-micrometer resolution: Nine nano-fabricated metallic wires are scanned at different angles across the beam while a beam loss monitor captures the amount of scattered particles. Applying tomography, the transverse beam distribution is reconstructed. Repeating the scans at different positions along the waist allows us to assess the four-dimensional transverse phase space. This tool could be used at other advanced accelerator research facilities which require diagnostics of micrometer-sized beams. Collaborators from ACHIP at DESY have received a nano-fabricated wire scanner from PSI and plan to characterize the electron beam at the ARES linac with it. A modified version of the multi-dimensional wire scanner could complement existing wire scanners, which would improve beam profile and emittance diagnostics at SwissFEL.

A tunable dielectric double grating with a variable gap ($10\ \mu\text{m}$ to $100\ \mu\text{m}$) and a periodicity of $50\ \mu\text{m}$ for wakefield studies has been designed and was fabricated by FEMTOprint. We were able to transmit the entire electron beam with a charge of $10\ \text{pC}$ through the narrow channel without significant losses. The effect of the longitudinal wakefield was observed on a spectrometer and tunability was demonstrated. Transverse wakefields perpendicular to the dispersive direction were studied experimentally as well. The strong dependence of the transverse streaking on beam tilts could be used for a precise tilt correction scheme.

The simulations of the wakefield interaction with CST do not reproduce the experimental results well. The calculated shift of the main peak of the spectrum is around a factor of three larger than seen in the experiment. A variety of parameter studies were

carried out, but did not resolve the discrepancy. The wakefield studies would greatly benefit from a direct measurement of the LPS after the ACHIP chamber, as it would allow us to observe the wakefield time-dependently. Nevertheless, the demonstrated loss-less transmission and tunable wakefield interaction make this a device a potential candidate for passive beam shaping at SwissFEL.

With a theoretical study, we explored the use of a DLA to modulate the LPS of the electron beam at infrared wavelengths for FELs. By a magnetic chicane, the energy modulation can be converted to a pulse train which can be used for the generation of an X-ray pulse train in the undulators. We showed that the laser-to-modulation efficiency for the DLA scheme is around an order of magnitude better than for the conventional eSASE scheme using a magnetic wiggler to resonantly extract energy from a co-propagating laser. Hence, DLAs could provide a compact and cost-efficient alternative to the conventional eSASE scheme at FELs.

Bibliography

- [Abe+19] R. Abela, A. Alarcon, J. Alex, C. Arrell, V. Arsov, S. Bettoni, M. Bopp, C. Bostedt, H.-H. Braun, M. Calvi, et al. **The SwissFEL soft X-ray free-electron laser beamline: Athos**. *Journal of Synchrotron Radiation* 26:4 (2019) (see pages 19, 61, 79).
- [Ack+07] W. a. Ackermann, G. Asova, V. Ayzvazyan, A. Azima, N. Baboi, J. Bähr, V. Balandin, B. Beutner, A. Brandt, A. Bolzmann, et al. **Operation of a free-electron laser from the extreme ultraviolet to the water window**. *Nature photonics* 1:6 (2007), 336 (see pages 60, 79).
- [ACS] ACST. ACST GmbH, Hanau, Germany. URL: <https://acst.de/> (see page 13).
- [Akr+08] R. Akre, D. Dowell, P. Emma, J. Frisch, S. Gilevich, G. Hays, P. Hering, R. Iverson, C. Limborg-Deprey, H. Loos, et al. **Commissioning the linac coherent light source injector**. *Physical Review Special Topics-Accelerators and Beams* 11:3 (2008), 030703 (see page 32).
- [All+15] E. Allaria, L. Badano, S. Bassanese, F. Capotondi, D. Castronovo, P. Cinquegrana, M. Danailov, G. D’Auria, A. Demidovich, R. De Monte, et al. **The FERMI free-electron lasers**. *Journal of synchrotron radiation* 22:3 (2015), 485–491 (see pages 60, 79).
- [Alt+06] M. Altarelli, R. Brinkmann, M. Chergui, W. Decking, B. Dobson, S. Düsterer, G. Grübel, W. Graeff, H. Graafsma, J. Hajdu, et al. **The European x-ray free-electron laser**. *Technical design report, DESY 97* (2006), 1–26 (see pages 60, 79).
- [Bal+95] V. Balakin, V. Alexandrov, A. Mikhailichenko, K. Flöttmann, F. Peters, G.-A. Voss, V. Bharadwaj, M. Halling, J. Holt, J. Buon, et al. **Focusing of submicron beams for TeV-scale e^+e^- linear colliders**. *Physical Review Letters* 74:13 (1995), 2479 (see page 32).
- [Ban+09] K. L. F. Bane, F.-J. Decker, Y. Ding, D. Dowell, P. Emma, J. Frisch, Z. Huang, R. Iverson, C. Limborg-Deprey, H. Loos, H.-D. Nuhn, D. Ratner, G. Stupakov, J. Turner, J. Welch, and J. Wu. **Measurements and modeling of coherent synchrotron radiation and its impact on the Linac Coherent Light Source electron beam**. *Phys. Rev. ST Accel. Beams* 12 (3 Mar. 2009), 030704. doi: 10.1103/PhysRevSTAB.12.030704. URL: <https://link.aps.org/doi/10.1103/PhysRevSTAB.12.030704> (see pages 48, 55).

- [Beh+14] C. Behrens, F.-J. Decker, Y. Ding, V. Dolgashev, J. Frisch, Z. Huang, P. Krejcik, H. Loos, A. Lutman, T. Maxwell, et al. **Few-femtosecond time-resolved measurements of X-ray free-electron lasers**. *Nature communications* 5 (2014), 3762 (see page 83).
- [Bla+19] D. S. Black, U. Niedermayer, Y. Miao, Z. Zhao, O. Solgaard, R. L. Byer, and K. J. Leedle. **Net Acceleration and Direct Measurement of Attosecond Electron Pulses in a Silicon Dielectric Laser Accelerator**. *Phys. Rev. Lett.* 123 (26 Dec. 2019), 264802. DOI: [10.1103/PhysRevLett.123.264802](https://doi.org/10.1103/PhysRevLett.123.264802). URL: <https://link.aps.org/doi/10.1103/PhysRevLett.123.264802> (see page 1).
- [Bol+15] B. Bolzon, A. Aryshev, T. Aumeyr, S. Boogert, P. Karataev, K. Kruchinin, T. Lefevre, S. Mazzoni, L. Nevay, M. Shevelev, et al. **Very high resolution optical transition radiation imaging system: Comparison between simulation and experiment**. *Physical Review Special Topics-Accelerators and Beams* 18:8 (2015), 082803 (see pages 17, 32).
- [Bor+18] S. Borrelli, G. L. Orlandi, M. Bednarzik, C. David, E. Ferrari, V. A. Guzenko, C. Ozkan Loch, E. Prat, and R. Ischebeck. **Generation and measurement of sub-micrometer relativistic electron beams**. *Communications Physics* 1:52 (2018), 1–8. DOI: <https://doi.org/10.1038/s42005-018-0048-x>. URL: <https://doi.org/10.1038/s42005-018-0048-x> (see pages 12, 17).
- [Bor00] M. Borland. **Elegant: A flexible SDDS-compliant code for accelerator simulation**. Tech. rep. Argonne National Lab., IL (US), 2000 (see pages 9, 10, 46–48, 63, 71, 74, 80, 81).
- [Bor01] M. Borland. **Simple method for particle tracking with coherent synchrotron radiation**. *Phys. Rev. ST Accel. Beams* 4 (7 July 2001), 070701. DOI: [10.1103/PhysRevSTAB.4.070701](https://doi.org/10.1103/PhysRevSTAB.4.070701). URL: <https://link.aps.org/doi/10.1103/PhysRevSTAB.4.070701> (see page 48).
- [BPR15] S. Bettoni, M. Pedrozzi, and S. Reiche. **Low emittance injector design for free electron lasers**. *Physical Review Special Topics-Accelerators and Beams* 18:12 (2015), 123403 (see page 71).
- [Bra+03] H. H. Braun, S. Döbert, I. Wilson, and W. Wuensch. **Frequency and temperature dependence of electrical breakdown at 21, 30, and 39 GHz**. *Physical Review Letters* 90:22 (2003), 224801 (see pages 1, 38).
- [Cas+01] M. Castellano, V. Verzilov, L. Catani, A. Cianchi, G. Orlandi, and M. Geitz. **Measurements of coherent diffraction radiation and its application for bunch length diagnostics in particle accelerators**. *Physical Review E* 63:5 (2001), 056501 (see page 81).
- [Cas+05] S. Casalbuoni, B. Schmidt, P. Schmüser, and B. Steffen. **Far-infrared transition and diffraction radiation**. *Tesla Report 2005-15*: 2005 (2005) (see page 82).

- [Cas96] M. Castellano. **Diffraction Radiation as a non-intercepting diagnostics for TTF: the bunch length measurement**. *Tesla Report 1996-08*: 1996 (1996) (see page 81).
- [Ces+18a] D. Cesar, S. Custodio, J. Maxson, P. Musumeci, X. Shen, E. Threlkeld, R. England, A. Hanuka, I. Makasyuk, E. Peralta, et al. **High-field nonlinear optical response and phase control in a dielectric laser accelerator**. *Communications Physics* 1:1 (2018), 46 (see pages 2, 3, 38, 41, 63, 68).
- [Ces+18b] D. Cesar, J. Maxson, P. Musumeci, X. Shen, R. England, and K. Wootton. **Optical design for increased interaction length in a high gradient dielectric laser accelerator**. *Nuclear Instruments and Methods in Physics Research Section A: Accelerators, Spectrometers, Detectors and Associated Equipment* 909 (2018), 252–256 (see page 61).
- [Chi06] E. Chiadroni. **Bunch Length Characterization at the TTF VUV-FEL**. *Tesla-FEL 2006-09*: 2006 (2006) (see page 81).
- [Cof+19] R. N. Coffee, J. P. Cryan, J. Duris, W. Helml, S. Li, and A. Marinelli. **Development of ultrafast capabilities for X-ray free-electron lasers at the linac coherent light source**. *Philosophical Transactions of the Royal Society A* 377:2145 (2019), 20180386 (see pages 4, 61).
- [Cra+18] P. Craievich, S. Reiche, R. Ganter, R. D’Arcy, E. Prat, A. Grudiev, W. Wuensch, R. Zennaro, F. Christie, G. McMonagle, et al. **Sub-Femtosecond Time-Resolved Measurements Based on a Variable Polarization X-Band Transverse Deflecting Structures for SwissFEL**. *38th International Free Electron Laser Conference FEL2017* (2018) (see page 83).
- [Cra+20] P. Craievich, M. Bopp, H.-H. Braun, A. Citterio, R. Fortunati, R. Ganter, T. Kleeb, F. Marcellini, M. Pedrozzi, E. Prat, S. Reiche, K. Rolli, R. Sieber, A. Grudiev, W. L. Millar, N. Catalan-Lasheras, G. McMonagle, S. Pitman, V. d. P. Romano, K. T. Szypula, W. Wuensch, B. Marchetti, R. Assmann, F. Christie, B. Conrad, R. D’Arcy, M. Foese, P. G. Caminal, M. Hoffmann, M. Huening, R. Jonas, O. Krebs, S. Lederer, D. Marx, J. Osterhoff, M. Reukauff, H. Schlarb, S. Schreiber, G. Tews, M. Vogt, A. d. Z. Wagner, and S. Wesch. **Novel X-band transverse deflection structure with variable polarization**. *Phys. Rev. Accel. Beams* 23 (11 Nov. 2020), 112001. DOI: [10.1103/PhysRevAccelBeams.23.112001](https://doi.org/10.1103/PhysRevAccelBeams.23.112001). URL: <https://link.aps.org/doi/10.1103/PhysRevAccelBeams.23.112001> (see pages 46, 58).
- [CST19] CST. *CST Studio Suite*, (2019). 2019 (see pages 46, 49, 63, 72).
- [Div+15] M. C. Divall, E. Prat, S. Bettoni, C. Vicario, A. Trisorio, T. Schietinger, and C. P. Hauri. **Intrinsic emittance reduction of copper cathodes by laser wavelength tuning in an rf photoinjector**. *Physical Review Special Topics-Accelerators and Beams* 18:3 (2015), 033401 (see page 71).

- [Ege20] T. Egenolf. **Intensity Effects in Dielectric Laser Accelerator Structures**. PhD thesis. Darmstadt: Technische Universität, Oct. 2020. URL: <http://tuprints.ulb.tu-darmstadt.de/14139/> (see pages 38, 52, 55).
- [Emm+10] P. Emma, R. Akre, J. Arthur, R. Bionta, C. Bostedt, J. Bozek, A. Brachmann, P. Bucksbaum, R. Coffee, F.-J. Decker, et al. **First lasing and operation of an ångstrom-wavelength free-electron laser**. *nature photonics* 4:9 (2010), 641 (see pages 60, 79).
- [ENB20] T. Egenolf, U. Niedermayer, and O. Boine-Frankenheim. **Tracking with wake-fields in dielectric laser acceleration grating structures**. *Phys. Rev. Accel. Beams* 23 (5 May 2020), 054402. doi: 10.1103/PhysRevAccelBeams.23.054402. URL: <https://link.aps.org/doi/10.1103/PhysRevAccelBeams.23.054402> (see page 50).
- [Eng+14] R. J. England, R. J. Noble, K. Bane, D. H. Dowell, C.-K. Ng, J. E. Spencer, S. Tantawi, Z. Wu, R. L. Byer, E. Peralta, et al. **Dielectric laser accelerators**. *Reviews of Modern Physics* 86:4 (2014), 1337 (see pages 17, 38, 61, 79).
- [ESL09] E. Esarey, C. Schroeder, and W. Leemans. **Physics of laser-driven plasma-based electron accelerators**. *Reviews of Modern Physics* 81:3 (2009), 1229 (see pages 16, 38).
- [FEM] FEMTOprint. *FEMTOprint SA, Via Industria 3, 6933 Muzzano, Switzerland*, <https://www.femtoprint.ch/> (see pages 6, 40, 41, 58).
- [Fer+18] E. Ferrari et al. **The ACHIP experimental chambers at the Paul Scherrer Institut**. *Nuclear Instruments and Methods in Physics Research Section A: Accelerators, Spectrometers, Detectors and Associated Equipment* 907 (2018), 244–247 (see pages 3, 8, 18, 19, 38, 40, 61, 65, 79).
- [Flo00] K. Floettmann. *ASTRA* <http://www.desy.de/~mpyflo/>. 2000 (see pages 63, 71, 80).
- [FMP14] M. Ferrario, M. Migliorati, and L. Palumbo. **Space Charge Effects**. In: *Proceedings of the CAS-CERN Accelerator School: Advanced Accelerator Physics, Trondheim, Norway, 19–29 August 2013*. Vol. CERN-2014-009. 2014 (see page 71).
- [Fre+13] F. Frei, I. Gorgisyan, B. Smit, G. Orlandi, B. Beutner, E. Prat, R. Ischebeck, V. Schlott, and P. Peier. **Development of electron bunch compression monitors for SwissFEL**. In: *Proceedings of the 2nd International Beam Instrumentation Conference (IBIC 2013), Oxford, UK*. 2013, 16–19 (see page 82).
- [GBH70] R. Gordon, R. Bender, and G. T. Herman. **Algebraic reconstruction techniques (ART) for three-dimensional electron microscopy and X-ray photography**. *Journal of Theoretical Biology* 29:3 (1970), 471–481 (see page 22).

- [Ger+11] C. Gerth, B. Schmidt, S. Wesch, R. Ischebeck, G. Orlandi, P. Peier, and V. Schlott. **THz radiation diagnostics for monitoring the bunch compression at the SwissFEL Injector Test Facility**. *Proc. of DIPAC2011, Hamburg* (2011), 374–376 (see page 81).
- [Gri+08] O. Grimm, H. Delsim-hashemi, V. Bal, N. Golubeva, et al. **Transverse electron beam size effect on the bunch profile determination with coherent radiation diagnostics**. *Proceedings of EPAC08, Genoa, Italy, TUPC030* (2008) (see page 82).
- [Hal80] K. Halbach. **Design of permanent multipole magnets with oriented rare earth cobalt material**. *Nuclear Instruments and Methods* 169:1 (1980), 1–10. ISSN: 0029-554X. DOI: [https://doi.org/10.1016/0029-554X\(80\)90094-4](https://doi.org/10.1016/0029-554X(80)90094-4). URL: <https://www.sciencedirect.com/science/article/pii/0029554X80900944> (see page 9).
- [Hei+18] S. Heidrich, K. Aulenbacher, S. Donders, and A. Nikipelov. **Irradiation caused performance losses of undulators equipped with Sm₂Co₁₇ magnets**. *Journal of Magnetism and Magnetic Materials* 456 (2018), 204–211. ISSN: 0304-8853. DOI: <https://doi.org/10.1016/j.jmmm.2018.01.068>. URL: <https://www.sciencedirect.com/science/article/pii/S0304885317328299> (see page 9).
- [Her+19] B. Hermann, S. Bettoni, T. Egenolf, U. Niedermayer, E. Prat, and R. Ischebeck. **Laser-Driven Modulation of Electron Beams in a Dielectric Micro-Structure for X-Ray Free-Electron Lasers**. *Scientific Reports* 9:1 (2019), 1–9 (see pages 18, 40, 79, 80).
- [Her+21] B. Hermann, V. A. Guzenko, O. R. Hürzeler, A. Kirchner, G. L. Orlandi, E. Prat, and R. Ischebeck. **Electron beam transverse phase space tomography using nanofabricated wire scanners with submicrometer resolution**. *Phys. Rev. Accel. Beams* 24 (2 Feb. 2021), 022802. DOI: [10.1103/PhysRevAccelBeams.24.022802](https://doi.org/10.1103/PhysRevAccelBeams.24.022802). URL: <https://link.aps.org/doi/10.1103/PhysRevAccelBeams.24.022802> (see pages 39, 40).
- [HER21] HERO. *ERC Synergy project HERO: Hidden Entangled and Resonating Orders*. <http://synergyhero.org/>. 2021 (see page 4).
- [Her21] B. Hermann. *BeamTomography*. <https://github.com/hermannbene/BeamTomography>. 2021 (see page 25).
- [HK07] Z. Huang and K.-J. Kim. **Review of x-ray free-electron laser theory**. *Physical Review Special Topics-Accelerators and Beams* 10:3 (2007), 034801 (see page 64).

- [Hua+04] Z. Huang, M. Borland, P. Emma, J. Wu, C. Limborg, G. Stupakov, and J. Welch. **Suppression of microbunching instability in the linac coherent light source**. *Phys. Rev. ST Accel. Beams* 7 (7 July 2004), 074401. DOI: [10.1103/PhysRevSTAB.7.074401](https://doi.org/10.1103/PhysRevSTAB.7.074401). URL: <https://link.aps.org/doi/10.1103/PhysRevSTAB.7.074401> (see page 48).
- [Isc+15] R. Ischebeck, E. Prat, V. Thominet, and C. Ozkan Loch. **Transverse profile imager for ultrabright electron beams**. *Physical Review Special Topics-Accelerators and Beams* 18:8 (2015), 082802 (see pages 10, 12, 17, 31).
- [Isc+20] R. Ischebeck et al. **Characterization of the electron beam in the ACHIP chamber in SwissFEL**. *J. Phys. Conf. Ser.* 1596:1 (2020), 012019. DOI: [10.1088/1742-6596/1596/1/012019](https://doi.org/10.1088/1742-6596/1596/1/012019) (see pages 3, 19, 20).
- [Ish+12] T. Ishikawa, H. Aoyagi, T. Asaka, Y. Asano, N. Azumi, T. Bizen, H. Ego, K. Fukami, T. Fukui, Y. Furukawa, et al. **A compact X-ray free-electron laser emitting in the sub-ångström region**. *nature photonics* 6:8 (2012), 540 (see pages 60, 79).
- [Ji+19] F. Ji, D. B. Durham, A. M. Minor, P. Musumeci, J. G. Navarro, and D. Filippetto. **Ultrafast relativistic electron nanoprobe**. *Communications Physics* 2:54 (2019), 1–10. DOI: <https://doi.org/10.1038/s42005-019-0154-4>. URL: <https://doi.org/10.1038/s42005-019-0154-4> (see page 17).
- [Kan+17] H.-S. Kang, C.-K. Min, H. Heo, C. Kim, H. Yang, G. Kim, I. Nam, S. Y. Baek, H.-J. Choi, G. Mun, et al. **Hard X-ray free-electron laser with femtosecond-scale timing jitter**. *Nature Photonics* 11:11 (2017), 708 (see pages 60, 79).
- [Koz+18] M. Kozák, J. McNeur, N. Schönenberger, J. Illmer, A. Li, A. Tafel, P. Yousefi, T. Eckstein, and P. Hommelhoff. **Ultrafast scanning electron microscope applied for studying the interaction between free electrons and optical near-fields of periodic nanostructures**. *Journal of Applied Physics* 124:2 (2018), 023104 (see page 61).
- [KPJ07a] R. Kitamura, L. Pilon, and M. Jonasz. **Optical constants of silica glass from extreme ultraviolet to far infrared at near room temperature**. *Appl. Opt.* 46:33 (Nov. 2007), 8118–8133. DOI: [10.1364/AO.46.008118](https://doi.org/10.1364/AO.46.008118). URL: <http://ao.osa.org/abstract.cfm?URI=ao-46-33-8118> (see pages 55, 56, 58).
- [KPJ07b] R. Kitamura, L. Pilon, and M. Jonasz. **Optical constants of silica glass from extreme ultraviolet to far infrared at near room temperature**. *Applied optics* 46:33 (2007), 8118–8133 (see page 68).

- [Lee+18] K. J. Leedle, D. S. Black, Y. Miao, K. E. Urbanek, A. Ceballos, H. Deng, J. S. Harris, O. Solgaard, and R. L. Byer. **Phase-dependent laser acceleration of electrons with symmetrically driven silicon dual pillar gratings**. *Opt. Lett.* 43:9 (May 2018), 2181–2184. DOI: [10.1364/OL.43.002181](https://doi.org/10.1364/OL.43.002181). URL: <http://ol.osa.org/abstract.cfm?URI=ol-43-9-2181> (see page 2).
- [LHS94] R. Lai, U. Happek, and A. Sievers. **Measurement of the longitudinal asymmetry of a charged particle bunch from the coherent synchrotron or transition radiation spectrum**. *Physical Review E* 50:6 (1994), R4294 (see page 82).
- [LS94] R. Lai and A. Sievers. **Determination of a charged-particle-bunch shape from the coherent far infrared spectrum**. *Physical Review E* 50:5 (1994), R3342 (see page 82).
- [Mac+19] J. P. MacArthur, J. Duris, Z. Zhang, A. Lutman, A. Zholents, X. Xu, Z. Huang, and A. Marinelli. **Phase-stable self-modulation of an electron beam in a magnetic wiggler**. *Physical review letters* 123:21 (2019), 214801 (see page 6).
- [Mar+06] X.-M. Maréchal, T. Bizen, Y. Asano, and H. Kitamura. **65 MeV Neutron Irradiation of Nd-Fe-B Permanent Magnets**. In: *Proc. of European Particle Accelerator Conference (EPAC 2006)*. 2006, 3116–3118 (see page 9).
- [Mar+20] B. Marchetti, R. Assmann, R. Brinkmann, F. Burkart, U. Dorda, K. Floettmann, I. Hartl, W. Hillert, M. Huening, F. Jafarinaia, S. Jaster-Merz, M. Kellermeier, W. Kuroopka, F. Lemery, D. Marx, F. Mayet, E. Panofski, S. Pfeiffer, H. Schlarb, T. Vinatier, P. A. Walker, L. Winkelmann, and S. Yamin. **SINBAD-ARES - A Photo-Injector for external Injection Experiments in novel Accelerators at DESY**. *Journal of Physics: Conference Series* 1596 (July 2020), 012036. DOI: [10.1088/1742-6596/1596/1/012036](https://doi.org/10.1088/1742-6596/1596/1/012036). URL: <https://doi.org/10.1088/1742-6596/1596/1/012036> (see page 12).
- [Max+17] J. Maxson, D. Cesar, G. Calmasini, A. Ody, P. Musumeci, and D. Alesini. **Direct measurement of sub-10 fs relativistic electron beams with ultralow emittance**. *Physical Review Letters* 118:15 (2017), 154802 (see pages 17, 31, 32).
- [May+18] F. Mayet, R. Assmann, J. Bödewadt, R. Brinkmann, U. Dorda, W. Kuroopka, C. Lechner, B. Marchetti, and J. Zhu. **Simulations and plans for possible DLA experiments at SINBAD**. *Nuclear Instruments and Methods in Physics Research Section A: Accelerators, Spectrometers, Detectors and Associated Equipment* 909 (2018). 3rd European Advanced Accelerator Concepts workshop (EAAC2017), 213–216. ISSN: 0168-9002. DOI: <https://doi.org/10.1016/j.nima.2018.01.088>. URL: <https://www.sciencedirect.com/science/article/pii/S0168900218301219> (see page 12).
- [Mil+17] C. Milne, T. Schietinger, M. Aiba, A. Alarcon, J. Alex, A. Anghel, V. Arsov, C. Beard, P. Beaud, S. Bettoni, et al. **SwissFEL: the Swiss X-ray free electron laser**. *Applied Sciences* 7:7 (2017), 720 (see pages 3, 38, 60, 79).

- [Mod+95] A. Modena, Z. Najmudin, A. Dangor, C. Clayton, K. Marsh, C. Joshi, V. Malka, C. Darrow, C. Danson, D. Neely, et al. **Electron acceleration from the breaking of relativistic plasma waves**. *Nature* 377:6550 (1995), 606–608 (see page 1).
- [Mos+12] A. Mostacci, M. Bellaveglia, E. Chiadroni, A. Cianchi, M. Ferrario, D. Filippetto, G. Gatti, and C. Ronsivalle. **Chromatic effects in quadrupole scan emittance measurements**. *Phys. Rev. ST Accel. Beams* 15 (8 Aug. 2012), 082802. DOI: 10.1103/PhysRevSTAB.15.082802. URL: <https://link.aps.org/doi/10.1103/PhysRevSTAB.15.082802> (see page 18).
- [NBE17] U. Niedermayer, O. Boine-Frankenheim, and T. Egenolf. **Designing a dielectric laser accelerator on a chip**. In: *Journal of Physics: Conference Series*. Vol. 874. 1. IOP Publishing. 2017, 012041 (see page 63).
- [NEB17] U. Niedermayer, T. Egenolf, and O. Boine-Frankenheim. **Beam dynamics analysis of dielectric laser acceleration using a fast 6d tracking scheme**. *Physical Review Accelerators and Beams* 20:11 (2017), 111302 (see pages 62, 63, 66, 72, 73).
- [Nie+19] U. Niedermayer, A. Adelmann, R. Aßmann, S. Bettoni, D. Black, O. Boine-Frankenheim, P. Broaddus, R. Byer, M. Calvi, H. Cankaya, et al. **Challenges in Simulating Beam Dynamics of Dielectric Laser Acceleration**. In: *13th Int. Computational Accelerator Physics Conf.(ICAP'18), Key West, FL, USA, 20-24 October 2018*. JACOW Publishing, Geneva, Switzerland. 2019, 120–126 (see page 62).
- [Orl+16] G. L. Orlandi, P. Heimgartner, R. Ischebeck, C. Ozkan Loch, S. Trovati, P. Valitutti, V. Schlott, M. Ferianis, and G. Penco. **Design and experimental tests of free electron laser wire scanners**. *Physical Review Accelerators and Beams* 19:9 (2016), 092802 (see page 17).
- [Orl+20] G. L. Orlandi, C. David, E. Ferrari, V. Guzenko, R. Ischebeck, E. Prat, B. Hermann, M. Ferianis, G. Penco, M. Veronese, et al. **Nanofabricated free-standing wire scanners for beam diagnostics with submicrometer resolution**. *Physical Review Accelerators and Beams* 23:4 (2020), 042802 (see pages 12, 17, 21, 32).
- [Ozk+20] C. Ozkan Loch, D. Llorente Sancho, E. Divall, E. Ebner, P. Pollet, R. Ischebeck, and F. Loehl. **Loss monitoring for undulator protection at SwissFEL**. *Phys. Rev. Accel. Beams* 23 (10 Oct. 2020), 102804. DOI: 10.1103/PhysRevAccelBeams.23.102804. URL: <https://link.aps.org/doi/10.1103/PhysRevAccelBeams.23.102804> (see page 22).
- [PA14] E. Prat and M. Aiba. **Four-dimensional transverse beam matrix measurement using the multiple-quadrupole scan technique**. *Phys. Rev. ST Accel. Beams* 17 (5 May 2014), 052801. DOI: 10.1103/PhysRevSTAB.17.052801. URL: <https://link.aps.org/doi/10.1103/PhysRevSTAB.17.052801> (see page 25).

- [PB68] W. K. H. Panofsky and M. Bander. **Asymptotic Theory of Beam Break-Up in Linear Accelerators**. *Review of Scientific Instruments* 39:2 (1968), 206–212. DOI: [10.1063/1.1683315](https://doi.org/10.1063/1.1683315). eprint: <https://doi.org/10.1063/1.1683315>. URL: <https://doi.org/10.1063/1.1683315> (see page 38).
- [Per+13] E. Peralta, K. Soong, R. England, E. Colby, Z. Wu, B. Montazeri, C. McGuinness, J. McNeur, K. Leedle, D. Walz, et al. **Demonstration of electron acceleration in a laser-driven dielectric microstructure**. *Nature* 503:7474 (2013), 91–94 (see pages 2, 41).
- [PLR15] E. Prat, F. Löhl, and S. Reiche. **Efficient generation of short and high-power x-ray free-electron-laser pulses based on superradiance with a transversely tilted beam**. *Phys. Rev. ST Accel. Beams* 18 (10 Oct. 2015), 100701. DOI: [10.1103/PhysRevSTAB.18.100701](https://doi.org/10.1103/PhysRevSTAB.18.100701). URL: <https://link.aps.org/doi/10.1103/PhysRevSTAB.18.100701> (see pages 44, 56).
- [Pra+14] E. Prat, M. Aiba, S. Bettoni, B. Beutner, S. Reiche, and T. Schietinger. **Emittance measurements and minimization at the SwissFEL Injector Test Facility**. *Physical Review Special Topics-Accelerators and Beams* 17:10 (2014), 104401 (see page 62).
- [Pra+15] E. Prat, S. Bettoni, H.-H. Braun, R. Ganter, and T. Schietinger. **Measurements of copper and cesium telluride cathodes in a radio-frequency photoinjector**. *Physical Review Special Topics-Accelerators and Beams* 18:4 (2015), 043401 (see page 71).
- [Pra+16] E. Prat, M. Calvi, R. Ganter, S. Reiche, T. Schietinger, and T. Schmidt. **Undulator beamline optimization with integrated chicanes for X-ray free-electron-laser facilities**. *Journal of synchrotron radiation* 23:4 (2016), 861–868 (see page 61).
- [Pra+17] E. Prat, S. Bettoni, M. Calvi, M. Dehler, F. Frei, P. Hommelhoff, M. Kozak, J. McNeur, C. O. Loch, S. Reiche, et al. **Outline of a dielectric laser acceleration experiment at SwissFEL**. *Nuclear Instruments and Methods in Physics Research Section A: Accelerators, Spectrometers, Detectors and Associated Equipment* 865 (2017), 87–90 (see pages 3, 8, 18, 19, 38, 40, 61, 65, 79).
- [Pra+20] E. Prat, P. Dijkstal, E. Ferrari, A. Malyzhenkov, and S. Reiche. **High-resolution dispersion-based measurement of the electron beam energy spread**. *Phys. Rev. Accel. Beams* 23 (9 Sept. 2020), 090701. DOI: [10.1103/PhysRevAccelBeams.23.090701](https://doi.org/10.1103/PhysRevAccelBeams.23.090701). URL: <https://link.aps.org/doi/10.1103/PhysRevAccelBeams.23.090701> (see page 48).
- [Pra14] E. Prat. **Symmetric single-quadrupole-magnet scan method to measure the 2D transverse beam parameters**. *Nuclear Instruments and Methods in Physics Research Section A: Accelerators, Spectrometers, Detectors and Associated Equipment* 743 (2014), 103–108 (see pages 19, 31, 39).

- [Rai+93] P. Raimondi, P. Emma, N. Toge, N. Walker, and V. Ziemann. **Sigma matrix reconstruction in the SLC final focus**. *Conf. Proc. C 930517* (1993). Ed. by S. T. Corneliussen and L. Carlton, 98–99 (see page 25).
- [RO94] M. Reiser and P. O’Shea. **Theory and design of charged particle beams**. Vol. 312. Wiley Online Library, 1994 (see page 1).
- [Ros+20] J. B. Rosenzweig et al. **An ultra-compact X-ray free-electron laser**. *New J. Phys.* 22 (2020), 093067 (see pages 17, 32).
- [RWT01] S. Ratschow, T. Weiland, and M. Timm. **On the mechanism of surface roughness wake field excitation**. *PACS2001. Proceedings of the 2001 Particle Accelerator Conference (Cat. No.01CH37268)* 1 (2001), 167–169 vol.1. DOI: [10.1109/PAC.2001.987460](https://doi.org/10.1109/PAC.2001.987460) (see page 58).
- [Sap+20] N. V. Sapro, K. Y. Yang, D. Vercruysse, K. J. Leedle, D. S. Black, R. J. England, L. Su, R. Trivedi, Y. Miao, O. Solgaard, R. L. Byer, and J. Vučković. **On-chip integrated laser-driven particle accelerator**. *Science* 367:6473 (2020), 79–83. ISSN: 0036-8075. DOI: [10.1126/science.aay5734](https://doi.org/10.1126/science.aay5734). eprint: <https://science.sciencemag.org/content/367/6473/79.full.pdf>. URL: <https://science.sciencemag.org/content/367/6473/79> (see page 2).
- [Sch+19] N. Schönenberger, A. Mittelbach, P. Yousefi, J. McNeur, U. Niedermayer, and P. Hommelhoff. **Generation and Characterization of Attosecond Microbunched Electron Pulse Trains via Dielectric Laser Acceleration**. *Phys. Rev. Lett.* 123 (26 Dec. 2019), 264803. DOI: [10.1103/PhysRevLett.123.264803](https://doi.org/10.1103/PhysRevLett.123.264803). URL: <https://link.aps.org/doi/10.1103/PhysRevLett.123.264803> (see page 1).
- [SP53] S. J. Smith and E. M. Purcell. **Visible Light from Localized Surface Charges Moving across a Grating**. *Phys. Rev.* 92 (4 Nov. 1953), 1069–1069. DOI: [10.1103/PhysRev.92.1069](https://doi.org/10.1103/PhysRev.92.1069). URL: <https://link.aps.org/doi/10.1103/PhysRev.92.1069> (see page 12).
- [SSY97] E. Saldin, E. Schneidmiller, and M. Yurkov. **On the coherent radiation of an electron bunch moving in an arc of a circle**. *Nuclear Instruments and Methods in Physics Research Section A: Accelerators, Spectrometers, Detectors and Associated Equipment* 398:2 (1997), 373–394. ISSN: 0168-9002. DOI: [https://doi.org/10.1016/S0168-9002\(97\)00822-X](https://doi.org/10.1016/S0168-9002(97)00822-X). URL: <https://www.sciencedirect.com/science/article/pii/S016890029700822X> (see page 48).
- [Stu98] G. V. Stupakov. **Impedance of small obstacles and rough surfaces**. *Phys. Rev. ST Accel. Beams* 1 (6 Oct. 1998), 064401. DOI: [10.1103/PhysRevSTAB.1.064401](https://doi.org/10.1103/PhysRevSTAB.1.064401). URL: <https://link.aps.org/doi/10.1103/PhysRevSTAB.1.064401> (see page 58).
- [TM08] N. Thompson and B. McNeil. **Mode locking in a free-electron laser amplifier**. *Physical review letters* 100:20 (2008), 203901 (see pages 38, 61, 79).

- [TS99] P. Tenenbaum and T. Shintake. **Measurement of small electron-beam spots**. *Annual Review of Nuclear and Particle Science* 49:1 (1999), 125–162 (see page 32).
- [Wei+17] Y. Wei, M. Ibison, G. Xia, J. Smith, and C. Welsch. **Dual-grating dielectric accelerators driven by a pulse-front-tilted laser**. *Applied optics* 56:29 (2017), 8201–8206 (see page 61).
- [Wil89] P. B. Wilson. **Introduction to wakefields and wake potentials**. *AIP Conference Proceedings* 184:1 (1989), 525–564 (see pages 52, 53).
- [Woo+16] K. P. Wootton, Z. Wu, B. M. Cowan, A. Hanuka, I. V. Makasyuk, E. A. Peralta, K. Soong, R. L. Byer, and R. J. England. **Demonstration of acceleration of relativistic electrons at a dielectric microstructure using femtosecond laser pulses**. *Optics letters* 41:12 (2016), 2696–2699 (see page 67).
- [You+19] P. Yousefi, N. Schönenberger, J. Mcneur, M. Kozák, U. Niedermayer, and P. Hommelhoff. **Dielectric laser electron acceleration in a dual pillar grating with a distributed Bragg reflector**. *Optics letters* 44:6 (2019), 1520–1523 (see pages 2, 63).
- [Zho+04] A. A. Zholents, P. Emma, S. Reiche, G. Stupakov, Z. Huang, and W. Fawley. **Current-enhanced SASE using an optical laser and its application to the LCLS**. In: *Presented at. SLAC-PUB-10713*. 2004, 582–585 (see pages 67, 69).
- [Zho05] A. A. Zholents. **Method of an enhanced self-amplified spontaneous emission for x-ray free electron lasers**. *Physical Review Special Topics-Accelerators and Beams* 8:4 (2005), 040701 (see pages 4, 61, 64, 68, 79).

List of Publications

Articles in Refereed Journals as First Author

- [1] **Laser-Driven Modulation of Electron Beams in a Dielectric Micro-Structure for X-Ray Free-Electron Lasers.** *Scientific Reports* 9:1 (2019), 1–9. Joint work with S. Bettoni, T. Egenolf, U. Niedermayer, E. Prat, and R. Ischebeck.
- [2] **Electron beam transverse phase space tomography using nanofabricated wire scanners with submicrometer resolution.** *Phys. Rev. Accel. Beams* 24 (2 Feb. 2021), 022802. Joint work with V. A. Guzenko, O. R. Hürzeler, A. Kirchner, G. L. Orlandi, E. Prat, and R. Ischebeck.

Articles in Refereed Conference Proceedings as First Author

- [3] **Diagnostics for Electron Pulse Trains at SwissFEL Obtained by Energy Modulation in a Laser-Driven Dielectric Structure.** In: *Journal of Physics: Conference Series*. Vol. 1596. 1. IOP Publishing. 2020, 012046. Joint work with S. Bettoni, T. Egenolf, T. Feurer, F. Frei, U. Niedermayer, E. Prat, and R. Ischebeck.

Articles in Refereed Journals as Co-Author

- [4] **Challenges in simulating beam dynamics of dielectric laser acceleration.** *International Journal of Modern Physics A* 34:36 (2019), 1942031. Joint work with U. Niedermayer, A. Adelman, S. Bettoni, M. Calvi, M. Dehler, E. Ferrari, F. Frei, D. Hauenstein, N. Hiller, et al..
- [5] **Nanofabricated free-standing wire scanners for beam diagnostics with submicrometer resolution.** *Physical Review Accelerators and Beams* 23:4 (2020), 042802. Joint work with G. Orlandi, C. David, E. Ferrari, V. Guzenko, R. Ischebeck, E. Prat, M. Ferianis, G. Penco, M. Veronese, et al..

Articles in Conference Proceedings as Co-Author

- [6] **Characterization of the Electron Beam in the ACHIP Chamber in Swiss-FEL.** In: *Journal of Physics: Conference Series*. Vol. 1596. 1. IOP Publishing. 2020, 012019. Joint work with R. Ischebeck, S. Bettoni, S. Borrelli, M. Calvi, P. Dijkstal, E. Ferrari, V. Guzenko, D. Hauenstein, O. Hürzeler, et al..
- [7] **Towards additive manufacturing of dielectric accelerating structures.** In: *Journal of Physics: Conference Series*. Vol. 1596. 1. IOP Publishing. 2020, 012020. Joint work with M. Kellermeier, S. Zinsli, U. Dorda, R. Ischebeck, J. Lehmann, K. Flöttmann, F. Lemery, H. Dinter, C. Lombosi, et al..
- [8] **Wire-Scanners with Sub-Micrometer Resolution: Developments and Measurements.** In: *39th Free Electron Laser Conference (FEL'19), Hamburg, Germany, 26-30 August 2019*. JACOW Publishing, Geneva, Switzerland. 2019, 307–310. Joint work with G. L. Orlandi, S. Borrelli, C. David, E. Ferrari, V. Guzenko, O. Huerzeler, R. Ischebeck, C. Lombosi, C. Ozkan-Loch, et al..
- [9] **Dielectric Waveguide Based THz Radiator Study for SwissFEL.** In: *29th Linear Accelerator Conference, Beijing, China, 2018*. 2019. Joint work with L. Shi, F. Marcellini, S. Reiche, R. Ischebeck, A. Mittelbach, S. Bettoni, V. Thominet, E. Ferrari, and M. Dehler.

BENEDIKT HERMANN

Mühlackerstrasse 108, 8046 Zurich | benedikt.hermann@psi.ch

PERSONAL DATA

Date, Place of Birth 04/12/1993, Starnberg, Germany
Nationality German

EDUCATION

Since 10/2017 *Paul Scherrer Institut and University of Bern, Switzerland*
PhD in Physics

09/2015 – 04/2017 *Swiss Federal Institute of Technology, Zurich, Switzerland*
Master of Science ETH in Physics

09/2012 – 09/2015 *Swiss Federal Institute of Technology, Zurich, Switzerland*
Bachelor of Science ETH in Physics

09/2004 – 06/2012 *Kurt-Huber-Gymnasium, Gräfelfing, Germany*
High School Diploma

WORK HISTORY AND INTERNSHIPS

Since 10/2017 *Paul Scherrer Institut, Switzerland*
PhD Researcher

04/2017 – 09/2017 *Optotune, Dietikon, Switzerland*
Internship (100 %)

02/2015 – 12/2016 *Swiss Federal Institute of Technology, Zurich, Switzerland*
Teaching Assistant (30 %)

06/2015 – 07/2015 *CERN, Geneva, Switzerland*
Summer Internship (100 %)

09/2010 – 05/2012 *German Aerospace Centre (DLR), Oberpfaffenhofen, Germany*
Internship (10 %)